Investigating the near-surface airflow
and its turbulent and submesoscale statistics
for the weak-wind regime from field experiments

Master thesis in Physics

University of Bayreuth

Anita Freundorfer

1. Supervisor: Prof. Dr. Ingo Rehberg

2. Supervisor: Prof. Dr. Christoph Thomas

October 23, 2017

1 Abstract

The behaviour of the atmospheric boundary layer (ABL) during weak-wind situations is still not completely understood, mainly due to the existence of so-called submeso motions. Thus, further research on the typical phenomena during weak-wind situations and their physical mechanisms is required. For this purpose, during the **A**dvanced **R**esolution **C**anopy **FL**ow **O**bservations experiment (ARCFLO), data were collected at four different sites located in Oregon, USA. Those sites cover a variety of terrain complexities and vegetation densities, especially focusing on different forest architectures. The following work focusses on evaluating the data obtained in the series of ARCFLO experiments and comparing the different sites.

After an introduction to the typical approaches for investigating turbulence in the ABL and a description of the study sites and our data, a way of determining an objective threshold velocity for the weak-wind regime is elaborated. This is done using a scatter plot of the friction velocity u_* in dependence of the mean wind velocity $\overline{u}_{\mathrm{skal}}$. Using a segmented linear regression with two segments, a transition point can be found, where the mean behaviour of the friction velocity changes from nearly independent from the mean wind velocity to a linear dependency. This threshold can be identified for all four sites. The identified thresholds vary from $u_{\mathrm{thr}} = 0.25 \, \frac{\mathrm{m}}{\mathrm{s}}$ at the grassland site to $u_{\mathrm{thr}} = 1.03 \, \frac{\mathrm{m}}{\mathrm{s}}$ most densely forested site.

Subsequently, it is investigated how the weak-wind threshold is influenced by the landscape and vegetation. We find that a denser vegetation leads to a higher threshold velocity. Thus, we test the hypothesis that in the weak-wind regime, the subcanopy is inherently decoupled from the above canopy. However, this hypothesis can not be confirmed.

In the next section, meandering is analysed. Meandering is one of the typical phenomena during weak-wind situations. We develop a novel method for identifying meandering periods using the difference between vector averages and scalar averages. The results from this new method are compared to those from a commonly applied method from literature. This other method makes use of the special form of the autocorrelation function of the horizontal wind components in meandering situations. For the detected meandering periods we analyse the typical inherent time scales by means of the autocorrelation function as well as by using wavelet analysis. We find a broad range of meandering time scales at all 4 sites with a preference of shorter time scales. The average time scale during the night is slightly longer than that during the day.

II Zusammenfassung

Das Verhalten der atmosphärischen Grenzschicht während Schwachwindsituationen ist bisher noch nicht vollständig verstanden. Der Grund dafür sind sogenannte, vor allem bei Schwachwind auftretende, submesoskalige Strukturen. Daher ist es nötig, die typischen Phänomene während Schwachwindsituationen und deren physikalische Mechanismen weiter zu untersuchen. Dazu wurden im Rahmen des 'Advanced Resolution Canopy FLow Observations' Experiments (ARCFLO) an vier verschiedenen Standorten in Oregon, USA, Messungen durchgeführt. Diese Standorte umfassen eine große Bandbreite an Komplexität bzgl. des Geländes und an Vegetationsdichten. Die folgende Arbeit konzentriert sich darauf, die Daten der ARCFLO Experimente auszuwerten und die verschiedenen Standorte zu vergleichen.

Nach einer Einführung in die typischen Ansätze zur Analyse von Turbulenz in der atmosphärischen Grenzschicht und einer Beschreibung der Standorte und der Messdaten wird eine Methode entwickelt, um einen objektiven Grenzwert der Windgeschwindigkeit für das Schwachwindregime zu bestimmen. Dazu wird ein Streudiagramm der Schubspannungsgeschwindigkeit u_* in Abhängigkeit von der skalar gemittelten Windgeschwindigkeit $\bar{u}_{\mathrm{scal}}$ erzeugt. Anschließend wird eine abschnittsweise definierte lineare Funktion mit zwei Abschnitten an die Daten im Streudiagramm angepasst. Es kann ein Übergangspunkt gefunden werden, wo das mittlere Verhalten der Schubspannungsgeschwindigkeit von nahezu unabhängig von der mittleren Windgeschwindigkeit in eine lineare Abhängigkeit übergeht. Dieser Grenzwert kann an allen vier Standorten identifiziert werden. Die gefundenen Grenzwerte variieren zwischen $u_{\mathrm{thr}} = 0,25\,\frac{\mathrm{m}}{\mathrm{s}}$ am unbewaldeten Standort und $u_{\mathrm{thr}} = 1,03\,\frac{\mathrm{m}}{\mathrm{s}}$ im dichtesten der untersuchten Wälder. Anschließend wird untersucht, wie der Schwachwindgrenzwert von der Landschaft und der Vegetation beeinflusst wird. Es stellt sich heraus, dass eine dichtere Vegetation zu einer höreren Grenzgeschwindigkeit führt. Es wird die Hypothese getestet, dass während Schwachwindsituationen der Stammraum von der Luftschicht oberhalb der Baumkronen entkoppelt ist. Diese Hypothese kann jedoch nicht bestätigt werden.

Im nächsten Abschnitt wird das Phänomen des Mäandrierens analysiert. Mäandrieren is eines der Phänomene, die typischerweise während Schwachwindsituationen auftreten. Wir entwickeln eine Methode, um Intervalle zu indentifizieren, während denen mäandieren auftritt. Dazu von dem Unterschied zwischen einem vektoriellen und einem skalaren Mittelwert wird Gebrauch gemacht. Die Ergebnisse dieser neuen Methode zum Detektieren von Mäandireren werden mit einer Methode verglichen, welche in der Literatur häufig angewendet wird. Diese zweite Methode nutzt die spezielle Form, die die Autokorrelationsfunktion der horizontalen Windkomponenten während Mäandriersituationen annimmt.

Für die Intervalle, für die Mäandrieren festgestellt wurde, analysieren wir die typi-

scherweise auftretenden Zeitskalen mit Hilfe der Autokorrelationsfunktion sowie mit Hilfe einer Waveletanalyse. Es zeigt sich, dass an allen vier Standorten eine große Bandbreite an Mäandrierzeitskalen auftritt, wobei kürzere Zeitskalen bevorzugt sind. Die mittlere nächtliche Mäandrierzeitskala ist etwas länger als die während des Tages.

Contents

List of Figures

List of Tables

1 Introduction

The stable atmospheric boundary layer plays an important role in weather and climate models, for this is where the exchange of energy happens (Holtslag 2006; Holtslag *et al.* 2013). Also diffusion of airborne pollutants, formation of fog and the estimation of the potential of forests to act as a carbon sink are determined by phenomena in the stable atmospheric boundary layer (Duynkerke 1999; Acevedo *et al.* 2009; Vickers *et al.* 2012; Thomas *et al.* 2013; Kristensen *et al.* 1981). Yet, the stable atmospheric boundary layer is still not very well understood. Particularly the very stable weak-wind boundary layer that often develops during the night due to radiative cooling still offers a large amount of unanswered questions (Mahrt, 2014). In stable weak-wind situations, submesoscale motions prevail like cold air drainage, solitons, gravity waves or two-dimensional motions like meandering (Mahrt, 2014). It is hypothesized that submeso motions are actually always present in the atmosphere, but only during those weak-wind cases they appear so clearly because then they are not superimposed by other, stronger flow modes. Submeso motions are phenomena with a typical size smaller and more short-lived than that of mesoscale motions but bigger and more long-lived than the typical turbulent scales (Mahrt *et al.*, 2009). They are mostly two-dimensional, often intermittent, non-local and they neither obey the common similarity laws nor Taylor's hypothesis (Thomas 2011; Belušić & Mahrt 2008). Because of the failure of Taylor's hypothesis, spatial observations collected from a network of sensors are necessary in order to properly investigate submesoscale motions (Thomas, 2011). Thus, considerable experimental challenges have to be met. So far mostly only case studies exist (Mahrt *et al.*, 2009).

The first step in studying weak-wind phenomena is of course finding a proper definition for what determines a weak-wind situation. Some authors determine all wind speeds lower than 1.5 $\frac{\text{m}}{\text{s}}$ as weak wind (Anfossi *et al.* 2005; Mortarini *et al.* 2013; Cava *et al.* 2017). Others have attributed a 'low wind speed' situation if the mean wind speed u is less than the root-mean-square of the horizontal turbulent velocity fluctuations σ_u (Deaves & Lines, 1998).

Sun *et al.* (2012) showed that the turbulence intensity only starts to depend linearly on the mean flow starting from a certain minimum wind speed. This minimum wind speed can be taken as the transition point between the strong-wind regime and the weak-wind regime (Mahrt *et al.*, 2015). The transition point was shown to be site-dependent (Mahrt & Thomas, 2016) as well as height-dependent (Sun *et al.*, 2012).

We will use this classification scheme with the friction velocity as an indicator for the turbulence strength following Mahrt & Thomas (2016). This way, a site-dependent weak-wind threshold can be identified. Next we will analyse the dependence of the

weak-wind threshold on the properties of the site. We will further look if low wind speeds are connected to a decoupling of the lower layers of the atmosphere (i.e. the subcanopy at the forested sites) (Thomas *et al.*, 2013). Decoupling means that no transport of momentum or of any other scalars like e.g. CO_2 happens between the decoupled layers and the air above. As an indicator for coupling or decoupling, we use the dependence of the standard deviation of the vertical wind component σ_w in the subcanopy from the one above the canopy. A smaller slope in this dependence should indicate a decoupled state of the subcanopy while during a coupled situation the subcanopy turbulence should be driven by the above canopy turbulence. This should result in a greater slope.

One of the typical submesoscale phenomena mainly present during low wind-speed conditions is meandering. There is no exact physical definition on what is meant by meandering, but typically it is described as a low frequency oscillation of the wind direction over a wide variety of angles, or as sudden, horizontal wind direction shifts (Mahrt 2007; Belušić & Mahrt 2008). Those drastic changes of wind direction lead to a failing of all models describing dispersion in low wind speeds, as a gaussian plume cannot be applied any longer. Thus in meandering conditions it can for example not be predicted correctly, how a pollutant will spread.

According to Anfossi *et al.* (2005), meandering starts to prevail when wind speed decreases below 1 to 2 $\frac{m}{s}$ but also exists for higher wind speeds. It may have many different causes and can be triggered by surface pressure perturbations above the boundary layer, by pulsating cold air drainage, by solitons etc. (Mahrt, 2007). Oettl *et al.* (2005) and Goulart *et al.* (2007) showed that meandering even is an inherent solution of the Navier-Stokes equation in low wind speed conditions with negligible turbulent forcing and with the flow being almost being in geostrophic balance.Thus a specific trigger for meandering is not even necessary.

For detection of meandering, the Eulerian autocorrelation function has proven to be useful (Anfossi *et al.* 2005; Mortarini *et al.* 2016*b*). This is based on the negative lobe that the horizontal velocity component's autocorrelation functions frequently show during low wind speed conditions (Oettl *et al.*, 2001). Anfossi *et al.* (2005) attributed the negative lobe to the occurence of large-scale eddies with a vertical axis and found an analytical form for this autocorrelation function. In this analytical form two time scales are present. One of them describes the time scale of the slow horizontal directional changes and the other one of them describes the decorrelation if the flow due to turbulence. The ratio of those two times scales can be used for identifying meandering situations (Mortarini *et al.*, 2013). Unfortunately, determining those two time scales for every interval includes considerable computational effort. Furthermore, with more wave modes being present simultaneously, the fit of the autocorrelation function, which is necessary for deciding whether or not an interval is meandering, fails (Cava *et al.*, 2017).

We will develop another method for identifying meandering that is more straight-forward and where a complete timeseries can be analysed at once without having been split into single intervals first. The new method makes use of the constancy, which quantifies how symmetric the wind directions are distributed over the full

range of 360° during a specific interval (Singer 1967; Mahrt 2007). Comparison of the new method to the autocorrelation method shows promising results for clearly meandering intervals. The new method performs better than the autocorrelation method for detecting intervals with a superposition of different time scales. However, with the new method, great care has to be taken to avoid misinterpreting turbulent fluctuations for meandering.

For analysing the time scales of the meandering, either the time scale the autocorrelation functions can be used or wavelet analysis can be applied (Thomas & Foken 2005; Cava *et al.* 2017). We use both methods and compare the results. Again it becomes clear that in case of a superposition of different scales, the results from the autocorrelation function are not very reliable. However, if one scale clearly dominates, both methods agree very well.

2 Data and site descriptions

We analyse data from sensor networks at four different sites with different vegetation density and terrain complexity. In this chapter we will first describe the sensors and the data they provide for the analysis and then the study sites. For the site descriptions, we start at the site with the least dense vegetation and then go on to the more and more densely vegetated ones.

2.1 Measuring devices and data

On each of the study sites, a network of 12 SUbcanopy Sonic ANemometer (SUSAN) units was deployed over a period of one to two months in late summer. Each SUSAN unit consists of one sonic anemometer (Model 81000VRE, R.M. Young, Traverse City, MI, USA) and one Vaisala HMP Thermohygrometer (models 155 and 45c) (Drake et al., 2012a). The SUSAN units will be called SUSAN A1 to A4, B1 to B4 and C1 to C4. All sensors heights will be given in height above ground.

Figure 2.1: Photo of a SUSAN unit at the Botany and Plant Pathology site. The sonic anemometer is attached to the right and the thermohygrometer to the left side of the metal crossbar.

Measured parameters
time stamp t
wind velocity u_s
wind velocity v_s
wind velocity w_s
sonic temperature T_s
temperature T
vapour pressure e

Table 2.1: List of the parameters measured by a SUSAN unit

A picture of a SUSAN unit is shown in figure 2.1. Both measurement devices are attached to a cross bar (thermohygrometer left, sonic anemometer right). The sonic anemometer reports three wind velocity components u_s, v_s and w_s and the sonic temperature T_s, while the thermohygrometer gives back the temperature T and

the vapour pressure e (see tab. 2.1). For measuring the wind velocity, the sonic anemometer sends ultrasonic pulses back and forth between its transducers and measures the transit time of the pulses. The difference in the transit times for the opposite directed pulses depends on the velocity of the air in the path between the transducers.

The wind velocity along the transducer axis u_{12} is given by

$$u_{12} = \frac{d}{2} \left(\frac{1}{t_{12}} - \frac{1}{t_{21}} \right) \tag{2.1}$$

where d is the distance between the transducers. t_{12} and t_{21} are the transit times of the ultrasonic pulse in opposite directions (Aubinet *et al.*, 2012). As there are three pairs of transducers at the sonic anemometers of the SUSAN units, a three-dimensional wind speed can be calculated if the orientation of the three acoustic paths is known. The resolution for the wind speed measurements is 0.01 $\frac{m}{s}$ in a range from 0 to 40 $\frac{m}{s}$. The accuracy is $s_u = \pm 1\% \pm 0.05 \frac{m}{s}$. For the wind direction, the resolution is 0.1° with an accuracy of $s_\phi = \pm 2°$ (Manual, 2017).

Apart from that, the sonic anemometer can also measure the speed of sound c by

$$c = \frac{d}{2} \left(\frac{1}{t_{12}} + \frac{1}{t_{21}} \right) \tag{2.2}$$

The speed of sound depends on the temperature and the water vapour content of the air by

$$c^2 = 402 \cdot T \left(1 + 0.32 \frac{e}{p} \right) = 402 \cdot T_s \tag{2.3}$$

with the actual air temperature T, water vapour pressure e and pressure p (Kaimal & Businger, 1963). T_s is the sonic temperature which is output by the anemometer. The sonic temperature is approximately equal to the virtual temperature $T_v \approx T_s$. The virtual temperature is the temperature that dry air would have, if its density and pressure were the same as that of the regarded moist air. The virtual temperature is used e.g. for calculating the buoyancy of an air parcel. The resolution of the sonic temperature is 0.01 °C with an accuracy of $s_{T_s} = \pm 2$ °C (Manual, 2017).

The thermohygrometer uses a Pt100 resistance sensor for the temperature measurement and a capacitive thin film polymer sensor for measuring the relative humidity RH. The accuracy of the thermohygrometer at measuring the temperature is $s_T = \pm(0.226 \text{ °C} - 0.0028T)$, the accuracy for the relative humidity is $s_{RH} = \pm 1$ % for $RH \leq 90$ % and $s_{RH} = 1.7$ % for strong humidity 90 % $< RH \leq 100$ % (Vaisala, 2012). From the relative humidity and the temperature, the water vapour pressure e is calculated by the data logger according to Lowe (1977).

The data is output with a frequency of $f = 20$ Hz for the three forested sites (chap. 2.3 - 2.5) while for the Botany and Plant Pathology site (chap. 2.2) the output frequency is $f_{\text{BPP}} = 10$ Hz. The response time of the thermohygrometer however is $T_{\text{response}} = 60$ s for a response of 90 % (Vaisala, 2012). The data is stored in hourly files on a permanent storage archive at the *btgmm6*-server.

2.2 Botany and Plant Pathology site

The only unforested site of our analysis is the Botany and Plant Pathology site (BPP). This site is located in the Willamette river valley, 3 km east of Corvallis, Oregon, USA at 67 m above sea level (44.57°N, 123.24°W). The only slightly undulating landscape around this site is mainly used by agriculture and thus covered by a mix of orchards, hedges, crops and a few small buildings (Zeeman *et al.*, 2015). The main study site is situated on grassland within a shallow depression that is about 20 m across, 50 m long and 1-2 m deep (Mahrt & Thomas, 2016). At the main site, 8 SUSAN stations (SUSAN A1 to A4 and SUSAN C1 to C4) were deployed during a period from 23 August to 14 October 2011. In addition to that, 2 further sonic anemometers (METEK USA-1) were deployed at the main site (model USA-1, Metek
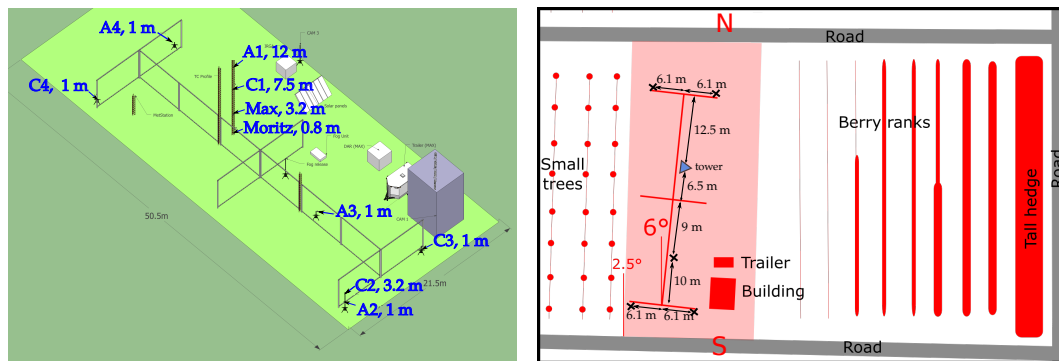
Figure 2.2: Locations of the 10 sensors (8 SUSANs and 2 extra METEK sonic anemometers at the main site at BPP (Drake *et al.*, 2012b).

GmbH, Elmshorn, Germany), which are called Max and Moritz (fig. 2.2). Other instruments were deployed at the site as well but we will only analyse data from the SUSAN units and the two additional sonics Max and Moritz. The measurement area is about 38 m long and 12 m wide and the longitudinal axis has an azimuth of 6°. The sensors are arranged on tripods in a ground network at one meter height above ground (A2-A4, C3, C4). Additionally there is a tower with four sonic anemometers up to a height of $h_{A1} = 12$ m for profile measurements and one sensor at $h_{C2} = 3.2$ m above the sensor A2 (see fig. 2.2). The distances between the single sensors can be learned for the picture at the right in figure 2.2, where the sensor locations are marked with small crosses.

Apart from the main site, there is an additional smaller site at a distance of about 1 km to the north-north-east which is called the Moritz site. Also the Moritz site is situated on grassland. To the north of this secondary site runs a small river with dense shrubs at the banks. On the other sides, there is the same mix of scattered trees and grassland as at the main site.

At the Moritz site, the remaining four SUSAN units (SUSAN B1-B4) are deployed with slightly bigger distances between the individual sensors than at the main site.
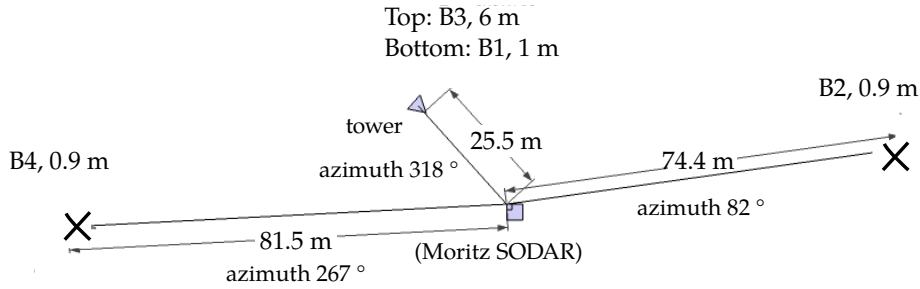
Figure 2.3: Spatial distribution of the four remaining SUSAN units at BPP that were deployed at the Moritz site in a distance of 1 km from the main site (Drake *et al.*, 2012*b*).

Figure 2.4: Satellite image of the surrounding landscape at the BPP main site.

Two of the SUSAN units are deployed on a small tower in a height of $h_{B1} = 1$ m and $h_{B3} = 6$ m above ground (fig. 2.3). The others are situated on tripods at a height of $h_{B2} = h_{B4} = 0.9$ m. Thus, there is data from a ground network at about 1 m height above ground from the Moritz site at BPP, too.

Figure 2.5 shows the typical behaviour of the wind velocity and the static stability at the BPP main site at two different heights during the course of the day as well as a distribution of wind directions. For calculating the plots, wind velocities and temperatures and wind directions from the Bmmflux program are used. This program computes, amongst others, a time series of the wind velocity, temperature and wind direction with a temporal resolution of one minute from the original 10 Hz data (see chap. 3).

For the wind velocity, the ensemble-averaged value as well as the standard deviation is calculated for each minute during a period of one month (i.e. the average velocity and standard deviation for all the minutes between 00:00 and 00:01 during one month, the average velocity and standard deviation for all the minutes between 00:01 and 00:02, etc.). Taking a longer period than one month does not make sense due to the
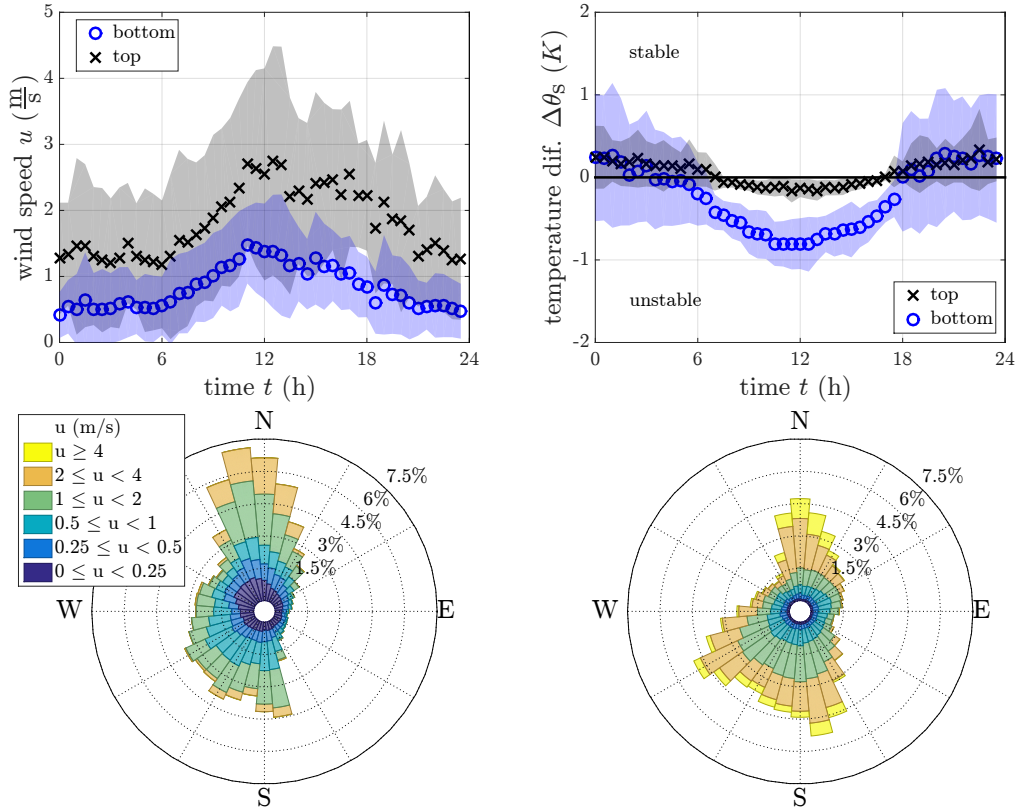
Figure 2.5: *Top left:* Diurnal course of the wind speed at 0.8 m ($\triangleq$ bottom, Moritz sensor) and at 12 m ($\triangleq$ top, A1 sensor). *Top right:* Diurnal course of the static stability measured by the temperature difference between 0.8 m and 3 m ($\triangleq$ bottom, Moritz and Max sensor) and between 7.5 m and 12 m($\triangleq$ top, C1 and A1 sensor). *Bottom left:* Distribution of wind velocities and wind directions at 0.8 m height (Moritz sensor). *Bottom right:* Distribution of wind velocities and wind directions at 12 m (A1 sensor).

annual course, as this only increases the standard deviation but changes nothing on the general course of the graph except for a constant offset (not shown).

The diurnal course calculated this way is shown in the top left plot of figure 2.5 for the Moritz sensor a t 0.8 m and the A1 sensor at 12 m height above ground. For visual clarity, only two points per hour are depicted. The standard deviations during the depicted minutes is indicated by a grey or blue background, respectively. As expected, the wind speed at the top sensor is higher than the one at the bottom sensor throughout the day. The speed at the bottom is lower due to the closer proximity to the ground which slows down the flow because of the surface drag. Furthermore, wind speeds are higher during the day than during the night for both sensors. This

is reasonable as during the night there is no forcing due to the solar radiation. The basic form of the wind speed's diurnal course however is the same for both heights. At the top sensor, the average wind speed during the day goes up to $3 \frac{m}{s}$ and only rarely reaches beyond $4 \frac{m}{s}$. At night, the average wind speed at the top sensor is slightly higher than $1 \frac{m}{s}$. For the bottom sensor, wind speeds during the night are rarely higher than $1 \frac{m}{s}$ while the average wind speed during the day is around $1.5 \frac{m}{s}$. In literature, situations with wind speeds lower than 1.5 to $2 \frac{m}{s}$ are frequently called weak-wind situations (Anfossi *et al.* 2005; Mortarini *et al.* 2013). It is thus evident from figure 2.5 that the BPP site is perfectly fit for analysing weak-wind situations on open grassland sites.

For the diurnal course of the static stability, the difference between the potential sonic temperatures of two sensors on top of each other is used.

$$\Delta\theta_s = \theta_{top} - \theta_{bottom} \tag{2.4}$$

The sonic potential temperature can be calculated from the sonic temperature by

$$\theta_s = T_s \left(\frac{p_0}{p}\right)^{\frac{R}{c_p}} \tag{2.5}$$

with the gas constant of air R and the specific heat capacity at constant pressure c_p. The sonic temperature T_s is given by the sonic anemometers (see chap.2.1). The potential temperature is the temperature an air parcel of pressure p had if it was adiabatically compressed to the reference pressure p_0, which is the pressure at sea level. The sonic temperature then takes into account the effect of different humidities on the buoyancy. This rescaled measure of temperature is used so that the temperature from air parcels at different heights and with different humidities can be compared. For $\Delta\theta_s > 0$, the density of the air at greater height is smaller than at lower height, which corresponds to a statically stable stratification and vice versa.

Figure 2.5 shows the diurnal course of the potential sonic temperature difference between the Moritz sensor ($h_{Moritz} = 0.8$ m) and the Max sensor ($h_{Max} = 3$ m) as well as between the C1 sensor ($h_{C1} = 7.5$ m) and the A1 sensor ($h_{A1} = 12$ m). As expected, statically stable situations prevail at night because of the radiative cooling that happens at the ground. During the day stratification is always unstable because also during the day, the radiative transfer happens right at the ground. This is also the reason, for the larger diurnal variations at the bottom sensors (i.e. closer to the ground where the transfer happens) compared to the sensors located aloft.

The two bottom plots of figure 2.5 show the distribution of wind directions for the Moritz sensor ($h_{Moritz} = 0.8$ m) at the left and the A1 sensor ($h_{A1} = 12$ m) at the right. The length of the bars in the circular histogram represents the frequency of the single wind directions with each group spanning an angle of 10°. Additionally, the two plots show very roughly the distribution of wind velocities. This is done by dividing the bars of the different wind directions into up to 6 differently coloured sections. The different colours indicate different intervals of wind velocities. From the right one of the two wind roses one can thus for example conclude that in about

1.5% of all cases, the wind comes from the north with a wind velocity less than $1 \frac{m}{s}$. All in all, the probability of the wind coming directly from the north for this sensor is slightly more than 4.5%.

Just like the diurnal course of the wind velocity at the two sensors, also the wind roses show that wind speeds at the A1 sensor are generally higher than at the Moritz sensor. Wind speeds higher than $4 \frac{m}{s}$ never occur at the Moritz sensor and wind speeds higher than $2 \frac{m}{s}$ only occur for northerly or southerly winds. This corresopnds also to the preferred wind directions. Winds from the east or the west, occur less frequently and generally have speeds less than $1 \frac{m}{s}$. This might be caused by the shallow depression in which the sensors are located, which channels the flow.

At the upper sensor, the preference of northerly or southerly winds is less pronounced because this sensor is situated above the shallow depression. Instead, there is an additional wind direction that occurs very frequently from the west-northwest ($\phi = 240°$). This indicates quite frequently happening directional shear of the wind. Nevertheless, also for the upper sensor, winds from the east or the west are on the whole lower than the ones from north or south.

2.3 Metolius Ponderosa Pine site

The Metolius Ponderosa Pine site (MP) is located on the east of the Cascade Mountains near Sisters, Oregon, USA at an elevation of 1253 m above sea level (44.451°N, 121.558°W). The site is covered by a sparse ponderosa pine forest with a tree density of approximately 325 trees ha^{-1} and a very low leaf area index of $LAI \approx 2.8 \frac{m^2}{m^2}$ (Irvine *et al.*, 2008). The canopy extends from 10 m to 16 m above ground. The understorey is sparse and consists of few 1 m tall shrubs. Because of the sparse tree density, understorey as well as forest floor can be reached directly by sunlight during the day and are open to the sky at night which results in a large diurnal cycle of stability of the air within the subcanopy (Vickers *et al.*, 2009). The MP site is part of the AmeriFlux network (US-Me2).

The sensor network is located at a flat saddle which is about 500 m wide. The
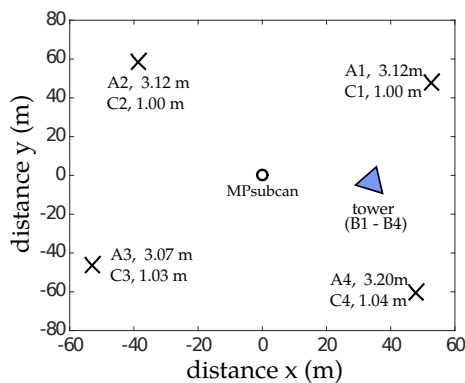
Figure 2.6: Layout of the experimental setup at the MP site. The locations of the sensors used for this study are marked with crosses or a triangle for the tower respectively. No analysis is done here with data from the additional tower MP subcan, which is shown for the sake of completeness.
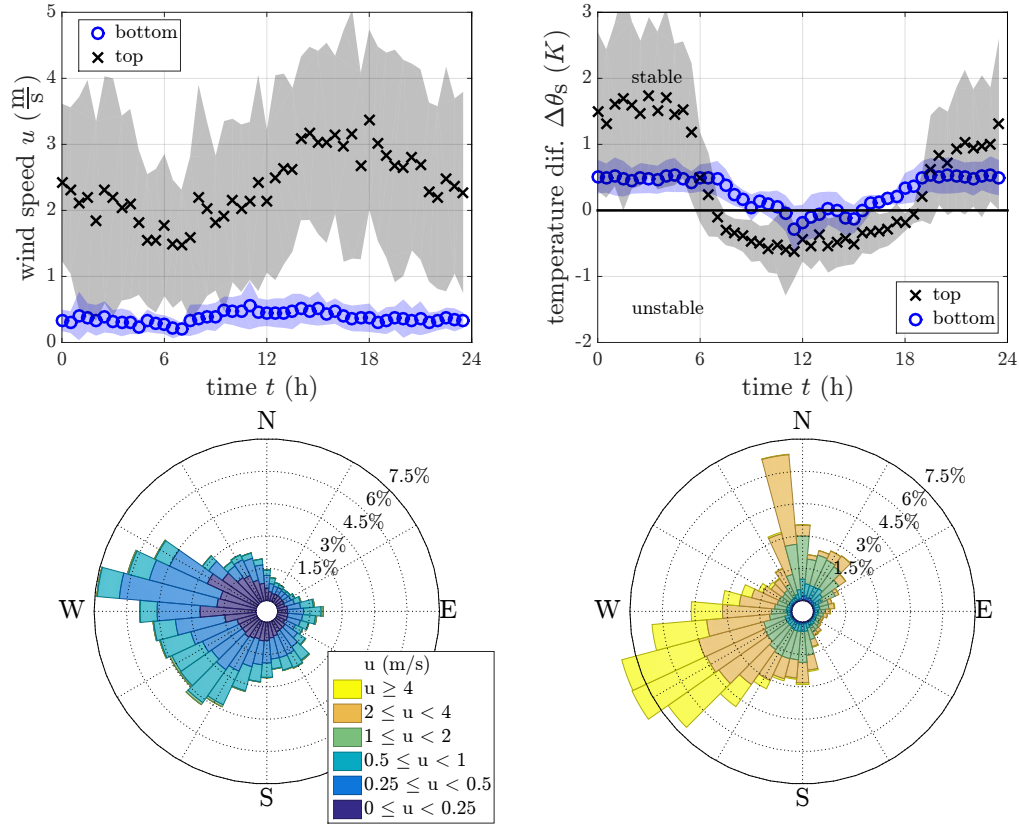
Figure 2.7: *Top left:* Diurnal course of the wind speed for the MP site at 1 m height ($\triangleq$ bottom, C2 sensor, within subcanopy) and at 30.7 m height ($\triangleq$ top, B1 sensor, above canopy). *Top right:* Diurnal course of the static stability measured by the temperature difference between 1 m and 3 m ($\triangleq$ bottom, C1 and A1 sensor) and between 16.8 m and 30.7 m height ($\triangleq$ top, B2 and B1 sensor). *Bottom left:* Distribution of wind velocities and wind directions at 1 m height (C2 sensor). *Bottom right:* Distribution of wind velocities and wind directions at 30.7 m height (B1 sensor).

surrounding topography however is very anisotropic, rising to the northwest, west and southeast, flat to the southwest and east and falling to the north, south and northeast (Vickers *et al.*, 2012).

Also at the MP site, there is a ground network of sensors at 1 m height above ground arranged approximately in a rectangle (SUSAN C sensors, see fig. 2.6). The SUSAN A sensors are located exactly above the C sensors and form a second network at a height of 3 m. The SUSAN B sensors are all placed on a tower which is situated on the eastern side of the rectangle. Their heights above ground are $h_{B1} = 30.65$ m , $h_{B2} = 16.75$ m, $h_{B3} = 5.8$ m and $h_{B4} = 0.125$ m. Thus, the B4 sensor measures the flow directly above the ground, the B3 sensor in the middle of the clear bole space,

the B2 sensor at the top of the canopy and the B1 sensor about 14 m above the canopy top.

The measurements at the MP site were conducted in the period from 25 June to 5 August 2014.

The diurnal courses of the wind velocity as well as static stability and the wind roses shown in figure 2.7 were produced as described in chapter 2.2. For the diurnal course of the wind speed, data are used from the C2 sensor ($h_{C2} = 1$ m) for the ground network and from the B1 sensor ($h_{B1} = 30.7$ m) for the above canopy. Large differences in the flow statistics between the C2 sensor and the B1 sensor become evident. The B1 sensor shows a clear diurnal cycle with the maximum wind velocities in the early afternoon. The average diurnal cycle goes up to around 3.5 $\frac{m}{s}$ but the standard deviation is quite large so that wind speeds up to nearly 5 $\frac{m}{s}$ may happen. During the night, wind velocities are around 2 $\frac{m}{s}$ and rarely fall below 1 $\frac{m}{s}$. Thus, wind velocities at the high B1 sensor at MP are higher than the wind speeds of the upper sensor at the BPP site, especially during the night.

At the ground network however, wind speeds are generally very weak. Within the range of the standard deviation even the wind velocities during the afternoon never exceed 1 $\frac{m}{s}$. With the axis range necessary for showing the diurnal cycle of the upper sensor, a maximum of the wind speed at the C2 sensor during the day cannot even be seen due to its small amplitude. Actually there is a small maximum around noon, albeit not a very pronounced one. All in all, at the MP site, the upper sensor shows a very clear diurnal cycle with a strong maximum while the wind speeds at the ground network sensor stay very low all the time so that the cycle is not very distinct.

The reason for this different behaviour compared to the BPP site is mainly the presence of a canopy between the two sensors used for the analysis, which acts as a barrier and a momentum sink. Additionally, the distance between the upper and the lower sensor is much bigger at the MP site than at BPP.

The presence of the canopy is also responsible for a difference in the diurnal course of the stabilities at the MP site compared to BPP. As at BPP, both, within the subcanopy and above the subcanopy, stable stratification prevails at night while unstable stratification can be found during the day. However, at MP, the diurnal cycle of the ground network is much less pronounced than the one above the canopy. This is caused by the exchange of energy partly happening within the canopy and by the canopy slightly acting as a insulator despite its sparseness. The behaviour described here can be observed independent of which subcanopy sensors are taken for determining the subcanopy stability. For the plot above, sensors C1 and A1 are used. For the above canopy, sensors B2 and B1 are used as these are the two highest ones. The wind roses at the bottom of figure 2.11 indicate a preference for winds from the west at the sensor C2 within the subcanopy. This presence can also be found at the other subcanopy sensors, even if it is somewhat less distinct at the C4 sensor (not shown). Above the canopy (sensor B1), the preferred direction is slightly shifted to the south with an additional peak for winds from the north. Thus, also at MP some directional shear can be found during most of the times. Within the subcanopy winds rarely get higher than 0.5 $\frac{m}{s}$ and are thus much lower than the winds at the ground

network of the BPP site. Above the canopy it is remarkable that the strongest winds are associated with south-westerly wind directions, which also corresponds to the preferred wind direction. This is probably caused by a channelling of the flow due to the surrounding topography (falling to the northeast and flat to the southwest).

2.4 H. J. Andrews Experimental Forest site

The third study site lies within the HJ Andrews Experimental Forest (HJA). The HJA is a Long Term Ecological Research site and is located on the western slope of the Cascade Mountains in Oregon, USA. Elevations in the HJA range from 412 m above sea level to 1627 m above sea level within an area of 6400 ha (Daly *et al.*, 2010). The site is distributed over Watershed 1, which is a steep basin ranging from 400 m to 900 m above sea level with slopes nearly up to 40° (see left plot, fig. 2.8). At the bottom of Watershed 1, there is a big reservoir. In this study, HJA is the site with the most extreme topography. We expect this to lead to a strong nocturnal drainage flow when synoptic forcing is absent (Drake *et al.*, 2012a). The basin was
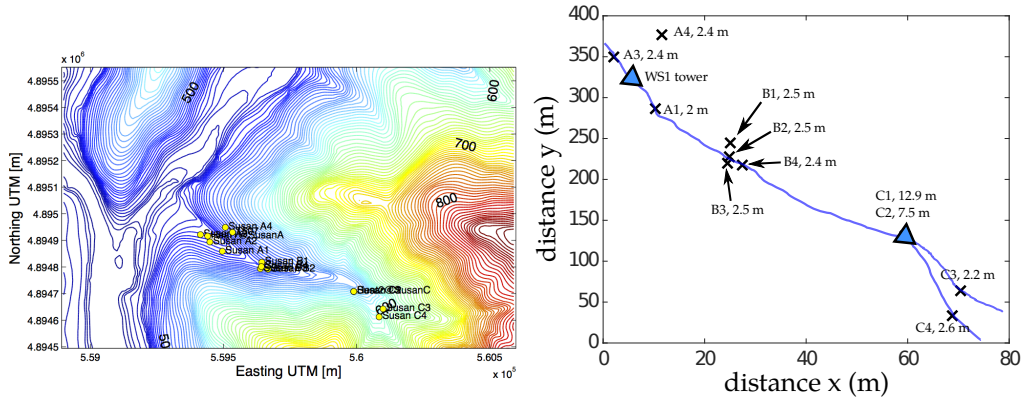
Figure 2.8: *Left*: Topographic map of Watershed 1 in the HJA (taken from Drake *et al.* (2012a)) The coloured lines indicate the height above sea level from 400 m (blue) to 900 m (dark red); *Right*: Spatial distribution of the sensor network; The blue line indicates the valley bottom.

logged in the 1960's and has since then regrown a dense canopy mainly composed of Douglas Fir with a canopy height ranging from $h_c = 19$ m at the steep slopes to $h_c = 28$ m at the valley bottom. There is also a dense understorey composed of rododendron, salal and Oregon grape with a height of approximately 1 m and a mid-storey that e.g. contains big-leaf maple. The overall plant area index ranges from $PAI = 2.9 \frac{m^2}{m^2}$ to $PAI = 10.4 \frac{m^2}{m^2}$ (Thomas *et al.*, 2015) and is approximately $PAI \approx 4 \frac{m^2}{m^2}$ on average.
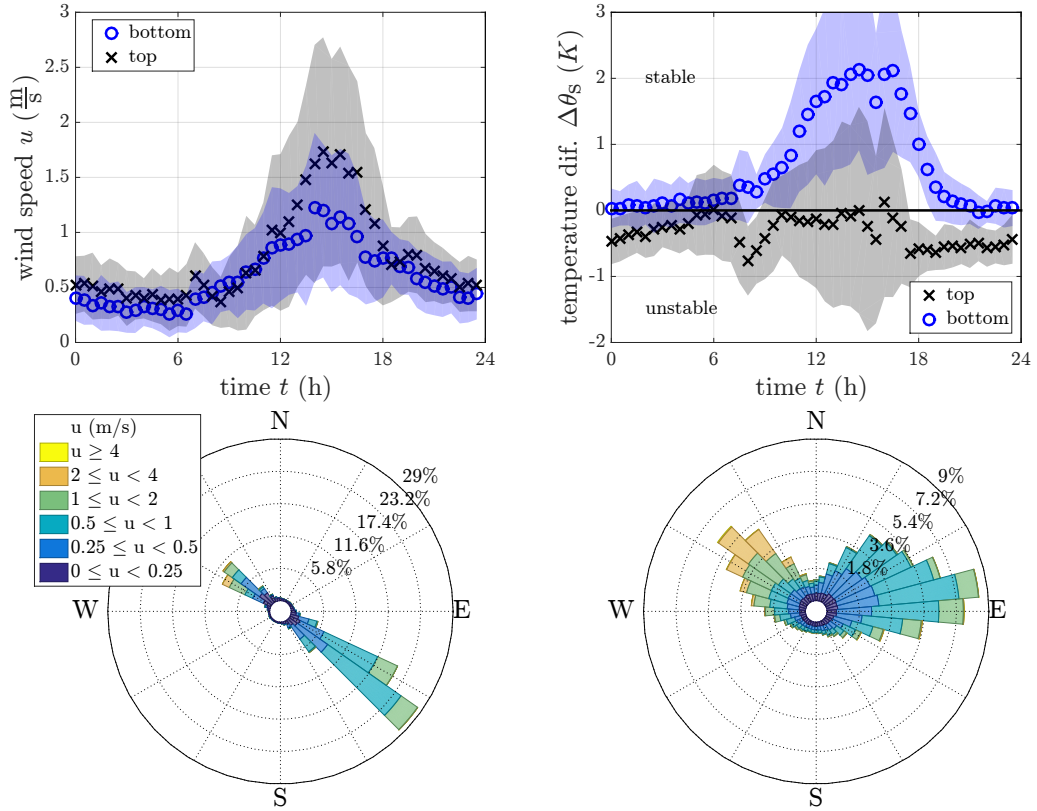
Figure 2.9: *Top left:* Diurnal course of the wind speed at 2 m height ($\triangleq$ bottom, A3 sensor, within subcanopy) and at 38 m height ($\triangleq$ top, WS1top sensor, above canopy). *Top right:* Diurnal course of the static stability measured by the temperature difference between 4 m and 15.8 m height ($\triangleq$ bottom, WS1sub and A2 sensor) and between 15.8 m and 38 m height ($\triangleq$ top, A2 and WS1top sensor). *Bottom left:* Distribution of wind velocities and wind directions at 2 m height (A3 sensor). *Bottom right:* Distribution of wind velocities and wind directions at 38 m height (WS1top sensor).

At HJA, the sensors are arranged in three groups mostly along the valley floor. The valley floor is illustrated by the blue line in figure 2.8. At this site, the ground network is located at 2 m height because of the dense understorey, which reaches up to 1 m height.

Starting at the reservoir and moving up the watershed, the first group consists of the SUSAN A sensors. Sensors A1-A3 are arranged along the valley floor while sensor A4 measures the flow on a small clearing at the north-western slope. Sensor A2 is located on the WS1 tower at the bottom of the canopy in a height of $h_{A2} = 15.8$ m. On the WS1 tower, there are 2 additional sonic anemometers. The lower one (CSAT

3, Campbell Scientific, Logan, UT, USA) is called WS1sub and is located within the subcanopy at a height of $h_{\mathrm{WS1sub}} = 4$ m. The higher one (R2, Gill Instruments Ltd., Lymington, UK) is called WS1top and is fixed above the canopy at a height of $h_{\mathrm{WS1top}} = 38$ m.

The second group is composed of the SUSAN B sensors, which are all part of the ground network at 2 m height. Sensors B1-B3 form a cross-section of the valley, with B1 at the north-western slope, B2 at the valley bottom and B3 at the south-eastern slope. B4 is located a bit upstream of this cross-section at the valley bottom.

The last group consists of the SUSAN C sensors and is located even farther up in the region of the bifurcation of the valley. Sensors C1 and C2 are both fixed on a tower right at the bifurcation while sensor C3 is in the northern and C4 in the southern branch.

The measurement period at HJA is from 14 July to 17 September 2012. In the first month however there are a lot of gaps in the data of the SUSAN C sensors due to problems with the power supply. Continuous data are available for SUSAN C starting from 14 August 2012.

At HJA, within the subcanopy as well as above the canopy, weak winds around $u = 0.5 \frac{\mathrm{m}}{\mathrm{s}}$ prevail during the night (fig. 2.9, top left plot). They are probably mainly determined by cold air drainage down the valley. During the day, wind speeds get much higher, both within the subcanopy (sensor A3) and above the canopy (sensor WS1_Top). In the diurnal course of the WS1_Top sensor, an additional small peak can be seen in the wind speed at around 7 AM, which is not present in the diurnal course of the subcanopy sensor. The time of occurence of this small bump coincides approximately with the time of sunrise. Drake *et al.* (2012a) also note that additional peak in the wind speed at HJA around sunrise that is present in the above canopy data, but not in the subcanopy data. They attribute it to a speedup of the cold air drainage flow or some larger scale mountain breeze. According to them, the speedup lasts until around 9:30-10 AM, when the directional variability of the wind starts to increase. This increase in directional variability during the day can be attributed to strong local heating, as this can induce a up valley breeze.

The diurnal course of the static stability (top right plot, fig. 2.9) within the subcanopy is calculated from the WS1_Sub sensor at $h_{\mathrm{WS1\_Sub}} = 4$ m and the A2 sensor at $h_{\mathrm{A2}} = 15.8$ m. The one above canopy is calculated from A2 and WS1_Top at $h_{\mathrm{WS1\_Top}} = 38$ m. In the subcanopy, the nights are clearly dominated by neutral stratification. This is caused by the cold air pool that lies within the valley during the nights. During the day, stratification in the subcanopy at the bottom of the valley becomes mostly stable. This is probably cause by the dense forest, as a big part of the exchange of energy happens within the canopy. Only little of the sunlight can actually reach and heat up the ground.

The diurnal course of the stability above the canopy looks quite peculiar, probably because the lower one of the two sensors from which is was calculated lies within the canopy instead of above. During the night, stratification is slightly unstable. This might indicate that the well-mixed cold air pool that renders the subcanopy neutral during the night does not reach up until above the canopy. Towards the morning,

stratification becomes more and more neutral until around 7 AM. This indicates that by morning, the cold air pool starts to grow up to this level. At the same time as the peak in the wind speed above canopy can be seen (around 7 AM), the stratification becomes suddenly unstable. Due to the temporal correlation of this drop in stability to the increase in wind speed we can assume that it is caused by the same larger scale mountain breeze as the peak in the wind speed. At the time when the small peak in the wind speed disappears and the larger diurnal peak in the wind speed develops, also the stratification gets more and more neutral again and stays neutral throughout the day. However, there is a large variability to the stratification during the day. Because of this and also due to the lower one of the two sensors for calculating the stability being within the canopy, the course of the above-canopy static stability during the day should not be overinterpreted.

The wind rose of a sensor within the subcanopy (A3 sensor, fig. 2.9, bottom left plot) shows a strongly bidirectional distribution. This corresponds to the wind going either up or down the valley. The wind rose thus represents the orientation of the valley near the observed sensor. For the sensor above the canopy, still a strong preference of the upvalley/downvalley direction can be recognized. It is however not as strong as within the subcanopy, possibly because it is more easily influenced by large-scale forcing.

2.5 Mary's River Douglas Fir site

The site with the densest forest is the Mary's River Douglas Fir site (MF). It is located in the coast range of Oregon (44.646° N, 123.551° W) at a height of 310 m above sea level. Like MP, this site is also part of the AmeriFlux Network (US-Fir). The site is surrounded by moderately complex, slightly sloped terrain with a flat saddle in the north-east at a distance of approximately 600 m.

The canopy is extremely dense with a plant area index of $PAI = 9.4 \ \frac{\text{m}^2}{\text{m}^2}$ and a mean canopy height of $h_\text{c} = 28$ m. The relatively sparse understorey consists mainly of Salal and has a plant height of approximately 0.8 m. Between the understorey and
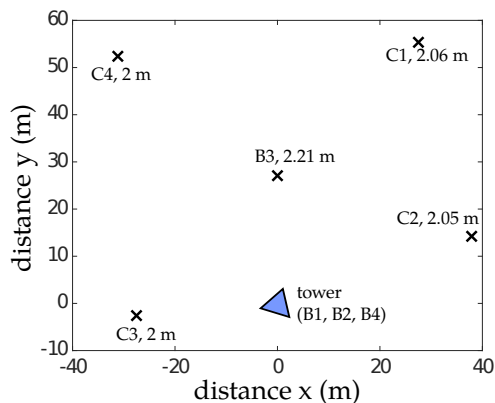
Figure 2.10: Layout of the experimental setup at the MF site
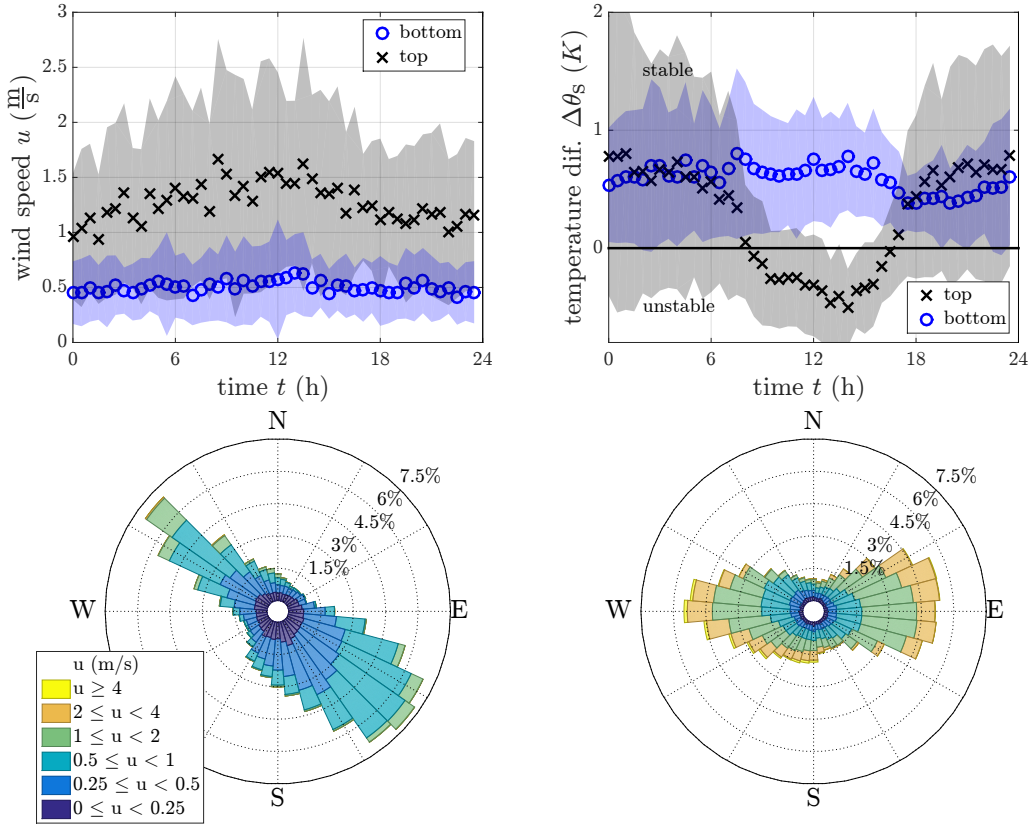
Figure 2.11: *Top left:* Diurnal course of the wind speed at 2 m height ($\triangleq$ bottom, C1 sensor, within subcanopy) and at 38.6 m height ($\triangleq$ top, B1 sensor, above canopy). *Top right:* Diurnal course of the static stability measured by the temperature difference between 2 m and 14.4 m height ($\triangleq$ bottom, B3/C3 and B2 sensor) and between 26.4 m and 38.6 m($\triangleq$ top, B4 and B1 sensor). *Bottom left:* Distribution of wind velocities and wind directions at 2 m height (C1 sensor). *Bottom right:* Distribution of wind velocities and wind directions at 38.6 m height (B1 sensor).

the canopy, there is a clear bole space which ranges approximately from 1 m to 15 m agl.

Due to the understorey, also at MF, the ground network is at 2 m height. It consists of the SUSAN C sensors which are arranged in a rectangle (side length around 50 m) and the B3 sensor in de middle of this rectangle (see fig. 2.10). The rest of the SUSAN B sensors is mounted on a tower which is located on the southern side of the rectangle. The heights of the sensors at the tower are $h_{B1} = 38.6$ m, $h_{B2} = 14.4$ m and $h_{B4} = 26.4$ m. Thus, in addition to the ground network, there is one sensor at the lower end of the canopy, one sensor at the upper end of the canopy and one sensor about 10 m above the canopy. The SUSAN A sensors were not operational at the

MF site due to a lightning strike. The measurement period at the MF site is from 20 September to 2 November 2013.

At the MF site, we expect a different stability behaviour compared to the open MP or BPP sites: Due to the dense canopy, radiative cooling happens mainly in the crown space. The stratification during the day should be more stable than the one during the night. On some days, stratification in the subcanopy might even be stable during the day and unstable during the night (Vickers *et al.*, 2009).

For the typical wind speeds at the MF site, data are taken from the C1 sensor ($h_{C1} = 2$ m) for the subcanopy and from the B1 sensor ($h_{B1} = 38.6$ m) for above the canopy (fig. 2.11, top left plot). As at the MP site, wind speeds are much lower within the subcanopy than above due to the trees slowing down the flow. Within the canopy, wind speeds higher than 1 $\frac{m}{s}$ are very rare while above the canopy occasionally wind speeds 4 $\frac{m}{s}$ may happen. Compared to the MP site however, above canopy winds are weaker at MF which is caused by topographic sheltering (Thomas *et al.*, 2013). Winds within the canopy are a little stronger at MF than at MP in spite of the MF forest being much denser. This is caused by the MF site being situated at a slope and thus influenced by cold air drainage. Furthermore, the bole space within MF between is free leading to a smaller drag and thus the flow within the bole space can develop more freely. At the MP site on the other hand, the crowns of the fewer trees have branches that reach down very far and so flow is inhibited strongly in the bole space. As a result, it is not surprising that the subcanopy flow is slightly stronger at MF than at MP, although the tree density at MF is higher.

For the stability above the canopy, data are used from the B4 and the B1 sensors. The expected diurnal cycle of stability is clearly visible (top right plot, fig. 2.11). It shows stable stratification during the night due to radiative cooling and unstable stratification during the day due to the solar irradiation heating up the canopy.

Unfortunately, there are no two sensors above each other in the subcanopy. As a workaround for getting the static stability, the mean potential temperature of the B3 and the C3 sensor is calculated (both at 2 m height). The static stability is then calculated from this average potential temperature and the one from the B2 sensor ($h_{B2} = 14.4$ m). The reason why the B3 and the C3 sensor are chosen out of all the ground network sensors is that those are the two closest ones to the B2 sensor. The result however doesn't depend on which sensors are chosen for determining the static stability within the subcanopy.

Figure 2.11 shows that there is very little diurnal variation in the static stability within the subcanopy. The temperature difference in the subcanopy is 0.5 K over a distance of 12.4 m. The same temperature difference can be found at the MP site over a distance of only two meters. Thus, the temperature gradient at the MF is very small and indicates a slightly stable to neutral stratification during all the day. The temperature gradient is slightly more stable during the day than during the night. The reason is that the exchange of energy happens mainly at the canopy as nearly no sunlight reaches the ground. The solar irradiation thus first heats up the higher layers of the subcanopy leading to a more stable stratification during the day. Similarly the energy loss of the canopy during the night and the cooling of the higher layers within

the subcanopy slightly diminishes the stability during the night. All in all however the subcanopy is very well isolated and stays nearly isothermal.

The wind roses for of the MF site (bottom plots, fig. 2.11) are produced using the data from the C1 sensor and the B1 sensor like the diurnal cycle of the wind speed. The preferred wind directions in the subcanopy are from the north-west as well as from the south east. There is again a directional shear as above the canopy there are mainly easterly or westerly winds. As from the diurnal cycle of the wind velocity we can also recognize from the colour code of the wind rose that the wind speed within the subcanopy of MF is not lower than the one at MP. Instead, actually more situations with wind speeds higher than $1 \frac{m}{s}$ can be found at the MF site in spite of the denser canopy. The reason for this is the clear bole space between the subcanopy and the canopy at MF, which enables the flow to speed up in this range. Furthermore, the location of the measurement site on slightly sloped terrain might lead to cold air drainage, which also leads to a speedup of the flow.

3 Data evaluation strategies in the atmospheric boundary layer

In order to get data on turbulence from the high-frequency wind and temperature data measured by the sonic anemometers that is comparable to other experiments, a number of methods typical in micrometeorology have to be applied. One of them is the block averaging method. In the following section, we will discuss block averaging and why it is necessary. Afterwards we will summarize the other methods that also are applied to our data.

3.1 Reynolds averaging

Since Osborne Reynolds, the principal strategy for studying turbulent flows is to separate the 'mean' part of the flow from the 'randomly' fluctuating part (Wyngaard, 2010). The mean portion is then treated deterministically, while for the turbulent portion statistic techniques are applied (Lee *et al.*, 2000). The separation of the turbulent from the non-turbulent part can be written as

$$u(\mathbf{x}, t) = \bar{u}(\mathbf{x}, t) + u'(\mathbf{x}, t) \tag{3.1}$$

where u' represents the fluctuating and $\bar{u}$ the 'mean' part of a flow, independent from the way the mean is derived. The ideal way of getting the mean part is an ensemble average

$$\bar{u}(\mathbf{x}, t) = \lim_{N \to \infty} \frac{1}{N} \sum_{n=1}^{N} u_n(\mathbf{x}, t) \tag{3.2}$$

where $u_n(\mathbf{x}, t)$ is the time-dependent velocity field $u(\mathbf{x}, t)$ in the n'th realization of an experiment (Finnigan & Shaw, 2008). The reason why ensemble averaging can be considered the ideal way of dividing a turbulent flow in its mean and fluctuating part is that it obeys the so-called Reynolds averaging rules. Only for an averaging operator that obeys the Reynolds averaging rules, it is possible to fully separate the turbulent and the non-turbulent part in non-linear equations. These rules are (de Fériet 1951;

Monin & Yaglom 1971)

$$\overline{u + v} = \bar{u} + \bar{v} \tag{3.3}$$

$$\overline{c \cdot u} = c \cdot \bar{u} \text{ if } c = \text{const} \tag{3.4}$$

$$\bar{c} = c \text{ if } c = \text{const} \tag{3.5}$$

$$\overline{\frac{\partial u}{\partial x}} = \frac{\partial \bar{u}}{\partial x} \tag{3.6}$$

$$\overline{\bar{u}v} = \bar{u}\bar{v} \tag{3.7}$$

From eq. (3.7) it follows that

$$\bar{\bar{u}} = \bar{u} \tag{3.8}$$

and from the equations (3.3) and (3.8)

$$\overline{u'} = \overline{u - \bar{u}} = 0 \tag{3.9}$$

and finally from eq. (3.7) and (3.9)

$$\overline{\bar{u}u'} = \bar{u}\overline{u'} = 0 \tag{3.10}$$

Unfortunately, it is impossible to apply ensemble averages to data from measurements in the atmosphere or to large simulations. The reason for ensemble averages not being possible are the very variable and uncontrollable boundary conditions in the atmosphere or the too high computational costs respectively. As a result, it is necessary approximate the ensemble averages by either space (typical for simulations) or time averages. For atmospheric measurements where data is only available from very few fixed points, time averaging has to be chosen:

$$\bar{u}(\mathbf{x}, t) = \frac{1}{T_{\mathrm{p}}} \int_{t - \frac{T_{\mathrm{p}}}{2}}^{t + \frac{T_{\mathrm{p}}}{2}} u(\mathbf{x}', t') \mathrm{d}t' \tag{3.11}$$

For statistically steady flows it is possible to choose very long averaging times $T_{\mathrm{p}} \to \infty$ for which the conditions (3.3)-(3.7) are fulfilled. For atmospheric measurements however, there will always be some non-stationarity due to the diurnal course, changing cloud cover and many other factors, forcing one to choose a shorter averaging time $T_{\mathrm{p}} \ll \infty$. Therefore, the ergodic hypothesis has to be applied, which means that for an averaging time $T_{\mathrm{p}} \gg T_{\mathrm{I}}$ the temporal average is assumed to be equal to the ensemble average. T_{I} is the integral time scale of the turbulence, a measure for the memory of the flow (Finnigan & Shaw, 2008).

The most intuitive solution now would be to filter the raw data with a running average of width T_{p}. Unfortunately, this is not possible, because for non-stationary flows the running average does not satisfy the Reynolds averaging rules eq. (3.3) and (3.7). Because of that, compared to the ensemble average, a running average leads to additional terms when non-linear equations are averaged. The additional terms

are a mixture of turbulent and non-turbulent quantities. This might be desirable for some purposes (Finnigan & Shaw 2008; Germano 1987), but also complicates the interpretation regarding the interaction of the mean flow and the turbulence (Germano, 1992). Only for fully separated flows without (i.e. without mixed terms that combine turbulent and non-turbulent quantities), the mechanisms by which turbulent and non-turbulent quantities interact can be analysed directly.

Instead of the running average, it is common to use the block average. This means,
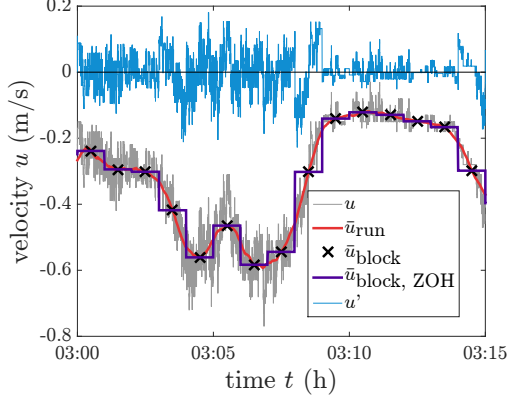
Figure 3.1: Time series of the raw data before (u, grey) and after filtering with a running average ($\bar{u}_{\mathrm{run}}$, pink), the reduced time series of the mean flow ($\bar{u}_{\mathrm{block}}$, black) and the 'expanded non-turbulent 'time series after application of the Zero Order Hold ($\bar{u}_{\mathrm{block,ZOH}}$, purple) as well as the time series of the perturbations (u', blue)
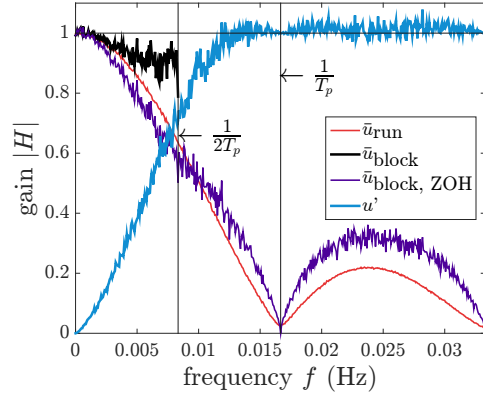
Figure 3.2: Magnitude of the frequency response of the running mean, the block average and the perturbation.

the time series is cut into single adjoining but non-overlapping pieces of length T_{p}, where T_{p} is called perturbation time scale. Each of these pieces is assumed to be one stationary realisation of an ensemble of possible realisations. From each piece, a single mean value (mean flow) is calculated as well as variances and covariances representing the turbulence (Rannik & Vesala, 1999).

Block averaging is equivalent to applying the running mean filter of width T_{p} (pink line in fig. 3.2), then retaining only one data point per T_{p} (black crosses). This reduced time series is considered as the mean, non-turbulent flow. For calculating the turbulent portion of the flow, it is assumed that the mean flow is constant for the period of $\frac{T_{\mathrm{p}}}{2}$ before and after each value of the reduced time series. This corresponds

to applying a Zero Order Hold to the reduced time series and shifting the new, re-expanded series back by $\frac{T_\mathrm{p}}{2}$ (purple line). The re-expanded time series will be called $\bar{u}_\mathrm{block,ZOH}$. It is then possible to get the turbulent perturbation by

$$u' = u - \bar{u}_\mathrm{block,ZOH} \tag{3.12}$$

In chapter A, the procedure of Reynolds averaging is shown a bit more in detail. From the time series of the perturbation (blue line, fig. 3.2), we can calculate statistical quantities like variances (e.g. $\sigma_u^2 = \overline{u'}$) and covariances (e.g. $\overline{u'v'}$), which describe the turbulence and the turbulent fluxes. These turbulent statistics are again calculated by block averaging in order to obtain the same resolution we have for the mean flow. This means, the Reynolds averaging process reduces the resolution of the time series from its original 20 Hz (10 Hz for BPP) to $\frac{1}{T_\mathrm{p}}$. In exchange for that we have gained separate data describing the mean flow on the one hand and the turbulence on the other hand. In the following, by $\bar{x}$ we mean the block average of the quantity x and by x' we mean the deviation of quantity x from this block average.

In figure 3.1 each step of the process of separating the perturbation from the mean flow is depicted. For this purpose, we use one velocity component (u) during an interval of 15 min from the sensor SUSAN_C1 at the MP experiment. As perturbation time scale and time constant for the moving average we use $T_\mathrm{p} = 1$ min. In the original time series (grey), we clearly see some rapid fluctuations. In addition to that, we can distinguish a 'slow' event with a duration of roughly $\tau \approx 10$ min. This slow event is also visible in the filtered time series $\bar{u}_\mathrm{run}$, $\bar{u}_\mathrm{block}$ and $\bar{u}_\mathrm{block,ZOH}$. The rapid fluctuations are suppressed in the filtered time series. In the perturbation u', the rapid fluctuations are visible but not the slow events.

Figure 3.1 suggests that the block average is able to capture the slow motions with $T_\mathrm{motion} \gg T_\mathrm{p}$. The high frequency motions with $T_\mathrm{motion} \ll T_\mathrm{p}$ are nicely captured by u' from eq. (3.12). Apart from that, we clearly see some jumps in the block averaged signal after the expansion by the Zero Order Hold. Physically, the jumps don't make much sense, but they are unavoidable if we want to separate the turbulent fluctuations from the mean flow in non-stationary conditions without any terms mixing those two quantities.

In order to better understand how the block average with its somewhat non-physical jumps affects the data, it is worth looking at its frequency response function $H(f)$. As we will work only with data that is already completely available, we are only interested in the gain $|H(f)|$ and will ignore the phase response of our filter.

For calculating the gain, one month of data from the SUSAN_C1 sensor at the MP site is used. We use again only the u-component, but the result depends neither on the component nor on the sensor or site chosen. For this period of time, an average spectrum for the filtered and the unfiltered time series as well as for the perturbation are calculated. This is done by dividing the time series of u into single periods of four hours u_k. For each complete four hour period, we calculate a spectrum U_k.

$$\mathcal{U}_k(f) = \frac{1}{\sqrt{2\pi}} \int\limits_0^{2\mathrm{h}} u_k(t) \exp(-2\pi i f t)\mathrm{d}t \tag{3.13}$$

In the end, we average over all the obtained spectra.

$$\langle \mathcal{U} \rangle(f) = \frac{1}{N} \sum_{k=0}^{N} \mathcal{U}_k(f) \tag{3.14}$$

The averaged spectra of the filtered time series and the perturbation time series are calculated in the same way. Subsequently, the frequency response function is calculated by

$$|H(f)| = \frac{\langle \mathcal{U}_{\text{filter}} \rangle(f)}{\langle \mathcal{U} \rangle(f)} \tag{3.15}$$

where $\mathcal{U}_{\text{filter}}$ can refer to the mean spectrum after any of the filtering steps.
In figure 3.2, the gain after the different filtering steps is shown. Additionally, the frequencies $\frac{1}{T_{\text{p}}}$ and $\frac{1}{2T_{\text{p}}}$ are marked by a vertical line. As expected, the gain of the running mean is

$$|H_{\text{run}}| = |\operatorname{sinc}(T_{\text{p}}f)| = |\frac{\sin(T_{\text{p}}\pi f)}{T_{\text{p}}\pi f}| \tag{3.16}$$

with its first zero at $\frac{1}{T_{\text{p}}}$. The gain for the block average $\bar{u}_{\text{block}}$ (fig. 3.2, black line) is even higher than the one for the running average $\bar{u}_{\text{run}}$ (pink line), at least within the range where the gain is defined for $\bar{u}_{\text{block}}$. This is only the case up to $\frac{1}{2T_{\text{p}}}$ due to the reduced sampling frequency. As a result of the reduced sampling frequency, events that take less than 2 minutes (or $2T_{\text{p}}$) cannot be recognized in the time series of the mean flow, because this corresponds to the Nyquist frequency. This is no problem since for the mean flow we are only interested in phenomena with a duration of a few minutes to hours. The reason for the gain of the block averages being higher than the one of the running average filter is that by reducing the resolution, the high-frequency part that remains after filtering with the running mean is aliased back into the spectrum. This is discussed by Kaimal & Finnigan (1994).
Surprisingly, after the re-expansion, the block averaging filter has a quite similar gain as the running mean. As we didn't include new information but only artificially streched the time series of the mean flow, the resulting gain for frequencies higher than $\frac{1}{2T_{\text{p}}}$ must be an artefact of the expansion. As this is only an intermediate step in order to calculate the turbulent perturbation, this will not be further investigated. For the perturbation, frequencies higher than $\frac{1}{T_{\text{p}}}$ are transmitted almost perfectly while frequencies much lower than $\frac{1}{2T_{\text{p}}}$ are strongly dampened (blue line, fig. 3.2). Frequencies $\frac{1}{2T_{\text{p}}} \lesssim f < \frac{1}{T_{\text{p}}}$ however are still to a big extent contained in the signal of the perturbation which should certainly be kept in mind when discussing time scales of turbulent motions.
Naturally, the above discussed process of separating the turbulence from the mean flow creates the problem of choosing the appropriate perturbation time scale T_{p}. By choosing this time scale, one automatically determines, up to which size an event is identified as turbulence and which events are recognized as part of the mean background flow. If one chooses a too short perturbation time scale, one ignores fluctuations at larger scales and may thus causes a systematic error. This is a problem

especially if the main interest is the turbulent fluxes (Lee *et al.*, 2000, chap. 2). On the other hand choosing a long time scale might include non-stationary in the single intervals. Furthermore, the more one expands the time scale T_p for the separation of turbulence and mean flow, the more the resolution is reduced of the time series of the mean flow. All in all, it is certainly necessary to keep in mind the purpose of the analysis when choosing the time-scale in order to find the best compromise (Vickers *et al.*, 2009).

We choose a perturbation time scale of $T_\mathrm{p} = 1$ min based on the findings of Vickers & Mahrt (2003). They find a gap in the cospectra of momentum flux and heat flux around a time scale of $T_{gap} \approx 1$ min and conclude that for scales larger than the gap scale, submeso motions are the main mechanism of transport. Since our aim is to study the influence of submeso motions on turbulence, it is necessary to separate those submesoscale motions from the fluctuating part and include them to the mean part of the flow. Hence we chose this comparatively short time scale knowing that we coincidentally exclude the larger scale vertical fluxes.

The Reynolds rules and its implications don't only apply to velocities, but also to any scalar of interest (e.g. temperature, concentration). In the following, $\bar{x}$ indicates the block average of the quantity $x(t)$ with a perturbation time scale of $T_\mathrm{p} = 1$ min. By x', we mean the perturbations from the mean of the respective block.

3.2 Eddy Covariance technique

Apart from block averaging, a number of other methods have to be applied to the data measured by the sonic anemometer in order to get meaningful results on turbulence characteristics. They are all part of a method named Eddy Covariance technique.

The Eddy Covariance technique is a statistical method for computing vertical turbulent fluxes by determining the correlation between the vertical wind velocity and any scalar of interest. The reason why this approach of measuring fluxes is reasonable is that in the atmospheric surface layer, where all our sensors are located, the turbulent fluxes represent the main mechanism of transport (Aubinet *et al.*, 2012). Before eventually the covariances and thus the fluxes are determined, a number of corrections, transformations and quality filtering need to be applied to the data.

Those corrections and calculations are all done by using the MATLAB program *bmmflux_process_mac.m* which was written by Prof. Christoph Thomas. In the following section, the corrections the program applies to our data are shortly described. After loading the first file starting from a user-determined starting time, *bmmflux* first controls the file for double or missing values and removes them or inserts NaNs at the missing values respectively. Then, the plausibility of the single measurement values is checked. The plausibility limits for this have to be predefined before in a configuration file. For the three velocity components, we choose the plausibility range of $|u_\mathrm{plaus}| \leq 30 \; \frac{\mathrm{m}}{\mathrm{s}}$. For the temperature we choose $-30°$ C $< T_\mathrm{plaus} < 50°$ C. All values outside this plausibility range are replaced by NaN for the further calculations. Subsequently, the data is despiked according to the method of Vickers & Mahrt (1997).

This is necessary because random electronic spikes can be created for example when water gathers at the transducers of the sonic anemometer during precipitation. For the despiking algorithm, a window of length $T_{\mathrm{despike}} = 5$ min is shifted over the time series. Within the window, the mean and the standard deviation are calculated. Every point that deviates more than 6.5 standard deviations from the mean is considered a possible spike. If less than four consecutive 'possible spikes' are detected, the identified data are replaced using a linear interpolation between the neighbouring data points. If four or more 'possible spikes' are detected in a row, they are considered real events and the data points are not replaced (Vickers & Mahrt, 1997). The process is repeated until no more spikes can be found with a maximum number of repetitions $N_{\mathrm{rep,\,max}} = 5$. The length of the sliding window, the maximum allowed standard deviation and the maximum number of repetitions can be set in the configuration file. The number of detected spikes, the number of data outside the plausibility limit and the number of NaN that were already contained in the data before the quality checks are then saved to a .csv-file and can be inspected for further control.

In the next step, the currently loaded file is divided into non-overlapping windows. The length of those windows is the perturbation time scale, which is set to $T_{\mathrm{p}} = 1$ min. The perturbation time scale also has to be set in the configuration file. The following steps are executed for the single averaging blocks individually. As soon as the final block within the currently loaded datafile is reached, the next datafile is loaded and all the corrections described above are applied again.

For the methods applied to the shorter intervals, first, a rotation of the coordinate system according to the triple rotation method by Wilczak *et al.* (2001) is conducted. This is necessary because the wind data from the sonic anemometer is aligned with the coordinate system of the anemometer and has no physical meaning. Our aim is now, to rotate our measurements to a coordinate system that is aligned with the mean wind direction. For this purpose, the original coordinate system is first rotated around its z-axis (vertical axis) so that

$$\bar{v} = 0 \tag{3.17}$$

Next, the coordinate system is rotated around its y-axis until

$$\bar{w} = 0 \tag{3.18}$$

Eq. 3.18 corresponds to applying the continuity equation by assuming that there can be no net vertical flow. After the second rotation, the x-axis of the new coordinate system is aligned with the mean wind direction. Both of the rotational angles for rendering $\bar{v} = 0$ and $\bar{w} = 0$ are written to a .csv-file by the *Bmmflux*-program.

From now on, the coordinates x, y or z or the wind components u, v or w will refer to this rotated coordinate system. The positive x-axis corresponds to the streamwise direction, the positive y-axis to the lateral and the positive z-axis to the vertical direction. This implies, that the orientation of our coordinate system can change for every new averaging block. Whenever velocity components in another coordinate system than the one rotated to the mean wind direction are meant, they

will be marked by a subscript (e.g. u_{NS}, v_{NS} and w_{NS} when talking about velocity components in the coordinate frame of the earth)

It is important to keep in mind that the rotation also affects the turbulence statistics, mainly acting as a high-pass filter for the atmospheric covariances. A detailed discussion of the consequences of the rotation can be found in Finnigan *et al.* (2003). Finally, mean values, variances and higher order moments as well as covariances of the three velocity components u, v, w (both, rotated and unrotated) and the sonic temperature T_{s} are calculated according to the Reynolds averaging scheme and written to the same .csv-file as the rotational angles. Additionally, many more typical meteorological and site-specific quantities are saved in this file. Most of the following work is based on some of the quantities calculated by the *bmmflux*-program.

4 Weak-wind situations

The submesoscale motions we are interested in are assumed to be present in all kinds of stabilities and for all wind speeds (Anfossi *et al.*, 2005). However they are dominant in stable weak-wind situations. Before analysing the different kinds of motions, it is thus sensible to define what is meant by a 'weak-wind situation'. In the following chapter we will develop a clear rule for deciding whether or not a given wind speed belongs to a 'weak-wind situation' by identifying a site-dependent weak-wind threshold.

4.1 Identification of weak-wind situations

For defining the weak-wind threshold, we use the dependence of the friction velocity u_* on the mean wind speed.

A similar method for the identification of wind regimes has been introduced by Sun *et al.* (2012), who used the dependence of the turbulent kinetic energy (TKE) $e = \sqrt{\sigma_u^2 + \sigma_v^2 + \sigma_w^2+})$ on the mean flow $\bar{u}$. They showed that in the low wind regime during the night, there is only a weak dependence of the TKE on the wind velocity. For stronger winds, the TKE starts to depend on the wind velocity $\bar{u}$ much more strongly. If the TKE is plotted in dependence of the mean flow, this behaviour of the TKE results in a curve with a shape that reminds of a hockey stick: It has a very small slope at for small winds, suggesting that at small wind velocities, the strength of the turbulence doesn't depend on the mean flow. At a certain velocity, there is a sudden increase of the slope which indicates, that for higher wind velocities, the turbulence intensity is determined by the mean flow. Sun *et al.* (2012) considered the wind velocity where the sudden increase of the slope happens as the threshold between two turbulence regimes.

Mahrt *et al.* (2015) showed, that also for many other turbulent quantities than the TKE, e.g. the standard deviation of the vertical velocity component $\sigma_w = \sqrt{\overline{w'^2}}$ or the friction velocity $u_* = \sqrt[4]{\overline{u'w'}^2 + \overline{v'w'}^2}$, the hockey stick like dependence on the mean flow can be found.

Mahrt & Thomas (2016) used the hockey stick curves of the friction velocity to identify a weak-wind limit a three different grassland sites. One of those is the grassland site BPP which is also used in this analysis. However, they used a different perturbation time scale than our $T_{\mathrm{p}} = 1$ min and also used only nighttime data.

In the papers cited above, the hockey stick method was only applied for grassland sites, while we will also apply it to data from the subcanopy. This however has very

recently also been done by Russell *et al.* (2016) who analysed the dependence of turbulence on wind velocity, stability, wind direction and sensor height within the canopy and day-or nighttime.

We will determine our site dependent weak-wind regime based on the hockey stick method from Sun *et al.* (2012), using the friction velocity as indicator for the strength of the turbulence. The friction velocity

$$u_* = \sqrt[4]{\overline{u'w'}^2 + \overline{v'w'}^2} = \sqrt{\frac{\tau}{\rho}} \tag{4.1}$$

is a density-independent measure of the shear strain in the vertical direction in units of a velocity. In turbulent flows, the shear is almost completely controlled by the turbulent fluctuations. Here, τ is the shear strain and ρ is the density of the air, which is e.g. dependent on the synoptic conditions.

Compared to the papers cited above, this work contains two novelties: First of all, we will not differentiate between nighttime and daytime data for the determination of the weak-wind threshold. The reason for this is the assumption, that submesoscale motions also exist during the day, even if they are more strongly pronounced during the night.

Apart from that we try using the scalar average wind speed

$$\bar{u}_{\mathrm{sc}} = \frac{1}{N} \sum_{i=1}^{N} \sqrt{u_i^2 + v_i^2 + w_i^2} \tag{4.2}$$
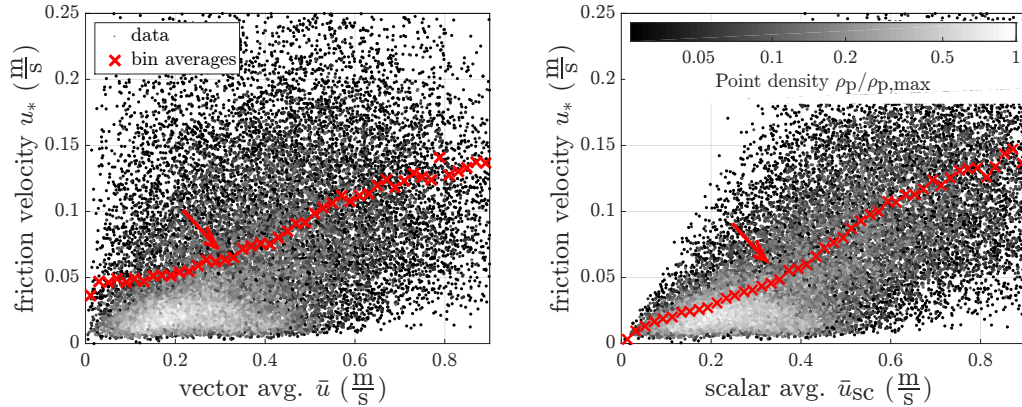
Figure 4.1: Dependence of the friction velocity on the vector averaged (left) and scalar averaged wind speed (right). The gray dots are the block averaged wind speeds and friction velocities. The brightness of the single points indicates their density. The red crosses are bin-averages of the single friction velocities and the red arrow roughly marks the transition point between weak wind and strong wind. The data shown here was measured by the SUSAN C2 station at the MP site during the complete measurement period.

of the single 20 Hz data instead of the formerly used vector average

$$\bar{u} = \bar{u}_{\mathrm{v}} = \sqrt{\left(\frac{1}{N}\sum_{i=1}^{N} u_i\right)^2 + \left(\frac{1}{N}\sum_{i=1}^{N} v_i\right)^2 + \left(\frac{1}{N}\sum_{i=1}^{N} u_i\right)^2} \qquad (4.3)$$

The vector average is, according to the Reynold's decomposition, considered as the mean, non-turbulent flow. On the contrary, the scalar averaged wind speed is a measure for the average momentum contained in the flow (non-turbulent and turbulent).

Here and in the following, when referring to the scalar average, this will be marked by an index 'sc' (i.e. $\bar{u}_{\mathrm{sc}}$) while we will continue calling the vector average $\bar{u}$.

Figure 4.1 shows a scatter plot of the friction velocity in dependence of the mean vector averaged and scalar averaged wind speeds. To provide visual clarity despite the huge number of data points, the dots are coloured according to their density using a logarithmic colour axis. A color bar is shown in the right plot of figure 4.1, demonstrating the logarithmic colouring of the points. The same scheme of point colors will be used in all scatter plots where the number of points makes such a color scheme necessary, without showing the color bar explicitly each time.

For visualizing the trend, figure 4.1 also shows bin averages of those data points. For calculating the bin averages, the data are distributed into bins according to their average wind speed ($\bar{u}$ or $\bar{u}_{\mathrm{sc}}$) with a equidistant bin width of $\Delta u_{\mathrm{bin}} = 0.01\ \frac{\mathrm{m}}{\mathrm{s}}$. This width corresponds to the resolution of the sonic anemometers (compare chap. 2.1). The red crosses are the average of all friction velocities within the respective bins. For visual clarity only every second bin average is depicted.

In the curve of the bin averages, there is a relatively flat region at small values of $\bar{u}$ and $\bar{u}_{\mathrm{sc}}$ (see ca. $\bar{u}_{\mathrm{sc}} = \bar{u} < 0.3\ \frac{\mathrm{m}}{\mathrm{s}}$). At higher velocities ($0.4\ \frac{\mathrm{m}}{\mathrm{s}} \lesssim \bar{u}(\text{or } \bar{u}_{\mathrm{sc}}) \lesssim 0.7\ \frac{\mathrm{m}}{\mathrm{s}}$), there is another region with a quite constant slope. The constant, positive slope of u_*
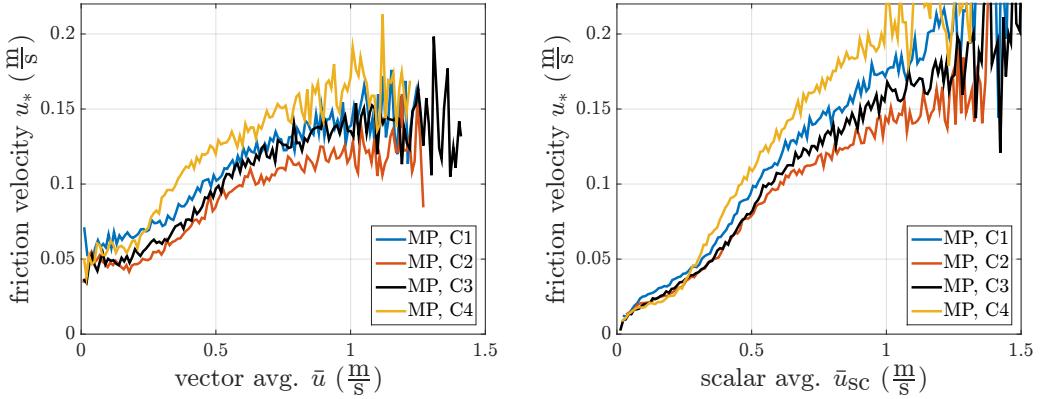
Figure 4.2: Dependence of the bin averaged friction velocity u_* on the vector averaged (left) and scalar averaged (right) mean wind speed for the four sensors of the ground network at MP. The single bin values are connected by a line for visual clarity.

in this region is the behaviour that is originally expected for all the data. It means that a higher mean flow or a higher average momentum of the fluid respectively, lead to stronger turbulence. In this region, the turbulence obeys the Monin-Obukhov similarity theory (Liang *et al.* 2014; Monin & Obukhov 1954).

We hypothesize that submesoscale motions are responsible for the reduction of the slope at low wind speeds, because they create additional turbulence. We will define the lower limit of the strong-wind regime as the point where the sudden change of slope happens. The approximate position of this threshold is marked with an arrow in both plots of figure 4.1.

Figure 4.2 shows the bin averaged friction velocities for the four stations of the ground network at the MP site. It is evident that within similar terrain, the trend of the friction velocities for increasing wind speed looks very similar. This is particularly pronounced for the scalar averaged version of the hockey stick plot (right plot in fig. 4.2), but also true for the vector averaged one. Moreover, the wind speed at the transition point seems similar in the vector averaged as in the scalar averaged case.

In contrast, figure 4.3 shows the bin averaged friction velocities of one ground
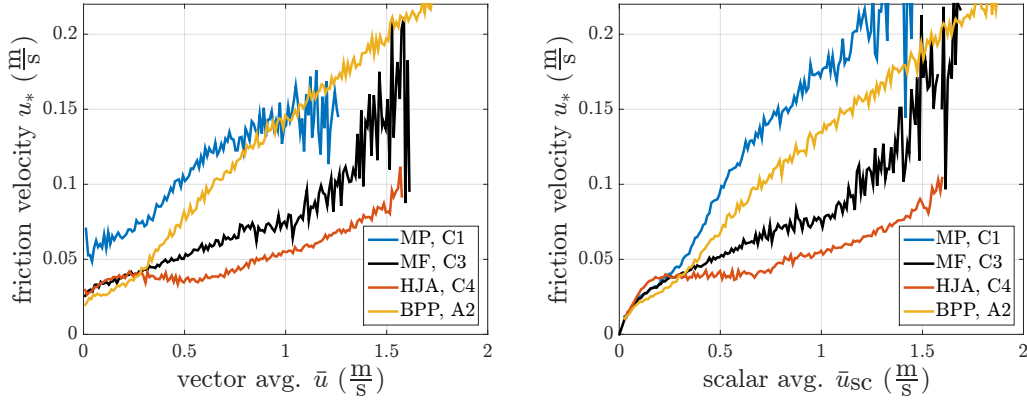
Figure 4.3: Dependence of the bin averaged friction velocity u_* on the vector averaged and scalar averaged mean wind speed for one ground network sensors for each of the four sites. The left plot contains the vector averaged wind speed, the right plot the scalar averaged version.

network sensor for each of the sites. One sees that the different terrains lead to strongly different hockey stick curves of the friction velocity. Not only the threshold itself is strongly site-dependent, but also the slope in the weak-wind as well as the strong-wind regime and the clarity of the transition point.

There is yet one site, at which also the single sensors show strongly different hockey stick curves within the site, namely the HJA site. This is no wonder however, since the HJA has a strongly variable topography. It even is possible to tell if a sensor is located at the slopes or at the valley bottom just by looking at the bin averaged hockey stick curves. On average, the turbulence is higher at the slopes (fig. 4.4, black and purple lines) than at the valley bottom (fig. 4.4, blue, orange and yellow lines).
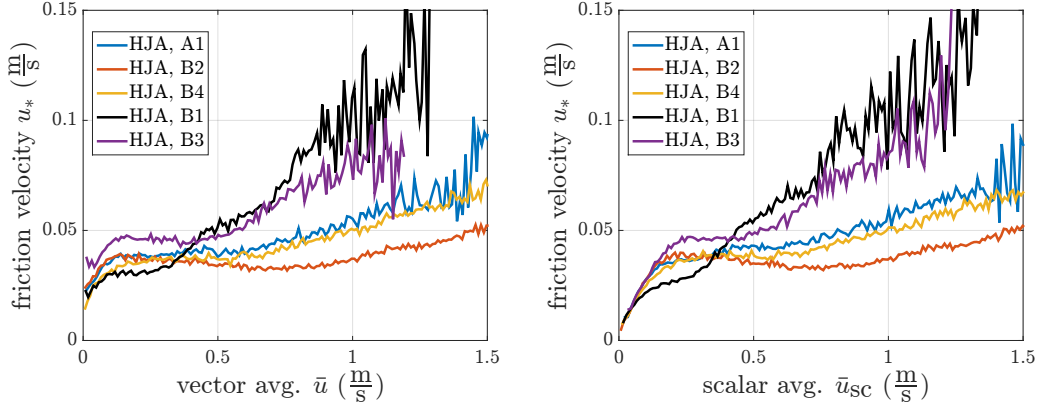
Figure 4.4: Bin averaged hockey stick curves for five stations of the ground network at HJA. Black and purple lines correspond to sensors at the side slopes, while the sensors of the blue, orange and yellow lines were located at the valley bottom. The left plot contains the vector averaged wind speed, the right plot the scalar averaged version.

Besides, for the slope-based sensors, turbulence already starts to depend on the mean flow at lower wind speeds (around $0.3 \frac{m}{s}$ to $0.5 \frac{m}{s}$) compared to the valley stations (around $0.6 \frac{m}{s}$ to $0.8 \frac{m}{s}$).

Apart from that, at every site, the curves from the above-canopy stations look different from the curves of the subcanopy stations (not shown). It is thus possible to conclude that the form of the hockey stick curves as well as the transition point from weak-wind to strong-wind regime are strongly influenced by the terrain and the vegetation.

The aim is now, to identify the transition point for every sensor by fitting a piecewise defined linear function

$$u_*(\overline{u}_{\mathrm{sc}}) = \begin{cases} m_1 \cdot \overline{u}_{\mathrm{sc}} + t_1 & \text{if } \overline{u}_{\mathrm{sc}} \leq u_{\mathrm{thr}} \\ m_2 \cdot \overline{u}_{\mathrm{sc}} + t_2 & \text{if } \overline{u}_{\mathrm{sc}} \geq u_{\mathrm{thr}} \end{cases} \tag{4.4}$$

to the hockey stick data, using m_1, m_2, t_1 and u_{thr} as fit parameters. t_2 is given by

$$t_2 = (m_1 - m_2) \cdot u_{\mathrm{thr}} + t_1 \tag{4.5}$$

because we postulate continuity. The threshold for the weak-wind regime is then given by u_{thr}. The same will be done using $\overline{u}$ instead of $\overline{u}_{\mathrm{sc}}$.

There is however one difficulty in finding the transition point by this piecewise linear fit. The problem is that at very low and at very high wind speeds, the curve of u_* is curved to the right for some of the sites (see figure 4.1 - 4.3), which hinders the fit. For the high wind speeds, this is the case for $\overline{u} \gtrsim 0.6 \frac{m}{s}$ ($\overline{u}_{\mathrm{sc}} \gtrsim 0.6 \frac{m}{s}$) at the MP and the BPP site. The reduction of slope at high wind speeds is also visible for some stations of the HJA site (stations A2, A3, A4 and C2, not shown). Here however, it starts at much higher wind speeds than at the BPP and MP sites ($\overline{u} \gtrsim 1 \frac{m}{s}$). At the

MF site, this behaviour is not observable at all. The reduction of the slope at high wind speeds was also noted by Mahrt *et al.* (2015). Unfortunately they didn't offer an explanation for this behaviour.

The strong curvature to the right at weak winds is more pronounced in the case of the scalar averaged wind speed, but also visible for the vector averaged case. This is somewhat intuitive because the scalar averaged mean wind speed also contains a turbulent component. That means, if the scalar average $\bar{u}_{\mathrm{sc}}$ goes to zero, this implies that not only the speed of the mean flow vanishes but also the turbulence. It is thus clear that for $\bar{u}_{\mathrm{sc}} \to 0$ also the turbulent quantity u_* has to vanish causing a downward turn. The downward bend at very weak winds is however also visible for the vector averaged version of the plot. At those curves, the friction velocity doesn't bend down to zero completely, but still a curve is recognizable for at least some stations at each of the sites. The strongest bend can be seen at the HJA site for both, the vector averaged and the scalar averaged version. At this site, the bend also reaches up to higher wind speeds (up to $\bar{u}_{\mathrm{sc}}0.3 \approx \frac{\mathrm{m}}{\mathrm{s}}$ for some stations) than at the other sites, where it never reaches wind speeds higher than $\bar{u} \approx 0.1 \frac{\mathrm{m}}{\mathrm{s}}$ ($\bar{u}_{\mathrm{sc}} \approx 0.1 \frac{\mathrm{m}}{\mathrm{s}}$). The problem is that for finding the transition point via fitting the piecewise defined linear function, in is necessary to exclude the two areas curved to the right. This however problematic since the physical reason for the additional curvature is unknown. Furthermore, it is impossible to use the same range of wind speeds for fitting at all the sites. This can be seen in figure 4.3. The transition point at the MF site lies around $\bar{u} \approx 1 \frac{\mathrm{m}}{\mathrm{s}}$ ($\bar{u}_{\mathrm{sc}} \approx 1 \frac{\mathrm{m}}{\mathrm{s}}$, black line). At this wind speed, the line of the bin averages is already curved to the right and thus has to be excluded at the BPP and MP site (blue and yellow lines). The transition at the BPP and MP site on the other hand happens around $\bar{u} \approx 0.3 \frac{\mathrm{m}}{\mathrm{s}}$ ($\bar{u}_{\mathrm{sc}} \approx 0.3 \frac{\mathrm{m}}{\mathrm{s}}$) and thus in a region that has to be excluded at some of the the HJA stations. The most problematic case is the HJA site. While at the other sites, the same range of $\bar{u}$ ($\bar{u}_{\mathrm{sc}}$) can at least be used for fitting all the ground network stations, the strong differences between the slope stations and the valley stations make this impossible at HJA.

But also for the other sites, it is necessary to adjust the fitting range for the sensors located higher within or above the canopy compared to the ones within the subcanopy. The ranges used for the fit can be seen in the appendix in tab. B.1. The fact that sensors in similar terrain have identical ranges suitable for fitting while different sites or sensor heights also have different fit ranges leads to the conclusion that also the curvature to the right is caused by an interaction of the flow with the landscape.

The result of the fit for one station of every site can be seen in figure 4.5. It is important to note that the fit was done using all the data points (grey dots) and not only the bin averages. The resulting curve however coincides very well with the bin averages, which confirms that the fit worked properly.

There are yet a few stations where no distinct threshold can be seen in the bin averaged curves. At those curves, the slopes of both lines of the fit either are extremely similar or the fitting function gives back a transition point at the very edge of the used fitting range with the first slope often being greater than the second one. In the latter case the fit probably identified one of the additional curved regions discussed above which
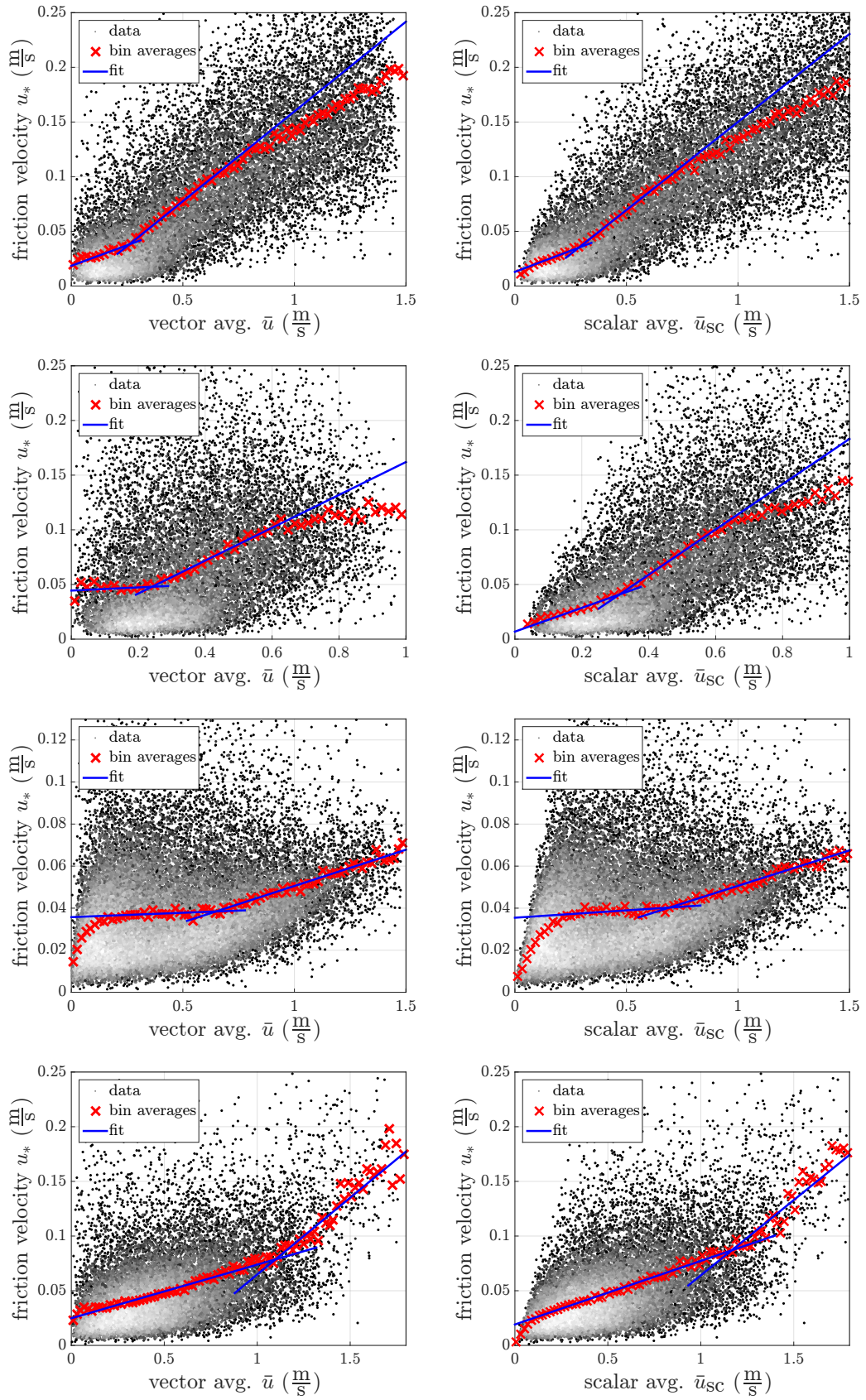
Figure 4.5: Hockeystick curves with fits for all sites, vector averaged version (left) and scalar averaged version (right). From top to bottom: BPP, MP, HJA, MF.

we actually intended to exclude by restricting the range of the fit. To be sure that the identified threshold is the desired threshold and does not correspond to one of the additional curved areas discussed above, we demand that the slope of the second interval is positive and bigger than the slope of the first line by at least 10%. Using this constraint, we successfully get a weak-wind threshold at 42 out of 44 stations when using the scalar averaged version. For the vector averaged one the fit works for 40 out of 44 stations. The only station that neither gives a threshold with the vector averaged wind speed nor with the scalar averaged, is station B4 at the MP site. This station however has a very special location at only 12.5 cm above ground. It can be assumed that because of the special location, the B4 sensor misses the main energy-containing turbulent eddies. It is thus no wonder that determining the weak wind threshold by the amount of turbulence fails at this station.

4.2 Which parameters impact the threshold velocity?

Table 4.1 shows a list of the resulting weak-wind thresholds for the vector averaged and the scalar averaged version. Besides, the table also contains the percentage of weak-wind situations for both options and the percentage of data that is attributed to a different regime when changing from vector to scalar average or vice versa.

station	$u_{\mathbf{thr}}$ $(\frac{\mathbf{m}}{\mathbf{s}})$ (vect)	ww (%)	$u_{\mathbf{thr}}$ $(\frac{\mathbf{m}}{\mathbf{s}})$ (scal)	ww (%)	Δ (%)
BPP, A1	0.92	27.8	0.98	28.75	1.8
BPP, A2	0.26	21.7	0.29	21.7	2.1
BPP, A3	0.27	24.1	0.19	14.07	10.1
BPP, A4	0.17	15.4	0.20	16.8	2.6
BPP, B1	0.38	31.9	0.40	28.3	5.0
BPP, B2	0.44	27.7	0.46	26.0	2.8
BPP, B3	0.63	36.6	0.55	26.4	10.13
BPP, B4	0.32	30.5	0.32	26.3	4.2
BPP, C1	0.87	31.8	0.70	22.7	9.1
BPP, C2	0.26	13.5	0.30	14.4	2.2
BPP, C3			0.33	23.5	
BPP, C4	0.21	18.6	0.25	19.9	2.6
MP, A1	0.27	32.7	0.32	28.2	12.3
MP, A2	0.30	31.6	0.35	31.9	11.6
MP, A3	0.37	39.3	0.37	28.4	10.8
MP, A4			0.28	24.1	
MP, B1	2.24	51.1	2.65	57.4	6.6
MP, B2			0.44	12.2	
MP, B3	0.26	31.9	0.30	27.0	11.7
MP, B4					
MP, C1	0.31	46.7	0.31	31.2	15.4

MP, C2	0.24	30.6	0.31	33.4	12.6
MP, C3	0.32	43.0	0.35	34.7	10.5
MP, C4	0.16	21.4	0.21	22.4	12.8
HJA, A1	0.63	75.5	0.70	79.9	4.8
HJA, A2	0.47	60.4	0.48	59.4	2.5
HJA, A3	0.56	57.0			
HJA, A4	0.55	75.5	0.47	63.5	12.1
HJA, B1	0.32	58.6	0.28	45.8	12.4
HJA, B2	0.78	67.3	0.79	67.4	0.3
HJA, B3	0.52	77.7	0.57	81.8	4.8
HJA, B4	0.65	67.1	0.69	69.7	2.7
HJA, C1	0.61	70.0	0.62	68.0	2.1
HJA, C2	0.55	53.1	0.59	55.9	3.76
HJA, C3	0.34	62.6	0.40	61.2	2.4
HJA, C4	0.60	61.8	0.67	64.8	3.8
MF, B1	0.46	15.1	0.53	15.8	3.0
MF, B2	0.67	92.4	0.71	91.7	2.0
MF, B3	0.69	81.0	0.94	92.0	11.1
MF, B4	0.25	53.15	0.33	52.7	13.6
MF, C1	0.92	91.7	0.96	92.0	1.0
MF, C2	0.88	94.1	0.90	93.8	0.7
MF, C3	1.15	98.5	1.16	98.2	0.4
MF, C4	1.10	94.7	1.17	95.4	0.9

Table 4.1: Thresholds of the weak-wind regime (columns 2 and 4), percentage of data that is weak wind (columns 3 and 5), percentage of data that is allocated to different regimes depending on whether the vector average or the scalar average is used (column 6) for all stations. Stations of the ground network are highlighted by a grey background.

It is evident that the resultant speed for the weak-wind threshold is very similar for scalar or vector averaged wind speed. Also the percentage of data classified differently is low for most stations (6% on average). The biggest number of differently classified data can be found at the MP site, although the threshold velocities are very similar. This will be discussed in chapter 4.3 (see fig. 4.13).

It was already mentioned, that a difference in the sensor height also leads to a difference in the hockey stick curve. This was also noted by Sun *et al.* (2012) who determined that at their grassland site, the weak-wind threshold increases approximately logarithmic with height. In order to compare this result to our data, figure 4.6 shows the relationship between the sensor height and the weak-wind threshold for the BPP (left) and the MF (right) sites. For both sites, the threshold value at the lowest height shown in the plot corresponds to the ground network. It is calculated by taking the average of all ground network stations of the respective site (marked grey in tab. 4.1). The errors are estimated by using the standard deviation of all thresholds from the
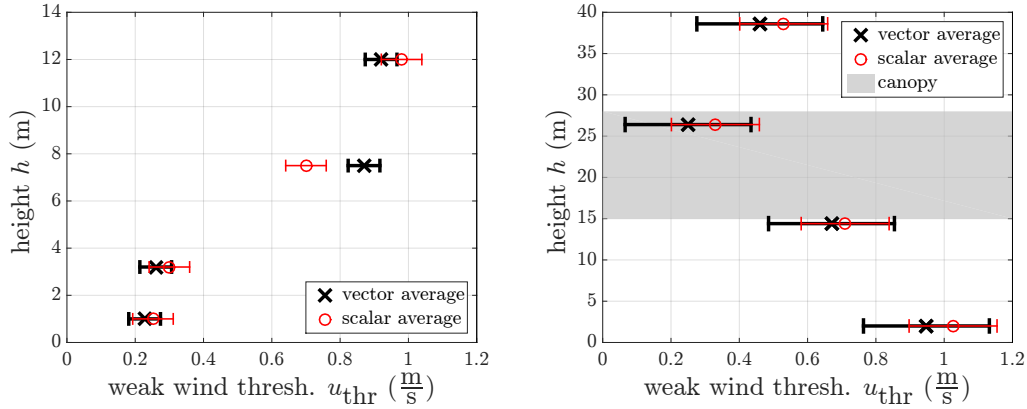
Figure 4.6: Relation between sensor height and threshold velocity of the weak-wind regime for the vector averaged (black crosses) and the scalar averaged (red circles) case. The left plot contains the results from the BPP site (grassland) while the right plot shows the one from the MF site (dense forest). In the right plot, the approximate extent of the canopy is marked grey.

ground network. All the other heights correspond to the threshold gotten from the hockey stick fit of only one sensor because there is only one sensor at each respective height except for the ground network. We assume that the uncertainty estimated from the data of the ground networks is valid also for the other heights.

The plot for the BPP site confirms the finding from Sun *et al.* (2012), that a greater height leads to a higher threshold wind speed of the weak-wind regime. The logarithmic relationship that they found can however not be verified at the BPP site. This might be due to the small number of sensors used for the profile and the large scatter.

Neither at the MF site nor at any of the other forested sites, the general trend of a higher weak-wind threshold with greater height can be seen. Instead, for MF, the weak-wind threshold calculated from the ground network is higher than that of all the three sensors at the tower. Within the dense canopy (marked in grey in fig. 4.6), the transition point is shifted to lower wind speeds and rises again above the canopy. Also at the MP site (not shown), the transition wind speed calculated by the scalar average only starts to rise above the canopy. For the vector average at the MP site, no reliable statement can be made because for the station at the top of the canopy the fit for determining the threshold didn't work. However, the vector averaged transition wind velocity of the B1 sensor (height $h_{B1} = 30.65$ m) is similar to that of the scalar average. Thus we can assume that also here, a similar increase of the transition wind speed happens above the canopy. Also at the HJA site, the sensor A2 ($h_{A2} = 15.8$ m) which is situated within the canopy shows a lower transition wind speed than the surrounding stations of the ground network (A1 and A3). The threshold at the sensor above the canopy (WS1_Top) is $u_{thr} = 0.75 \frac{m}{s}$ and thus again higher than the one within the canopy

In summary the canopy restricts the tendency of a higher weak-wind threshold at greater heights. Above the canopy, this tendency seems to hold again.

Next, we compare our results of the BPP site to the one of Mahrt & Thomas (2016) who used the data from the C3 sensor at the BPP site. For this sensor, they determined the threshold wind velocity for the weak-wind regime using the vector average. However, they used only night data and a much shorter perturbation time scale of $T_\mathrm{p} = 6$ s. For identifying the threshold they did not use a fit but roughly estimated it from the bin averages. That way they identified the transition point for the C3 sensor at $u_\mathrm{mahrt} = 0.3 \frac{\mathrm{m}}{\mathrm{s}}$. This is very similar to the threshold wind speed we get for the C3 sensor using the scalar average, namely $u_\mathrm{thr} = 0.33 \frac{\mathrm{m}}{\mathrm{s}}$. For the vector average unfortunately the fit didn't work at the BPP C3 station. Because of the similarity between vector averaged and scalar averaged threshold however we can assume that also with vector averaging the threshold would be around $u_\mathrm{thr} \approx 0.3 \frac{\mathrm{m}}{\mathrm{s}}$. The result from the C3 sensor thus suggests that neither including the data from the day nor increasing the averaging time scale have an impact on the weak-wind threshold from the hockey stick curve. In the scope of this master thesis however no tests where conducted for proving or disproving that impression with other sensors than the C3 sensor at BPP.

When comparing the thresholds of the ground networks between the different sites
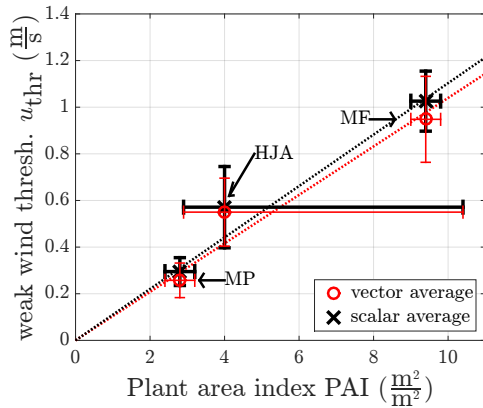
Figure 4.7: Relation between the Plant area index PAI and the mean transition wind speed at the ground network. The dotted lines are the respective fits of eq. 4.6 to the vector and scalar averaged data.

from table 4.1 it seems that a denser forest is connected to a higher weak-wind threshold. For testing that impression, we first plot the relationship between the plant area index PAI (area of plants per area of ground) and the weak-wind threshold calculated by averaging over all the the ground network stations of each respective site (fig. 4.7). For the PAI data has to be taken from literature (see chap. 2). Unfortunately we don't have data on the plant area index of the BPP site, and thus can not include it into the plot. At the HJA, the canopy density is very variable and ranges from $2.9 \frac{\mathrm{m}^2}{\mathrm{m}^2}$ to $10.4 \frac{\mathrm{m}^2}{\mathrm{m}^2}$. This is indicated by the errorbar covering this range of plant area indices. For the two other sites, the errorbar represents the range of plant area indices found in literature which is probably due to different dates of measurement. The errorbar in the weak-wind threshold is estimated by the standard deviation of

the ground network thresholds.

In addition to the data points, the plot includes the fit of the function

$$u_{\mathrm{thr}} = a \cdot \mathrm{PAI} \tag{4.6}$$

to the data. For the vector averaged case, the resulting parameter is $a_{\mathrm{v}} = (0.10 \pm 0.01) \frac{\mathrm{m}}{\mathrm{s}}$ and for the scalar averaged case $a_{\mathrm{v}} = (0.11 \pm 0.01) \frac{\mathrm{m}}{\mathrm{s}}$. The indicated error is the asymptotic standard error of the fit. When trying to add a constant so that $u_{\mathrm{thr}} = a \cdot \mathrm{PAI} + b$, the resultant b is small compared to its error. Thus the version without b is used. This equation shall however not imply any knowledge of the physical processes determining the threshold velocity.

Despite the large uncertainty and the small number of data, the plot (fig. 4.7) reflects the tendency that a denser vegetation leads to a higher weak-wind threshold.

Still we would like also to include the BPP site. For this reason, the plant area index will now be replaced by the roughness length z_0. This can calculate for all the sites including BPP. Without large obstacles, the roughness length is given by the height above ground, at which the mean wind speed becomes zero assuming a logarithmic wind profile. For neutral stability, it can be calculated from the friction velocity u_* and the mean wind speed $\bar{u}$ at height z using the logarithmic wind profile. It is

$$z_0 = z \exp\left(-\frac{\kappa \bar{u}}{u_*}\right) \tag{4.7}$$

with the Kármán's constant $\kappa = 0.41$. With trees (or buildings) it is necessary to take into account the displacement height d. This is the height by which the wind profile is shifted upward because of the large obstacles. The displacement height then becomes the effective ground level (Foken & Napo, 2008). Eq. (4.7) then becomes

$$z_0 = (z - d) \cdot \exp\left(-\frac{\kappa \bar{u}}{u_*}\right) \tag{4.8}$$

The displacement height can be approximated by $d \approx \frac{2}{3} h_{\mathrm{c}}$ where h_{c} is the canopy height. At heights lower than the displacement height, the logarithmic wind profile is not valid. This means, that it is only possible to calculate the roughness length from sensors higher than the displacement height. This condition is fulfilled when taking data from the highest sensor of every site. Thus, for computing the roughness length we use A1 at $h_{\mathrm{A1}} = 12$ m for the BPP main site, B3 at $h_{\mathrm{B3}} = 6$ m at the BPP Moritz site, B1 at $h_{\mathrm{B3}} = 30.65$ m at the MP site, WS1_Top at $h_{\mathrm{WS1\_Top}} = 38$ m at the HJA site and B1 at $h_{\mathrm{B3}} = 38.6$ m at the MF site .

Furthermore, the logarithmic wind profile of eq. (4.7) and (4.8) is only valid in neutral stability. Thus we first have to identify when this was the case and only use those intervals. For determining the stability, the Bulk Richardson number is used

$$R_{\mathrm{B}} = \frac{g}{\theta_{\mathrm{s}}} \cdot \frac{\Delta\theta_{\mathrm{s}} \cdot \Delta z}{(\Delta u_{\mathrm{NS}})^2 + (\Delta v_{\mathrm{NS}})^2} \tag{4.9}$$

with the gravity acceleration g. For calculating R_B, two sonic anemometers one above the other are necessary. This condition is fulfilled each of the sites. Then, Δz is the height difference between those two sensors. Δu_{NS} and Δv_{NS} are the differences between the two sensor's velocity components u_{NS} and v_{NS} respectively. The index NS at the velocity components indicates that it is impossible to take the velocity components from the coordinate system of the mean wind direction. one needs to choose the fixed coordinate frame of the earth instead, in order to make sure that for both sensors the same coordinate system is applied. u_{NS} is oriented along the east-west direction and v_{NS} along the north-south direction. Finally, θ_s is the sonic potential temperature

$$\theta_s = T_s \left(\frac{p_0}{p} \right)^{\frac{R}{c_p}} \tag{4.10}$$

with the gas constant of air R, the specific heat capacity at constant pressure c_p and the sonic temperature T_s(see chap.2.2).

The Bulk Richardson number corresponds to the ratio of buoyancy to shear flow and is a measure of the dynamic stability of a flow. This means that apart from the static stability given by the temperature gradient it also takes into account the wind shear. Thus, R_B is a measure of how much turbulence is generated by the flow. We consider the dynamic stability as neutral when

$$-0.0625 < R_B < 0.125 \tag{4.11}$$

according to Skeib (1980) and Foken (1991). When this condition is met, the roughness length z_0 can be calculated by eq. 4.8. For calculating the roughness length, it is necessary to choose a longer perturbation time scale T_p so that also the transport of momentum at larger time scales is included. Furthermore, with the larger time scales, turbulence is better in equilibrium with the mean flow (Mahrt & Thomas, 2016). For this purpose, we choose $T_p = 30$ min.

We can now compute the roughness length z_0 for every neutrally stable interval. The result of this calculation for the A1 sensor at the BPP main site can be seen in
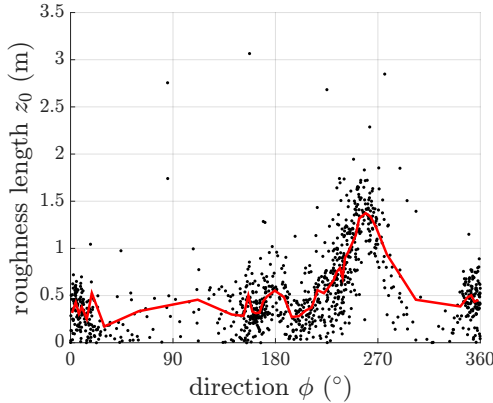
Figure 4.8: Roughness length at the BPP main site. The black dots are the results from the single, neutrally stable 30 min-intervals in dependence of the respective wind direction direction. The red line is the connecting line between the bin averages and serves as a guide to the eye. Each bin contains the same number of data points and 15 bins are distributed over the full range of $360°$.

figure 4.8. The results for the roughness length of the single intervals (black dots)

are depicted in dependence of their respective wind direction. Thus the directional dependence of the roughness length becomes evident. The maximum roughness length can be found at a westerly wind direction (270°). This corresponds to the direction of a field with small trees (see fig. 2.2).

For all the sites, an average roughness length is computed. The site-specific mean
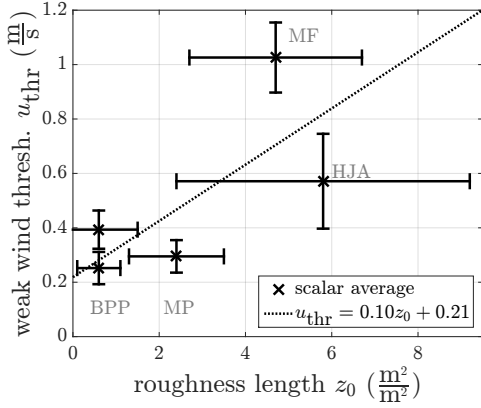
Figure 4.9: Relationship between the mean threshold wind speed of the ground network and the roughness length of the respective site. For the BPP site there is a clear difference in the transition wind speed between the main and the Moritz site so both are depicted. The Moritz site corresponds to the higher threshold. The dotted line is a fit of a linear function to the data.

threshold wind speed for each site is then plotted in dependence of it's roughness length (fig. 4.9). The uncertainties of the roughness length and the weak-wind threshold are estimated by the standard deviation of the roughness length and of the different thresholds of the ground network within one site respectively.

The large variability of the roughness length partially result from it's directional dependence (see fig. 4.8). If only one direction is considered, there is actually less uncertainty in the roughness length. The errorbars thus reflect the variability of the terrain. This is actually desirable since the sensors of the ground network are spread over the site and thus cover variable terrain. As there is only one sensor at the top of the canopy for each site for calculating the roughness length it is good that the variability of the terrain is represented by the uncertainty of the roughness length. The largest variability of the roughness length can be found for the HJA site, which also has the most variable terrain.

As with the plant area index, a trend of higher transition wind speeds with higher roughness length can be seen. The result from the fit of a linear function

$$u_{\mathrm{thr}} = a_{\mathrm{s}} \cdot z_0 + b_{\mathrm{s}} \tag{4.12}$$

to the data supports that impression (see dotted line in fig. 4.9) with $a_{\mathrm{s}} = (0.10 \pm 0.06) \, \frac{1}{\mathrm{s}}$ and $b_{\mathrm{s}} = (0.21 \pm 0.09) \, \frac{\mathrm{m}}{\mathrm{s}}$. Still, also when taking the roughness length instead of the plant area index as a proxy for the obstacle density, we cannot get a clearer result than this rough tendency due to the small number of data and the large uncertainty of the roughness length, especially that of the HJA site.

As the results when taking the vector average are very similar to that of the scalar average, they are not included in the plot of the relationship between the roughness length and the threshold of the low wind regime. The resultant fitparameters of

the linear function when using the threshold from the vector averaged version are
$a_{\mathrm{v}} = (0.09 \pm 0.06)\ \frac{1}{\mathrm{s}}$ and $b_{\mathrm{v}} = (0.19 \pm 0.08)\ \frac{\mathrm{m}}{\mathrm{s}}$.
All in all we could show that the location of a sensor regarding both, the terrain and the sensor height have a great influence on the weak-wind threshold. However it became apparent that finding a parameter that describes the relationship between the terrain and the weak-wind threshold is not an easy task.

4.3 Is the weak-wind regime connected to decoupling?

We now want to test if weak-wind intervals correspond to a decoupling of the subcanopy air from the air above the canopy. This would explain why a denser canopy leads to a higher threshold velocity. With a dense barrier impeding the vertical exchange it would need higher wind speeds for a coupling of the subcanopy to the air above.
For the purpose of testing whether or not the subcanopy is decoupled, the dependence of the turbulence below the canopy to the one above will be used. We use the standard deviation σ_w of the vertical velocity component as an indicator of the turbulence strength. Numerous works exist (Thomas *et al.* 2013; Oliveira *et al.* 2013) where the authors state that for a coupled canopy, if the turbulence above the canopy increases, the turbulence in the subcanopy is expected to increase as well. Vice versa they conclude that, if the turbulence in the subcanopy does not increase with stronger turbulence above the canopy, the two levels are likely to be decoupled from each other. Consequently, for differentiating between a coupled and a decoupled canopy regime they use a similar method as we did for identifying the weak-wind regime. The point where the dependence between the two standard deviations changes is used as transition point between coupled and decoupled regime.

We now test if the weak-wind cases correspond to a decoupled subcanopy. For this
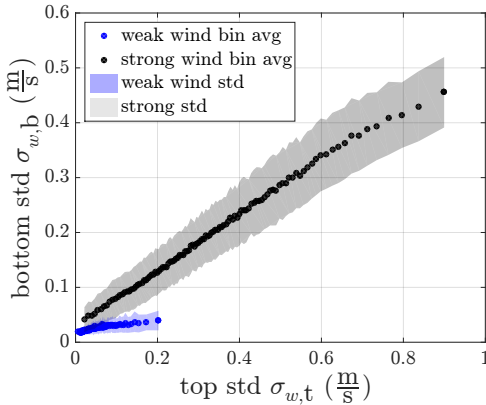
Figure 4.10: Relationship between the standard deviation of the vertical wind component of the ground network sensors $\sigma_{w,\mathrm{b}}$ and the sensor above the canopy $\sigma_{w,\mathrm{t}}$ for weak-wind (blue) and strong-wind cases (black) at the BPP site.

purpose, we need to check if there is a different relationship between the standard deviation of the vertical wind component above the canopy $\sigma_{w,\mathrm{t}}$ and the one in the subcanopy $\sigma_{w,\mathrm{b}}$ for weak-wind cases than there is for strong-wind cases. According to the method described above, we expect a smaller slope of $\sigma_{w,\mathrm{b}}(\sigma_{w,\mathrm{t}})$ for the weak-wind

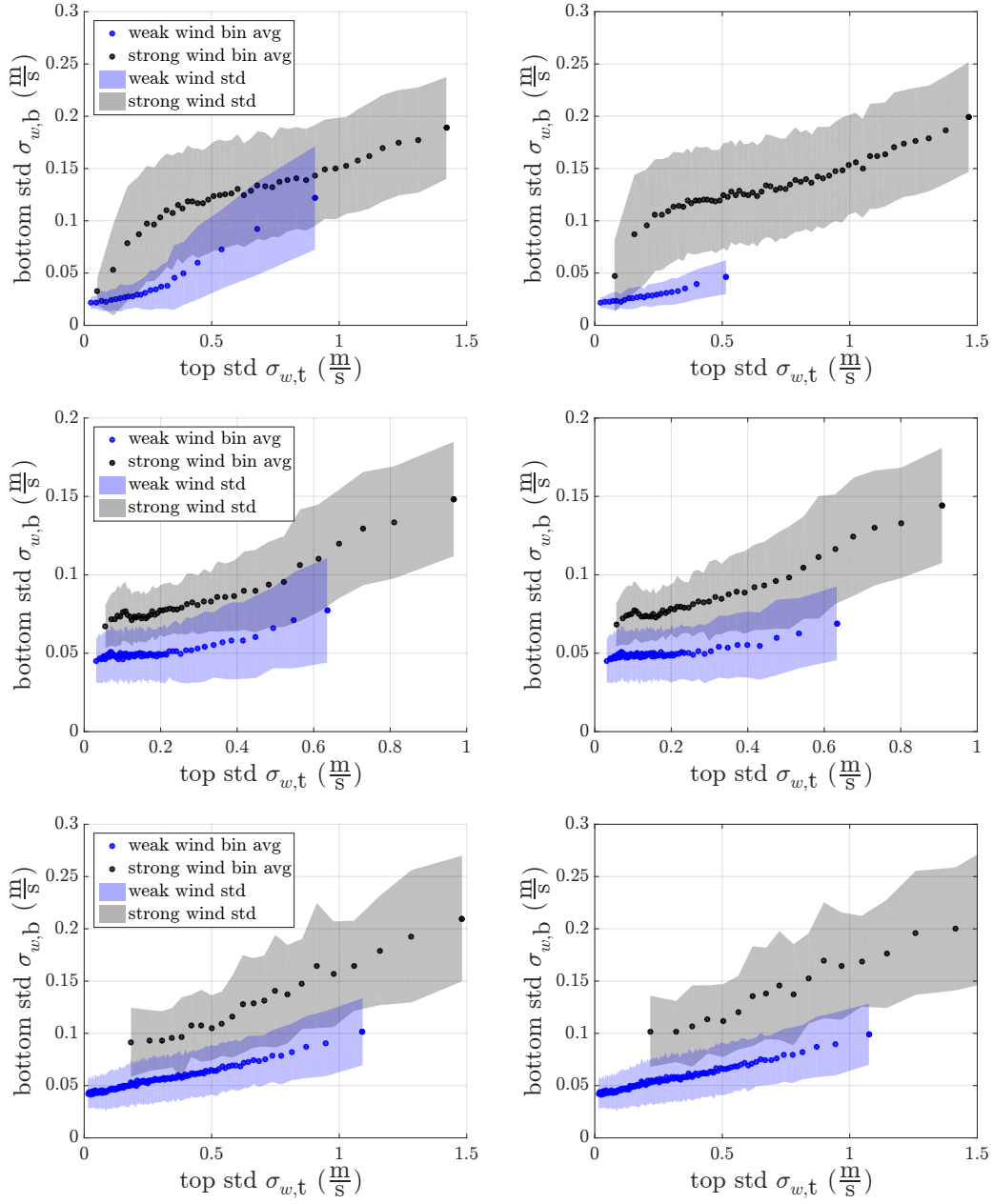Figure 4.11: Relationship between the standard deviation of the vertical wind component below $\sigma_{w,\mathrm{b}}$ and above the canopy $\sigma_{w,\mathrm{t}}$ for the forested sites. Top row corresponds to MP, middle row to HJA and lowest row to the MF site. In the left column, the weak-wind regime was determined from vector averaged wind velocities, in the right column from scalar averaged ones.

than for the strong-wind case, if weak wind corresponds to a decoupled subcanopy layer.

At the MP site and the MF site, data is taken from the B1 sensor and at HJA from WS1Top as the above canopy data. At the BPP site there naturally is no 'above canopy sensor', as there is no continuous canopy at this site. As a substitute, we use the A1 sensor, which is the highest sensor at this site. For the subcanopy data we would ideally like to take a sensor of the ground network fixed on the same tower as the above canopy sensor. This is however not possible because at most of the sites no ground network sensor is located at the main tower. As a substitute, we use the average from the two ground network sensors closest to the tower. The sensors used for this purpose are the A3 and A4 sensor at BPP, C1 and C4 at MP, A1 and A3 at HJA and B3 and C3 at MF. From the respective two sensors of each site, the mean of the vertical wind standard deviations for every interval is calculated.

For deciding whether or not there is a weak-wind situation, each of the two ground network sensors is taken into account individually. Only when both sensors indicate wind speeds below the weak-wind threshold of the respective site, an interval is classified as a weak-wind situation. Similarly, a strong wind situation is, when both sensors indicate a wind speed larger than the site-specific weak-wind threshold (see chap. 4.1). Intervals, that are classified differently by the two ground network sensors are excluded from the following analysis.

For looking at the dependence between $\sigma_{w,b}$ and $\sigma_{w,t}$, again bin averages are calculated (fig. 4.10 and fig. 4.11). This is done separately for the weak-wind and the strong-wind cases. Contrary to the previously calculated bin averages, this time the bins don't have fixed edges, but each bin contains the same number of points. Thus, one can directly see, if in a certain region of vertical wind standard deviations there are particularly many weak-wind or strong-wind data points. Each of the bins contains 500 data points, except for the weak-wind bins at the BPP site and the strong wind bins at the MF site. Here, one bin only corresponds to 100 data points due to the small overall number of observations. Additionally, figure 4.10 and figure 4.11 also show the standard deviations within the bins as a light blue or grey background, respectively.

Figure 4.10 shows that at the BPP site, there actually is a very different dependence of the ground network's vertical wind standard deviation on the one of the top sensor (A1), depending on whether there is a weak-wind or a strong-wind situation. The difference between the weak-wind and the strong-wind regime is so distinct that even the areas of the standard deviation hardly overlap. In figure 4.10, distinction between regimes was done using the scalar averaged threshold. The plot however looks the same, if the vector average is used instead.

One can see that weak-wind cases rarely exist with a top sensor standard deviation higher than $\sigma_{w,t} \gtrsim 0.2\,\frac{\mathrm{m}}{\mathrm{s}}$. For lower $\sigma_{w,t} \lesssim 0.2$ at the top, the turbulence at the ground network is generally weak in weak-wind situations compared to during strong-wind situations. For the same amount of turbulence at the top sensor, the turbulence at the bottom sensor is generally weaker in weak-wind situations. Furthermore, during weak-wind situations, the vertical wind standard deviation at the ground network

is almost independent of the one at the top sensor. In contrast, during strong wind cases, a higher standard deviation $\sigma_{w,\text{t}}$ at the top sensor leads to a higher standard deviation $\sigma_{w,\text{b}}$ at the bottom sensor. According to the method from Thomas *et al.* (2013) etc., we can thus conclude that at the BPP site, during weak-wind cases, the air layer at the ground network ($h = 1$ m) is decoupled from the layer at the A1 sensor ($h_{\text{A1}} = 12$ m).

Figure 4.10 shows the same plot for all the forested sites. At the forested sites, there is a slightly different picture than at the unforested BPP site. First of all, at the forested sites, there are also weak-wind situations with a higher top sensor standard deviation than at BPP $\sigma_{w,\text{t}} \gtrsim 0.2 \; \frac{\text{m}}{\text{s}}$. This difference is due to the canopy acting as a momentum sink, so that despite high turbulence and high wind speeds above the canopy only little momentum actually persists at the ground network sensors within the subcanopy. Thus, weak-wind situations can actually exist within the canopy despite relatively high wind speeds above. At the grassland site, to have a weak-wind situation at the ground network, there must also be relatively weak wind at the highest sensor because there is no momentum sink between those two. Still, as expected, the highest top sensor vertical wind standard deviations can be found during strong-wind situations.

The main difference however is that at the forested sites, there is no different slope in the dependence of $\sigma_{w,\text{b}}$ on $\sigma_{w,\text{t}}$ during weak-wind situations than during strong-wind situations. Especially at the HJA and the MF sites (middle and bottom row, fig. 4.10), the dependence of the turbulence within the canopy from that above the canopy during weak-wind situations appears to be identical to the one during strong-wind situations except for a constant offset. This observation is insensitive to the choice of averaging method (vector or scalar average). Consequently, at those sites we can not conclude that a weak-wind situation corresponds to a decoupled canopy.

Nevertheless, the amount of turbulence in the subcanopy at a certain above canopy turbulence is much smaller during weak-wind situations than during strong wind situations. The shaded areas, which indicate the typical amounts of subcanopy turbulence at a given above canopy turbulence hardly even overlap. We can thus conclude that during weak-wind situations, the canopy does act more efficiently as a momentum sink than during strong-wind situations. However, an increase in the above canopy turbulence leads to an increase of the subcanopy turbulence, which is not the behaviour expected for a decoupled subcanopy.

The only forested site with at least small differences in the dependence of $\sigma_{w,\text{b}}$ on $\sigma_{w,\text{t}}$ between weak-wind and strong-wind situations is the MP site. If the classification into weak-wind and strong-wind regime is done with the scalar averaged threshold velocity, only the strong wind data with a very small standard deviation $\sigma_{w,\text{t}}$ above canopy show a different trend. Here, a strong slope can be observed during the first two to three strong-wind bins. Then the slope levels off immediately to the same slope that can be observed in the weak-wind case. As every bin corresponds to the same number of individual data points, it is evident that this different behaviour is only the case for a very small portion of the overall data. To summarize, during a strong wind situation, the turbulence strength within the canopy seems to be much more

influenced by the turbulence above the canopy when the turbulence strength above is weak than when it is strong. One possible reason for that would be that the subcanopy
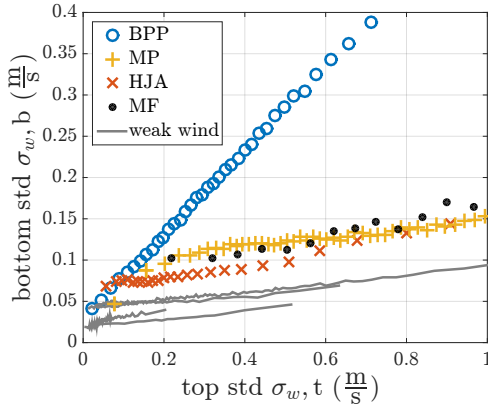

Figure 4.12: Comparison of the different site's dependency of the subcanopy turbulence on the above canopy turbulence during strong-wind situations (coloured symbols). In contrast, the different site's dependencies during weak-wind situations are added in grey.

is actually decoupled from the above-canopy during weak-wind situations and coupled during strong-wind situations, but the canopy prevents that vertical motions in the subcanopy can grow above a certain limit. Thus, once the turbulence has reached a certain threshold, the canopy hinders its further growth. This hypothesis is supported by the fact that also at the HJA site, the bin averages of the vertical wind's standard deviation bend down a bit at very small turbulence intensities at the top $\sigma_{w,t} < 0.1 \frac{m}{s}$ (see fig. 4.11 and fig. 4.12). It could thus be that also at the HJA site, the subcanopy turbulence strongly grows with increasing above canopy turbulence for $\sigma_{w,t} < 0.1 \frac{m}{s}$ and then levels off and that there is just not enough data in the weak turbulence sector to properly see this behaviour. It is remarkable that the transition in slope of the strong-wind subcanopy turbulence occurs at approximately the same amount of subcanopy turbulence at the HJA site as at the MP site. This is also coincident to the amount of subcanopy turbulence that can be found during the few strong-wind situations at the MF site (see fig. 4.12). Furthermore, the slope at the strongly rising section of the MP site's strong-wind cases resembles the slope of the strong-wind case at BPP (see blue circles and yellow crosses for $\sigma_{w,t} < 0.2 \frac{m}{s}$ in fig. 4.12).

All this could indicate that also at the forested sites, the subcanopy air is actually decoupled from the above canopy during weak-wind situations and coupled during strong-wind situations, but the canopy prevents the vertical wind's standard deviations from growing beyond a certain limit. This is however only a guess and can not be proven. Furthermore Vickers & Thomas (2014) showed that a canopy does actually not strongly restrict vertical motions but rather the horizontal ones. This contradicts the hypothesis of the canopy setting an upper limits for the vertical velocity's standard deviation. A detailed analysis of the different terms in the budget of the turbulent kinetic energy could help in understanding whether or not the different behaviours of $\sigma_{w,b}(\sigma_{w,t})$ in the strong-wind and the weak-wind regime indicate decoupling.

If the classification between weak and strong wind is done with the vector averaged threshold, the MP site has one more feature that distinguishes it from the other

forested sites. This feature is that during weak-wind situations at relatively strong above-canopy turbulence ($\sigma_{w,\mathrm{t}} \gtrsim 0.4\ \frac{\mathrm{m}}{\mathrm{s}}$), the subcanopy turbulence suddenly shows a much steeper slope (fig. 4.11 left column, top row). This is not the case if the classification is done with the scalar averaged wind speed.

The MP site is the site with the highest percentage of data points that is classified
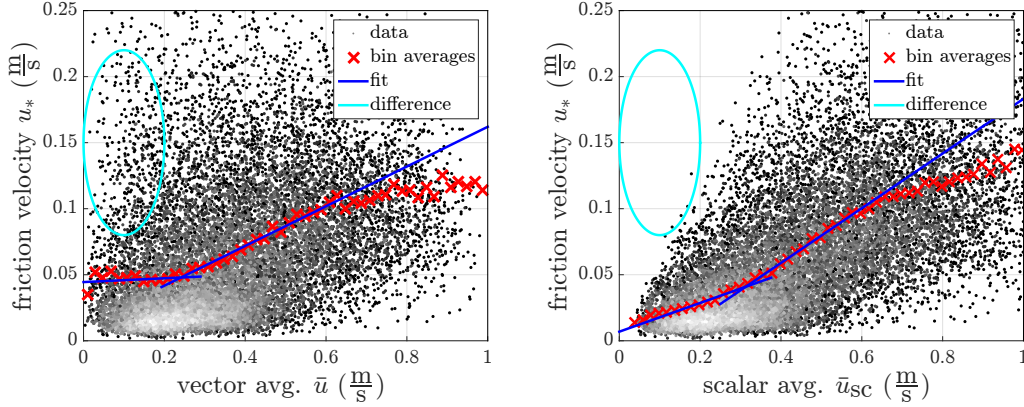
Figure 4.13: Points allocated differently to weak-wind or strong-wind depending on the averaging scheme used for the wind speed.

differently depending on whether the scalar or the vector averaged wind speed is used for determining the regimes. As a result, is not surprising that MP is the only site where there is a difference depending on which threshold is used for the classification. In figure 4.13 there are again the hockey stick plots used for the determination of the weak-wind regime at the MP site. This time however, the points that led to the big difference between classification by vector or by scalar average are marked by a turquoise ellipse. Apparently, at the MP site, there are some data points with a very small velocity of the mean flow but a considerable amount of turbulence. Due to the small velocity of the mean flow, with the vector average they are classified as weak-wind data. The considerable amount of turbulence however leads to a significant mean wind speed if the scalar average is used, as there is a significant amount of momentum contained in the flow. Thus, those points are allocated to the strong-wind regime when using the scalar average.

These points are very likely the ones that cause the larger slope for $\sigma_{w,\mathrm{t}} \gtrsim 0.4\ \frac{\mathrm{m}}{\mathrm{s}}$ in the vector averaged case at the MP site (fig. 4.11 top row). With those points being attributed to the strong-wind class in the scalar averaged case, the increase in slope can not be seen. As they are the data points with the highest above canopy turbulence of all the MP site's weak-wind data, we can conclude that the additional turbulence that causes the increased slope of $\sigma_{w,\mathrm{b}}$ likely is induced from above the canopy.

This coherence is actually an argument for using the scalar averaged wind speed for determining the weak-wind regime. The aim in separating the data of weak-wind situations from the rest is finding the situations in which there is more turbulence

than expected. Then, turbulence might have been generated by submeso motions. This however is probably not the case if the turbulence actually originates from over the canopy.

To summarize, it could not be confirmed that a weak-wind situation in the subcanopy is synonymous with decoupling of the subcanopy from the above canopy air. The only site where the dependence of the subcanopy turbulence from the above canopy turbulence acknowledges a decoupling is the BPP site, the only site where there is actually no physical barrier between the bottom and the top sensor. Nevertheless, for all of the sites, the weak-wind and the strong-wind data are surprisingly well separated in the plots of the vertical wind standard deviations $\sigma_{w,b}(\sigma_{w,t})$. The typical ranges of the strong-wind data and the weak-wind data hardly overlap. On the other hand, the typical ranges of the weak-wind data are very similar between all of the sites (see grey lines in fig. 4.12) and also the typical ranges of the strong-wind data at all forested sites (coloured symbols in fig. 4.12).

We did not find any evidence that during strong wind, turbulence in the subcanopy
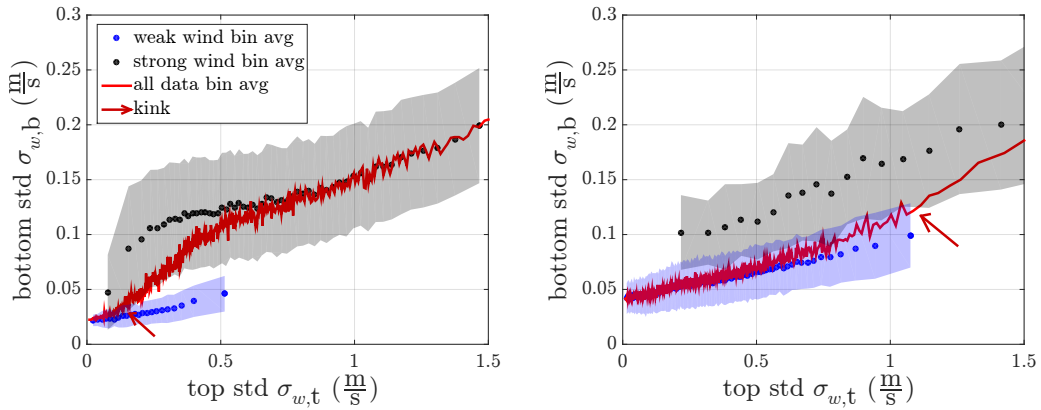
Figure 4.14: Dependency of the subcanopy turbulence on the above canopy turbulence in weak-wind and in strong-wind situations (blue and black points) versus overall dependence when no separation into weak and strong-wind regime is done (red line). Left plot belongs to the MP site, right plot to the MF site.

is more dependent on turbulence above canopy than during weak wind. In the case of strong-wind and weak-wind data being separated, there isn't even a critical above canopy turbulence, starting from which the subcanopy turbulence is more strongly influenced by the above canopy one. For this reason it is necessary to check, if a critical above canopy turbulence exists, in case that no separation between weak-wind and strong-wind is done. For this purpose, we look at the dependence of the subcanopy $\sigma_{w,b}$ from the above canopy $\sigma_{w,t}$ without separating weak and strong-wind data and compare it to the behaviour of the separated weak-wind and strong-wind curves.

Figure 4.14 shows again the black and blue dots representing the bin averages of the strong-wind and weak-wind case's dependence of $\sigma_{w,b}$ on $\sigma_{w,t}$ (left plot for MP, right plot for MF). As before, the standard deviation within the bins is represented by

grey and blue backgrounds. This time however, the plots show an additional red line, which is the connecting line between the bin averages when no separation into weak-wind and strong-wind data is done. In this line there actually is a point where the slope of $\sigma_{w,\mathrm{b}}(\sigma_{w,\mathrm{t}})$ suddenly increases (marked with a red arrow). Comparing the position of the transition point to the separated bin averages, one can see that this corresponds to the strong-wind situations becoming more frequent than the weak-wind situations at the given level of above canopy turbulence $\sigma_{w,\mathrm{t}}$. The higher slope of the combined weak and strong-wind bin averages that follows at higher above canopy turbulence than the kink value actually results from the focus of the combined data slowly shifting from the weak-wind position to the strong-wind position. Once the line of the combined data's $\sigma_{w,\mathrm{b}}(\sigma_{w,\mathrm{t}})$ reaches that of the strong-wind data, the slope reduces again to its original value (see left plot of fig. 4.14, MP site). It seems thus as if the bend in the dependence of the subcanopy $\sigma_{w,\mathrm{b}}$ on the above canopy $\sigma_{w,\mathrm{t}}$ was just caused by the strong-wind data gaining more influence than the weak-wind data. This should be further investigated in order to decide whether or not the kink in the relation between $\sigma_{w,\mathrm{b}}$ and $\sigma_{w,\mathrm{t}}$ can actually be used as an indicator on whether or not the subcanopy is decoupled from the above canopy.

5 Meandering - a typical weak-wind phenomenon

We now want to analyse meandering, one of the typical submesoscale phenomena. Meandering generally refers to a horizontal, low frequency oscillation of the wind direction. It is prevalent during weak-wind conditions, but can also be observed during strong-wind situations (Anfossi *et al.*, 2005). Also sudden wind shifts instead of wind direction oscillations are sometimes referred to as meandering (Mahrt, 2007). In the following section, a new technique for identifying meandering intervals is introduced, using the constancy of the wind C. Afterwards, this technique is compared to one that has been used a lot in the recent years. This technique makes use of the autocorrelation of the horizontal wind directions and the temperature, respectively (Anfossi *et al.*, 2005). Finally, we will look if there are any predominant time scales inherent to the meandering motions and if any differences in the meandering can be found between day and night-time or between weak-wind and strong-wind situations. For extracting the time scales, again two different methods are compared. Those methods are the autocorrelation function on the one hand and the wavelet transform on the other hand (Cava *et al.*, 2017).

5.1 Constancy as a meandering indicator

For determining during which intervals meandering took place, a dimensionless quantity called constancy C is used. This quantity makes use of the difference between the vector average and the scalar average. It is calculated as

$$C = \frac{\bar{u}}{\bar{u}_{\mathrm{sc}}} \tag{5.1}$$

where again $\bar{u}$ means the vector averaged wind velocity and $\bar{u}_{\mathrm{sc}}$ refers to the scalar averaged wind speed (Singer 1967; Mahrt 2007). When the direction of the wind stays constant during the complete interval over which the wind speed is averaged, the constancy will reach its maximum $C = 1$. On the other hand, if the wind speeds and directions are distributed symmetrically during the averaging interval, the constancy reaches its minimum $C = 0$. Thus, the constancy is a measure of the variability of the wind direction during the averaging interval.

Figure 5.1 shows time series of a 6-hour interval at the MF site (sensor C3), during which 2 separate periods of meandering can be observed. The meandering periods approximately last from 0:20 AM to 02:00 AM and from 3:40 AM to 05:10 AM.

Figure 5.1: Time series of the wind ϕ (top), the two horizontal wind components u_{NS} and v_{NS} (middle)and the constancy C (bottom) during a 6-hour interval that contains two separate meandering periods.

The time series of the wind direction (top plot in fig. 5.1) is output from the Bmmflux software with a perturbation time scale $T_p = 1$ min (see chap. 3.2). Whereas during non-meandering periods, the wind direction varies only sightly, it spans the full range of 360° during meandering periods. It is thus evident, that the 'mean wind direction' has no physical meaning during meandering (Mortarini *et al.*, 2013).

The plot in the middle shows the time series of the two vector averaged velocity components u_{NS} and v_{NS} output by the Bmmflux software ($T_p = 1$ min). The index NS indicates that the velocity components now are regarded in the coordinate frame of the earth's surface and not in the one of the mean wind direction, which changes

its orientation every interval. This is necessary for making the shifts in wind direction visible in the velocity components. Also the vertical wind component will get the index NS and thus be called w_{NS} when the coordinate frame referred to is the fixed one of the earth's surface. During the meandering periods, both horizontal velocity components switch their sign regularly due to the directional changes. During the non-meandering periods, the relative changes of the horizontal wind components are much smaller.

Since the aim is to find submesoscale phenomena, it is necessary to make sure that only the 'slow' directional changes are identified and not the rapid ones caused by the small-scale turbulent eddies. For this purpose, we do not take the 20 Hz data for calculating the constancy, but the vector averaged mean wind velocities u_{NS} and v_{NS}. This way, any directional changes that can be detected take at least longer than one minute. From the time series of u_{NS} and v_{NS}, the vector as well as the scalar average and from those the constancy are calculated with a moving average of length τ.

Of course, the window length τ for computing the constancy has an influence on what is identified as meandering and thus has to be chosen carefully. It is evident, that a too short filter may prevent the constancy from detecting some directional changes. If a directional change takes much longer than the filter length, the constancy is not able to see its full extent. Thus, a quick one-time directional change may be detected while a slow but long-lasting directional change may be missed.

On the other hand, also a too long averaging window may lead to problems, as for example:

- The ends of the meandering intervals get smeared out

- Very slow directional changes that might e.g. be connected to the diurnal cycle might be mistaken as meandering

- Regular directional changes from a well-defined main wind direction (see chap. 5.4, fig. 5.13) cannot be seen if the filter length is much longer than the switch of direction takes.

It is thus clear, that an intermediate length has to be chosen for the averaging window. The chosen filter length should be suitable for detecting directional changes at time scales typical for meandering.

Mortarini *et al.* (2016a) investigated the time scales of meandering motions at two different sites. The found that the average time scale is site-dependent. Within an urban environment in Turin, they found an median meandering time scale of $\tau_m \approx 25$ min and a median time scale $\tau_m \approx 36$ min at a pasture near the Amazon river. Within one site, the meandering time scales they found varied substantially from a few minutes up to nearly an hour. Those time scales should be kept in mind when choosing the filter length for calculating the constancy.

For selecting the optimal filter length, we look at the number of minutes N_Δ, that is classified differently as meandering or non-meandering when the length of the averaging window τ for computing the constancy is increased by one minute. In Figure 5.2, this can be seen for the A2 sensor at the BPP site. The dependence of the number of changes on the filter length can be well described by an exponential
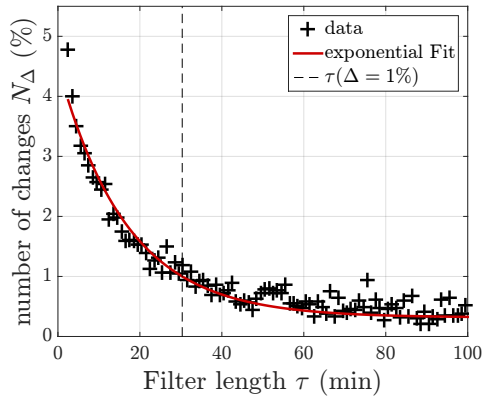
Figure 5.2: Crosses: Number of minutes that are classified differently as meandering or non-meandering when the filter length is extended by one minute. Red line: Fit of an exponential function to this data. Vertical dashed line: Marks the filter length at which the number of changes drops below 1%

Site	$\tau_{1\%}$ (min)	$\sigma_{\tau_{1\%}}$ (min)
BPP Main	29	2
BPP Moritz	40	4
MP	37	4
HJA	26	10
MF	42	2

Table 5.1: Mean site-specific optimal filter lengths determined by the dependence of the Number of minutes classified differently when increasing the filter length on the filter length and its standard deviation.

function

$$N_\Delta = N_0 \cdot \exp\left(\frac{\tau}{\tau_0}\right) \qquad (5.2)$$

For calculating the constancy, we use the filter length $\tau_{1\%}$, where on average, the number of changes N_Δ drops below 1%. Depending on site and sensor, the $\tau_{1\%}$ varies a bit. Thus, the fit of eq. (5.2) is done for every station of the ground network. From those values, a mean resultant filter length is calculated for every site.

Table 5.1 contains the filter lengths $\tau_{1\%}$ for the different sites and its standard deviation $\sigma_{\tau_{1\%}}$. The standard deviation, which indicates the variability of the single sensor's $\tau_{1\%}$, is much larger at the HJA site than at all the other sites. Furthermore, the site-specific filter lengths of the two BPP sub-sites (BPP Main and BPP Moritz) are very different compared to their respective standard deviations. The standard deviations of the BPP sub-sites and also the MP and MF site are comparatively small.

The reason for the high standard deviation $\sigma_{\tau_{1\%}}$ at the HJA site is probably the comparatively large distance between the sensors. While the distances between the sensors at the MF and MP site are less than 100 m, the HJA sensors are distributed along the valley over a length of nearly 1 km. Thus, the probability that the different sensors see the same meandering motions is much larger at the small MF and MP sites and the two BPP subsites than at the HJA site. This notion is confirmed by the big difference between the calculated filter lengths of the two the BPP subsites in combination with the relatively small standard deviation $\sigma_{\tau_{1\%}}$ within each of the subsites. The terrain at the BPP site is very similar between both subsites, but

the distance between them is about one kilometre (similar to the distance of the farthest sensors at the HJA site). Thus it seems that not differences in terrain but spatial separation lead to big differences between the single sensor's $\tau_{1\%}$. We can thus conclude that it is not possible to find a simple relationship between the terrain and the optimal filter time scale for detection of meandering intervals by the constancy. However the plan is not only to detect meandering, but also to compare the typical time scales between the different sites. In order to facilitate that without a bias due to the detection mechanism, the same filter length should be used for all the sites. Thus, the mean of the site-specific filter lengths from table 5.1 is used, which is $\overline{\tau_{1\%}} = 35$ min. The two-step averaging (first a site specific $\tau_{1\%}$ followed by an average over all the site specific values) is done because of the different number of ground network sensors at the different sites. By computing first a site-specific filter length and averaging those, favouring the sites with more sensors can be avoided.

Using $\overline{\tau_{1\%}} = 35$ min as filter length, a time series of the constancy C can be received like the one in figure. 5.1. It shows the time series of the constancy during the same 6-hour interval as the wind direction and the horizontal wind components in the upper two plots. The rapid drop of the constancy when the directional changes occur is clearly visible.

Finally, the meandering intervals are detected by searching for the minima of the constancy C. Once a minimum is detected, we search for the 'full width at half minimum' around this minimum (i.e. the full width half maximum of $1 - C$, FWHM). All the minima up to $C = 0.5$ are taken into account. This corresponds to the relative strength of the submesoscale flow compared to the large scale flow reaching approximately unity (Mahrt, 2007).

In figure 5.1, the intervals that were judged as meandering by this algorithm are marked with a grey background. Those intervals coincide perfectly with the intervals during which the large directional changes take place and the horizontal wind components keep switching their sign. Thus, the method using the constancy seems very promising for detecting the meandering phenomenon.

5.2 Autocorrelation function - the previous method for identifying meandering

In the following we want to compare our new method of detecting meandering to one that has so far often been used in literature (Anfossi *et al.* 2005; Mortarini *et al.* 2013; Mortarini & Anfossi 2015, Mortarini *et al.* 2016*a*, Cava *et al.* 2017). Thus, the following section shows how this other detection scheme works.

The method is based on the autocorrelation function of the horizontal wind components. Oettl *et al.* (2001) detected that during low wind speed conditions, the autocorrelation function of both horizontal wind components frequently show a negative lobe, while the autocorrelation function of the vertical wind component mostly has the expected exponential form of a turbulent flow. This negative lobe is attributed to the slow horizontal wind oscillations of the meandering. Anfossi *et al.*
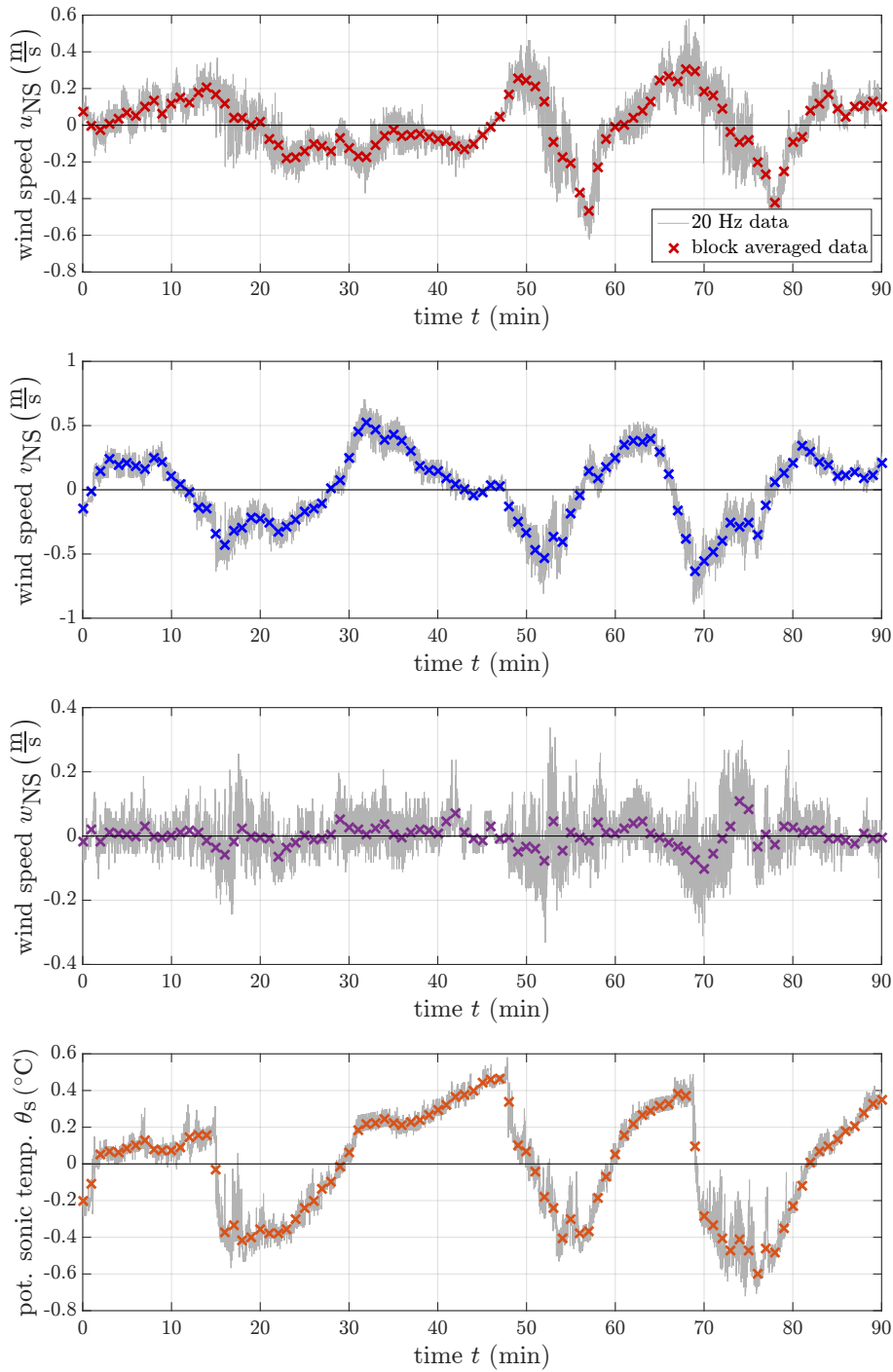
Figure 5.3: Time series of the three velocity components u_{NS}, v_{NS} and w_{NS} and of the sonic temperature θ_s after removing the linear trend.
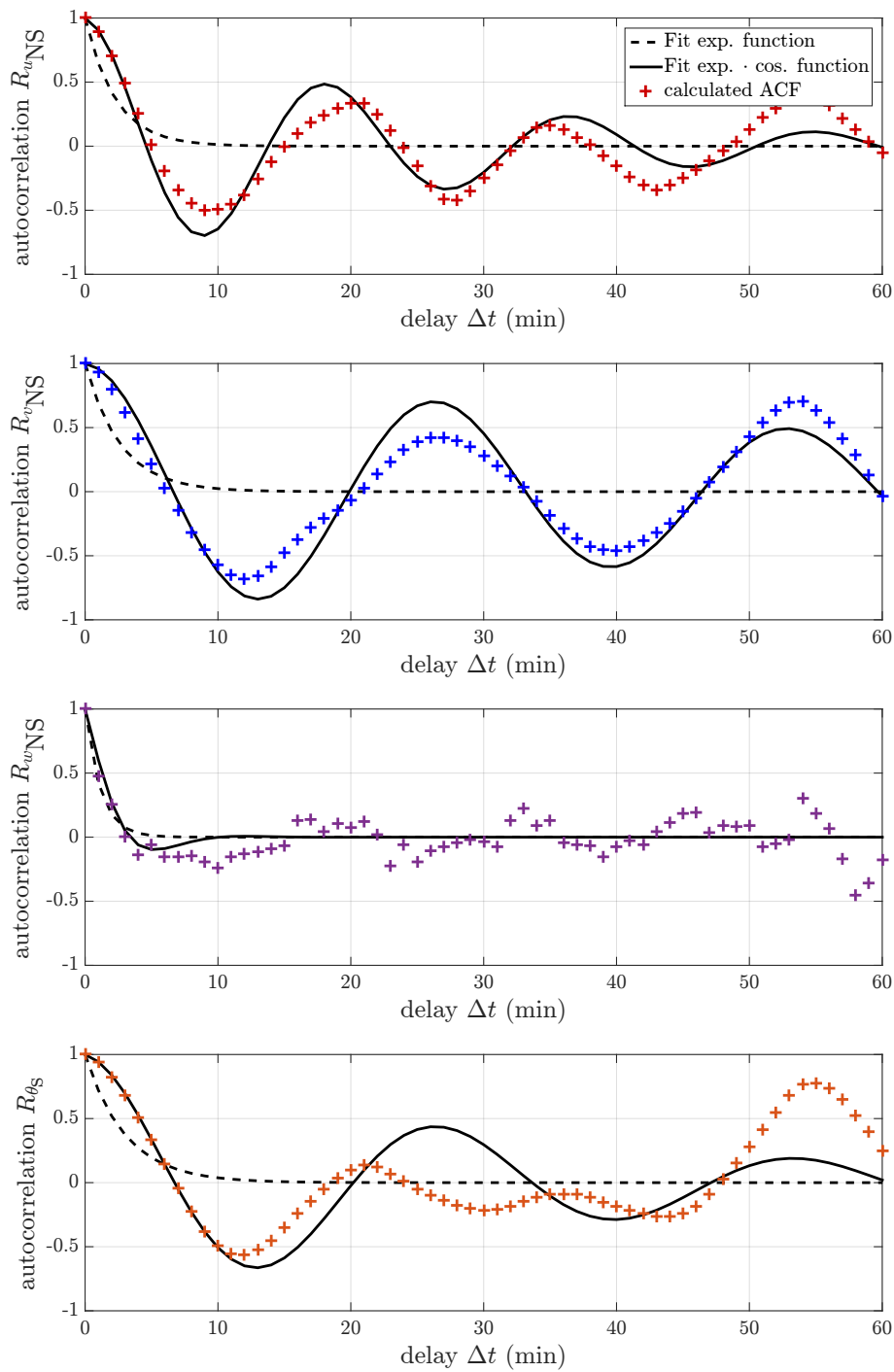
Figure 5.4: Autocorrelation functions of the time series shown in figure 5.3

(2005) showed that the autocorrelation function of the horizontal wind component, from which any linear trend has been removed, can be described by

$$R_{u,v}(\tau) = \exp\left(-p_{u,v}\tau\right)\cos\left(q_{u,v}\tau\right) \tag{5.3}$$

where u is the mean wind direction, v the lateral direction and τ is the delay. While $p_{u,v}$ describes the decorrelation due to turbulence, $q_{u,v}$ gives the typical time scale of the meandering motion. Both, $p_{u,v}$ and $q_{u,v}$ can be obtained by fitting eq. (5.3) to the autocorrelation function of the horizontal wind components during an interval that is to be checked for meandering. Mortarini *et al.* (2013) proposed, using the loop parameter

$$m_{u,v} = \frac{p_{u,v}}{q_{u,v}} \tag{5.4}$$

as a meandering indicator, with $m_{u,v} \geq 1$ during meandering and $m_{u,v} < 1$ during non-meandering conditions. The loop parameter measures the ratio between the oscillation frequency and the inverse of the decorrelation time. High values of $m_{u,v}$ indicate that the decorrelation takes long compared to the oscillation frequency, while for low values of $m_{u,v}$ the oscillation is negligible due to the quicker decorrelation. Also the temperature θ_{s} shows the oscillating autocorrelation function during meandering conditions due to the advection of heat (Mortarini *et al.*, 2016a). Sometimes, also the vertical wind component shows the oscillating behaviour of the autocorrelation. This is however not always the case and no necessary condition for meandering.
For determining, whether or not an interval is meandering according to the autocorrelation method, first any linear trend within that interval is removed by subtracting a linear function fitted to the data (Bendat & Piersol, 2011). Afterwards, the autocorrelation is calculated from the detrended interval. Then eq. (5.3) is fitted to the autocorrelation and the loop parameters $m_{u,v,\theta} < 1$ for both horizontal wind components and the temperature are calculated.
An interval will be called *non-meandering*, if $m_{u,v,\theta} < 1$ and *meandering* if $m_{u,v,\theta} \geq 1$. If at least one loop parameter, but not all of them are greater than unity, the respective interval is called *almost meandering* (Mortarini *et al.*, 2016b). Unlike the previous works we will not do this for fixed intervals of one hour (or two hours in Mortarini & Anfossi (2015)), but for the intervals that are identified as meandering by the constancy method. Furthermore, we resign from rotating the coordinate system to the direction of the mean wind and instead use the coordinate frame of the earth. Figure 5.3 shows the detrended but unrotated time series of all three wind components and of the sonic temperature. Apart from the block averaged data, also the high frequency data from the sonic is shown. The depicted time series corresponds to the second one of the two highlighted meandering intervals in figure 5.1 (from 03:37 AM to 05:07 AM). It is thus an interval that is judged as meandering by the constancy indicator. It is evident that both horizontal components and the temperature show structures on the order of 10 to 20 minutes that strongly exceed the turbulent fluctuations of the 20 Hz time series. Those structures are only very barely visible in the time series of the vertical wind component.

Figure 5.4 shows the autocorrelation of the time series in figure 5.3 (coloured crosses). Additionally, the fit of eq. (5.3) to the calculated autocorrelation is included in each of the plots (black line). For comparison we also include the fit of an exponential function (black dashed line), which does however not describe the autocorrelation properly.

For u_{NS}, v_{NS} and θ_{s}, the autocorrelation function shows a strongly oscillating behaviour. The first negative lobe goes down to -0.5 for the u_{NS} component and even further for v_{NS} and θ_{s}. Because of this, the form of the autocorrelation is much better described by eq. (5.3) than by the simple, exponential decay that would be expected for a turbulent system. The vertical wind component does not show a clear oscillation. This is however no necessary condition for meandering.

The two horizontal wind components' autocorrelations are well captured by eq. (5.3). The time scales of the oscillations are $\tau_{u_{\mathrm{NS}}} \approx 20$ min and $\tau_{v_{\mathrm{NS}}} \approx 26$ min. The loop parameters given by the fit of eq. (5.3) are $m_u = 8.6$ and $m_v = 17.7$.

The fit to the autocorrelation of the sonic temperature is much worse than that for the two horizontal wind components. After a closer comparison of the calculated autocorrelation $R_{\theta_{\mathrm{s}}}$ with the ones of the horizontal wind components, one realizes that $R_{\theta_{\mathrm{s}}}$ seems like a superposition of both, $R_{u_{\mathrm{NS}}}$ and $R_{u_{\mathrm{NS}}}$. This is plausible, as the temperature is horizontally advected by the wind (Mortarini *et al.*, 2016a). It makes thus sense that features from both horizontal wind components appear in the time series of the temperature. The function fitted to the autocorrelation can only take one frequency into account. It is thus not surprising that the fit cannot capture the autocorrelation correctly if there is a superposition. Nevertheless, the first negative lobe, which goes down to -0.5 and which would not happen in the autocorrelation of a purely turbulent time series, is nicely captured by the fit.

The loop parameter of the temperature is $m_{\theta_{\mathrm{s}}} = 7.5$. Thus, all loop parameters are greater than unity and the analysed interval is considered as meandering not only by the constancy, but also by the autocorrelation method. Also the other meandering interval depicted in figure 5.1 is classified as meandering by the autocorrelation method, too. The loop parameters of this interval are $m_u = 5.7$, $m_v = 1.8$ and $m_{\theta_{\mathrm{s}}} = 13.9$.

5.3 Extraction of meandering time scales

If the meandering intervals are detected by their autocorrelation function, one automatically also gets the typical time scales of this meandering motion. These time scales are given by

$$\tau_{u,v,\theta} = \frac{2\pi}{q_{u,v,\theta}} \tag{5.5}$$

where $q_{u,v,\theta}$ are the respective fit parameters from the cosine part of eq. (5.3) for the wind components u_{NS} and v_{NS} and the temperature θ_{s}.

When the constancy is used for detecting meandering, no information on the time scale arises during the detection. It is thus necessary to apply another method for

extracting the typical scales of the observed phenomena. For this purpose, wavelet analysis will be used (Cava *et al.*, 2017).

The wavelet transform is a local transform. Unlike the fourier transform it contains not only information on the frequencies contained in a signal, but also on when these frequencies occur. Thus it is a very good tool for studying non-stationary processes (Collineau & Brunet, 1993). Wavelet analysis can also be used for many other purposes mainly in signal processing like detection of jumps or filtering of signals. In this work it will however only be used for the determination of typical time scales during meandering situations.

The wavelet transform $T_p(a, b)$ of a function $f(t)$ is defined as

$$T_p(a, b) = \frac{1}{a^p} \int\limits_{-\infty}^{+\infty} f(t) \Psi\left(\frac{t - b}{a}\right) \mathrm{d}t \tag{5.6}$$

$\Psi\left(\frac{t-b}{a}\right)$ is called the mother wavelet, a the dilation parameter and b the translation parameter (Thomas & Foken, 2005). The factor $\frac{1}{a^p}$ serves for the normalisation. In this analysis, $p = 1$ is used as suggested by Collineau & Brunet (1993). This corresponds to the L1 norm. It is also possible to use $p = \frac{1}{2}$, which corresponds to the L2 norm (see Gamage & Hagelberg (1993) and Collineau & Brunet (1993) for a discussion on the difference and on which normalisation to choose).

Depending on the purpose of the wavelet analysis, there are many different possible
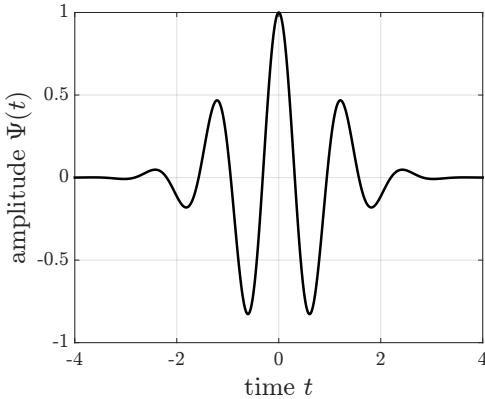
Figure 5.5: Basic form of the Morlet wavelet ($a = 1$ and $b = 0$)

mother wavelets. Some of them are better localised in the frequency space and some better in the time space. With the main interest being the typical durations, we chose the real-valued Morlet wavelet, which is well localised in the frequency domain. The Morlet wavelet, which is shown in figure 5.5, consists of a sine wave windowed by a gaussian function. The wavelet function is given by

$$\Psi(t) = \exp\left(-t^2\right)\cos(5t) \tag{5.7}$$

For extracting the information on the typical time scales, it is necessary to translate

Figure 5.6: Wavelet spectrum of the meandering time series shown in figure 5.3. From top to bottom: u_{NS}, v_{NS}, w_{NS} and θ_{s}.

the dilation parameter a into a time scale. This can be done by

$$D(a) = \frac{1}{2} \cdot \frac{a \cdot 2\pi \Delta t}{\omega^0_{\Psi_{p,1,0}}} \qquad (5.8)$$

The wavelet-specific constant $\omega^0_{\Psi_{p,1,0}} = 0.8125$ is given by the peak frequency of the mother wavelet in the Fourier space with $a = 1$ and $b = 0$ and Δt is the temporal resolution of the input time series. The factor $\frac{1}{2}$ is introduced here in order to get the time scale of single events. An event here consists of a single deviation of the time series upwards or downwards from the mean. Thus, during one period of a sine function, there are two events taking place (Thomas & Foken, 2005).

All in all, the Morlet wavelet transform is very similar to a short-time Fourier transform. However, for the wavelet transform, the width of the window function is scaled depending on the time scale that is currently analysed. Thus, with a wavelet transform, the high frequencies or short lived structures can be much better localized in the time domain than with a short-time Fourier transform. Simultaneously, for a slowly varying function, the Morlet wavelet has a very good resolution in the frequency domain compared to the short-time Fourier transform.
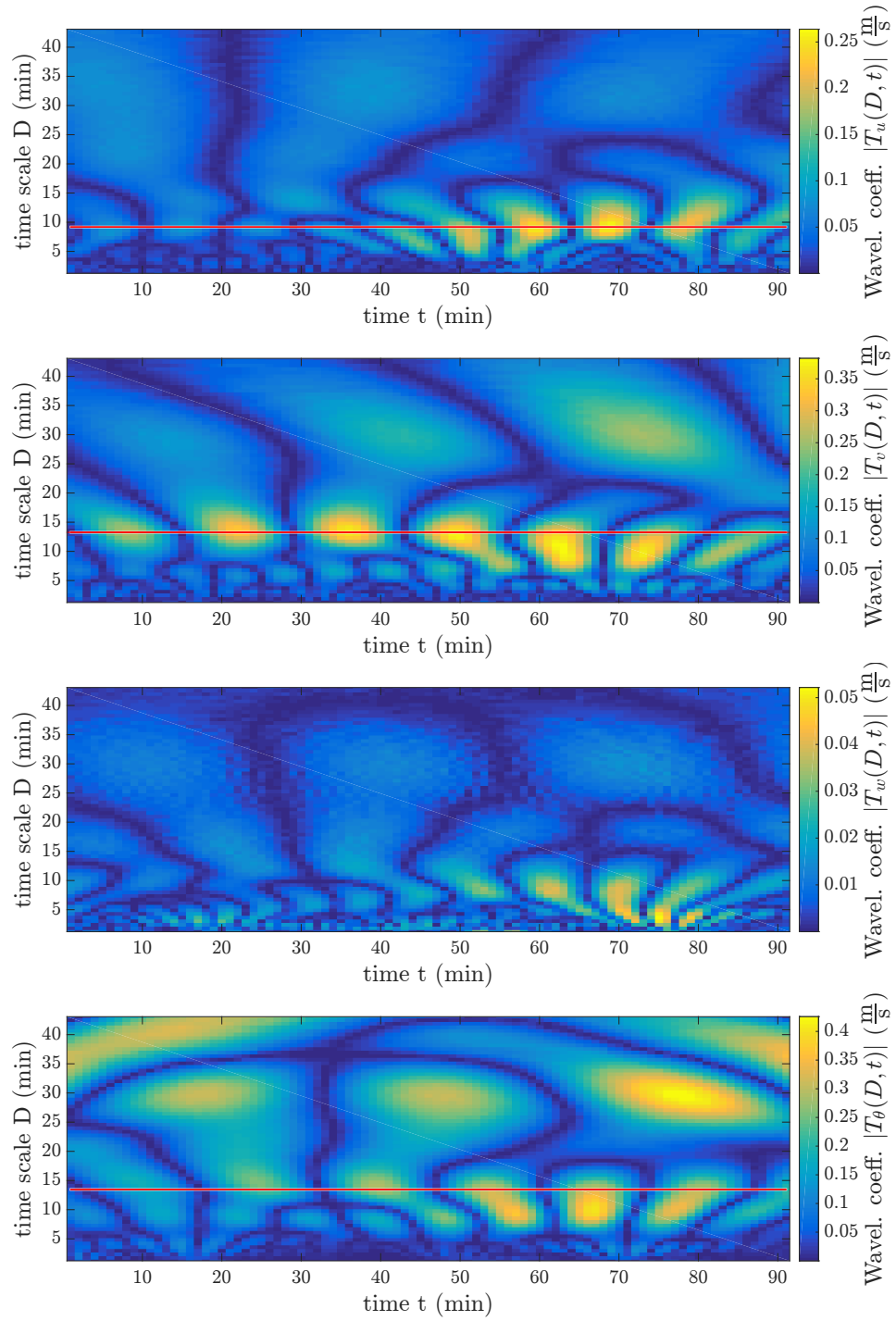
Figure 5.6 shows the wavelet spectrum of the meandering time series shown in figure 5.3. In addition to the time-dependent and scale-dependent wavelet coefficients $|T(D, t)|$, which are represented by a colour code, the plots show a red, horizontal line. This line corresponds to the time scale that was recognized by the autocorrelation function as the dominant time scale of the meandering. For the sake of consistency, the time scale determined by the autocorrelation function is also divided by two in order to refer to single events instead of an oscillation period. Thus, the horizontal line corresponds to $D_{u,v,\theta} = \frac{1}{2}\tau_{u,v,\theta} = \frac{\pi}{q_{u,v,\theta}}$.

From the wavelet coefficients, it is evident that for both horizontal components, there is a clearly dominant time scale (two top plots, fig. 5.6). In the time series of v_{NS}, the activity of this dominant time scale can be observed during the whole period, while for the u_{NS} component, it only is pronounced in the second half of the interval. For both horizontal wind components, the time scale determined from the autocorrelation function perfectly matches the dominant time scale in the wavelet spectrum.

Also in the vertical wind component (third plot from top, fig. 5.6), a dominant time scale can be recognized. Its activity however also only starts in the second half of the interval and thus much later than the meandering. The observed interval seems similar to the one analysed by Cava *et al.* (2017) as an extensive case study. In this study they came to the result that meandering cannot only exist without being triggered by vertical motions but can even trigger gravity waves itself.

In the wavelet spectrum of the temperature time series (bottom plot, fig. 5.6), a complex superposition of different scales can be seen. The difficulties in fitting eq. 5.3 are thus not surprising as this equation considers only one frequency. Still, considering the bad fit, one of the dominant time scales is captured surprisingly well by the autocorrelation function, as can be seen by the horizontal red line.

In order to get the dominant time scale over the whole interval by wavelet analysis,
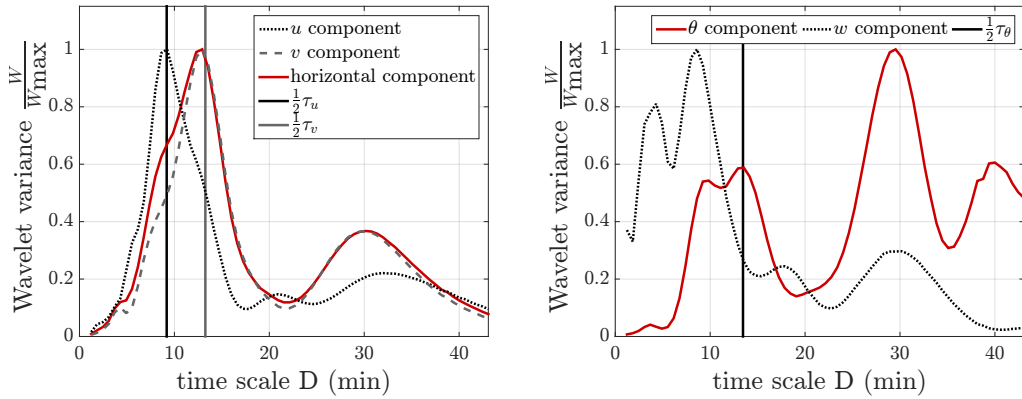
Figure 5.7: Left plot: Wavelet variance spectra of the horizontal wind components u_{NS} (dotted) and v_{NS} (dashed) and a total horizontal spectrum (red continuous line). The vertical lines indicate the time scales given by the respective autocorrelation. Right plot: Wavelet variance spectrum of the temperature θ_{s} and time scale from the autocorrelation $R_{\theta_{\mathrm{s}}}$.

	time scale ACF $\frac{1}{2}\tau_{u,v,\theta}$ (min)	peaks wavel. var. spectrum D_{peak} (min)				
u	**9.2**	**9.2**	20.9	32.0		
v	**13.3**	4.3	**12.9**	30.2		
w	(6.7)	4.3	8.6	17.8	30.2	
θ	**13.5**	3.7	9.8	**13.5**	29.5	40.0

Table 5.2: Comparison of the time scales from the autocorrelation function to the peaks in the wavelet variance spectrum.

a wavelet variance spectrum can be computed. The wavelet variance spectrum is given by

$$W(D) = \int\limits_{-\infty}^{+\infty} |T(D,t)|^2 \mathrm{d}t \tag{5.9}$$

The wavelet variance spectra for both horizontal wind components as well as the temperature θ_{s} can be seen in figure 5.7. Both horizontal velocity components show a distinctive peak at scales around 10 minutes. The peak of the v_{NS} component lies at slightly larger time scales than the one of the u_{NS} component. An additional but much less pronounced peak lies at time scales of $D \approx 30$ min. This time scale corresponds to most pronounced peak in the wavelet variance spectrum of the temperature. It is however too long to be properly visible in a autocorrelation function of a time series that is only 90 minutes long.

The peak at $D \approx 10$ min is the one recognized by the fit of the autocorrelation. This can be seen by the vertical lines that represent the autocorrelation time scales $\frac{1}{2}\tau_{u,v,\theta}$. They correspond perfectly to the peaks in the wavelet variance spectrum.

Table 5.2 shows the scales D_{peak} of all the peaks in the wavelet variance spectra and the meandering time scale from the autocorrelation function $\frac{1}{2}\tau_{u,v,\theta}$. For the sake of completeness, also the 'meandering' time scale from the autocorrelation function of the vertical wind component is included, although a vertical oscillation is not necessary for meandering. This time scale does not match with any of the peaks from the wavelet variance spectrum of the vertical velocity. This is however not surprising as the autocorrelation function of w_{NS} does not show a strong oscillation behaviour and the fit of eq. (5.3) gave a very poor result.

As also the plots in figure 5.6 and 5.7 indicate, for u_{NS}, v_{NS} and θ_{s}, the agreement between both methods on the time scale is very satisfying. This can be seen from the numbers in bold in table 5.2. Especially for the temperature, the compliance between the time scales from the different methods is surprising because the fit of the autocorrelation function does not even look very promising. The wavelet variance spectrum however gives a variety of peak time scales, while the autocorrelation function can give only one due to the design of the fit equation.

As already mentioned, during meandering conditions, there is no distinct mean wind direction. It would thus be advantageous to get the predominant horizontal time scales without allocating a certain direction to the coordinate system. For this purpose, the wavelet spectrum of the horizontal motions can be computed by

$$T_{\text{hor}}(D,t) = \sqrt{T_u^2(D,t) + T_v^2(D,t)} \tag{5.10}$$

From $T_{\text{hor}}(D,t)$ one can compute the wavelet variance spectrum of the horizontal wind speed $W_{\text{hor}}(D)$ by eq. 5.9 (red line in fig. 5.7). In the case shown here, the v_{NS} component was oscillating more strongly and thus the horizontal wavelet variance spectrum is mainly influenced by that of v_{NS}. The peak of the u_{NS} component is barely even visible in the combined spectrum. This shows that the calculation of the horizontal time scale is a very important step in determining the time scale of the meandering motion.

5.4 Comparing the constancy and wavelet method to the ACF

Chapters 5.1 - 5.3 show a nice case study for the comparison between the constancy and the autocorrelation method on an interval that clearly is meandering. For this interval, both methods don't only succeed in assessing it as meandering, but also agree very well on the time scale of the oscillating motion. However, the time series of the temperature also shows that difficulties could arise when there is a superposition of motions with different time scales. The reason for those difficulties is that the fit of the autocorrelation function only takes one time scale into account and thus doesn't perform well, if the time series consists of a superposition of differently sized motions. Thus, there already is some indication that the agreement between both methods might not always be as nice as in the interval discussed above.

In the following chapter, intervals for which the constancy indicator and the autocorrelation indicator don't agree on whether or not it is meandering will be analysed. A closer look at those intervals shows that there are different reasons for the discrepancy between both methods.
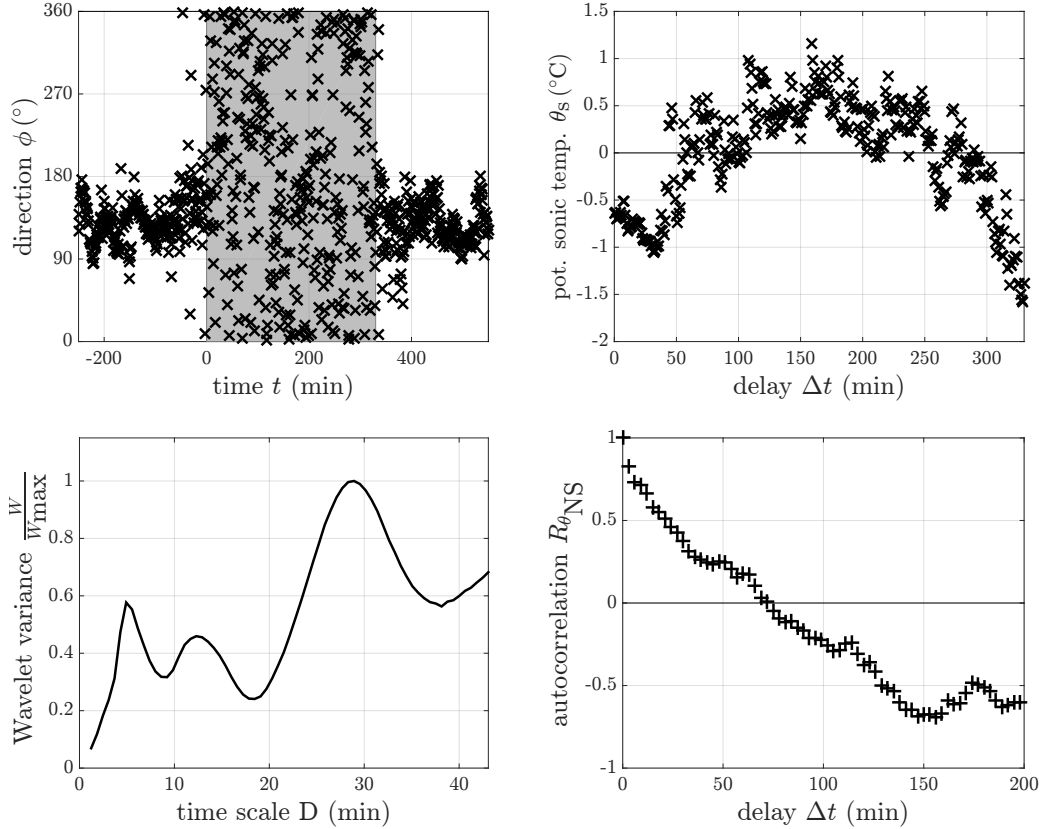
Figure 5.8: *Top left*: Time series of the wind direction which contains a very long meandering interval. Time series (*Top right*), Wavelet variance spectrum (*Bottom left*) and autocorrelation (*Bottom right*) of the potential sonic temperature during the meandering interval.

The first step in the analysis of the discrepancies is to find out, how many of the intervals classified as meandering by the constancy method are also judged as meandering by the autocorrelation. For this purpose however we have to consider one problem first, which is the diurnal course of the variables and especially of the temperature. This problem is only important for very long meandering intervals, as e.g. the one in figure 5.8.

During the long interval, the temperature undergoes a strong, non-linear shift due to its diurnal course (see top right plot, fig. 5.8). This shift is much stronger than any fluctuations due to advection of warmer or colder air by meandering. As a result,

(%)	BPP	BPP (Moritz)	MP	HJA (val.)	HJA (sl.)	MF
meandering	18.6	29.8	5.8	18.0	38.3	52.1
almost meandering	76.5	46.5	35.4	67.3	53.1	42.6
not meandering	13.9	23.7	58.9	14.7	8.6	5.4

Table 5.3: Percentage of meandering intervals according to constancy that are classified as meandering, almost meandering and not meandering by the loop parameters.

for a very long period of meandering, the linear detrending that is applied before calculating the autocorrelation is not enough for removing the diurnal trend. Consequently, the autocorrelation function is 'blind' to all the other, weaker fluctuations (fig. 5.8, bottom right plot). It will always give back a too long time scale because of the diurnal variations. The smaller fluctuations that are present in the time series according to the wavelet variance (fig. 5.8, bottom left plot) are not detected by the autocorrelation method.

As a workaround, in order to get a reasonable result when comparing both detection methods, the long meandering periods are cut into shorter pieces before analysing them with the autocorrelation function. This is a reasonable approach as also in the works done so far with the autocorrelation function, the intervals tested for meandering normally were only 60 minutes long. Mortarini & Anfossi (2015) also tested using longer intervals of 120 minutes. They see that the shorter interval of 60 minutes might lead to some meandering events not being recognized correctly. However they also state that using a too long interval does not make sense due to unavoidable instationarity. Thus, the necessity to cut the very long meandering intervals into shorter pieces is easily justifiable.

In order to decide, how long the pieces should be into which the too long time series is cut, it makes sense to remember that the averaging length for the constancy is $\overline{\tau_{1\%}} = 35$ min. During this period, the wind direction has to cover at least a sector of $120°$ in order to be recognized by the constancy indicator as meandering in case of a sudden jump of the wind direction. In case of a very gradual change of direction (equidistant steps), the directional change within 35 minutes must exceed $217°$ for being detected. For meandering motions that cover the full range of $360°$ this would mean that a full oscillation can take up to 56 minutes and still be identified. It is thus clear that using intervals of 35 minutes for the autocorrelation analysis is too short as not even a full oscillation will be completed during this period. Instead, we will use units of 70 minutes, which corresponds to twice the filter length. This way, more than one complete oscillation can take place during the interval and at the same time the diurnal course is not a problem.

The interval will thus be cut into as many intervals of length $L = 70$ min as possible. The remainder after that is attached to the last interval, resulting in intervals that can be 139 minutes at most. This is in a similar range as the interval length used by Mortarini & Anfossi (2015) and thus still a reasonable length.

Apart from cutting the time series into pieces, for intervals where the autocorrelation

(%)	BPP	BPP (Moritz)	MP	HJA (val.)	HJA (sl.)	MF
all agree	34.7	32.0	23.5	44.8	40.9	33.0
some agree	65.3	65.0	76.5	54.1	58.1	64.3
none agree	0	3	0	1.2	1.0	2.7

Table 5.4: Percentage of intervals where all the typical time scales (some/none of the time scales) determined with the autocorrelation function agree with the ones determined from the wavelet variance spectrum for the intervals that are classified as meandering by both methods.

(%)	BPP	BPP (Moritz)	MP	HJA (val.)	HJA (sl.)	MF
all agree	10.2	8.5	2.0	6.0	13.9	4.9
some agree	80.3	77.3	76.5	83.5	80.8	87.6
none agree	9.1	14.2	21.6	10.5	5.3	7.6

Table 5.5: Percentage of intervals where all the typical time scales (some/none of the time scales) determined with the autocorrelation function agree with the ones determined from the wavelet variance spectrum for the intervals that are classified as meandering by the constancy and as almost mendering by the autocorrelation function.

function gives a time scale greater than $D = 35$ min , we assume that the fit detected a variation due to the diurnal course instead of a fluctuation due to meandering and set the loop parameter to zero. $D = 35$ min corresponds to an oscillation period of 70 min, which is the limit of oscillations that can be reliably identified by the constancy. The process for excluding diurnal variations could certainly still be optimized but this was not done within the scope of this master thesis.

Being now able to avoid misjudging the diurnal course for meandering, it is interesting how often both methods of detection for meandering agree. For this purpose, the autocorrelation function is fitted for every interval that was identified by the constancy. If the interval is too long it is cut into pieces as described above and then the fit is done for each subinterval. Each of the (sub-)intervals is assigned to one of the groups 'meandering', 'almost meandering' and 'not meandering' according to its loop parameter (see chap. 5.2). Table 5.3 shows, how many of the intervals that are meandering according to the constancy are meandering, almost meandering or not meandering due to the autocorrelation function. The numbers shown in table 5.3 are the average of all the ground network stations at the given site.

By far the worst coincidence between the two methods can be found at the MP site, where nearly 60% of the meandering intervals found by the constancy are classified as not meandering by the autocorrelation function. Only 5.8% of the intervals are determined as meandering according to the autocorrelation and 58.9% are judged as non-meandering. At all the other sites, the results are much more encouraging. The best coincidence can be found at the MF site, where only 5.4% of the intervals are not

meandering due to the autocorrelation function and more than 50% are meandering. At all sites except MP one can observe that most of the intervals are attributed to the 'almost meandering' group by the autocorrelation function.

It is not only important to know how well both methods agree on whether or not there is meandering, but also the reliability of the detected time scale is interesting. The time scale given by the wavelet analysis is quite reliable as the Morlet wavelet was used, which has a very good localization in the frequency space. The time scale detection of the autocorrelation function however seems not very trustworthy, due to its difficulties in dealing with a superposition of different motions. Additionally, the autocorrelation function is prone to give the wrong time scale when a slow trend is present in the data, for example due to the diurnal cycle. Last but not least, it is doubtful how well a time scale can be detected from a autocorrelation function, if only a few cycles of the event take place during the analysed interval. Making the analysed interval longer is no option because than the diurnal cycle would start playing a role. Furthermore, in the atmosphere often not more than a few cycles can be observed.

Table 5.4 shows the percentage of intervals where all (some/no) time scales agree, in case both methods identified the interval as meandering. If the autocorrelation of both horizontal wind components as well as the temperature indicate meandering, almost always at least some of the time scales from the autocorrelation function agree. Nevertheless, for the bulk of the meandering intervals, only some of the time scales agree between the methods and not all of them. In the case of 'almost meandering' behaviour according to the autocorrelation, the percentage of intervals where some of the time scales agree is bigger than in the case of 'meandering'. This group includes around 80% of all the 'almost meandering' cases. Also the percentage of cases where none of the time scales agree rises for the 'almost meandering' case compared to the 'meandering' one. This group accounts for approximately 10% of all the 'almost meandering' cases.

It is not clear, which time scale is the correct one in case the two methods disagree. Due to the reasons discussed above however, the time scale given by the wavelet analysis seems more trustworthy.

Knowing that the autocorrelation and the constancy method don't always agree on whether or not a situation should be acknowledged as meandering, we now want to analyse the reason for those discrepancies.

First of all meandering often is caused by a complex superposition of motions (Mahrt, 2007). As a result, there sometimes is more than one predominant frequency in the meandering motion. As eq. (5.3) only considers one frequency of oscillation, this sometimes leads to a failing of the fit. The failing of the fit sometimes 'only' leads to a wrong time scale that is detected by the autocorrelation function, but sometimes it also leads to the autocorrelation function not detecting the meandering at all.

Figure 5.9 shows an example of an interval where motions of two different time scales occur simultaneously. In the top left plot, the time series of the wind direction during this interval is shown. It is evident that during the interval, the wind direction covers the complete possible range from 0° to 360° and thus is clearly meandering according
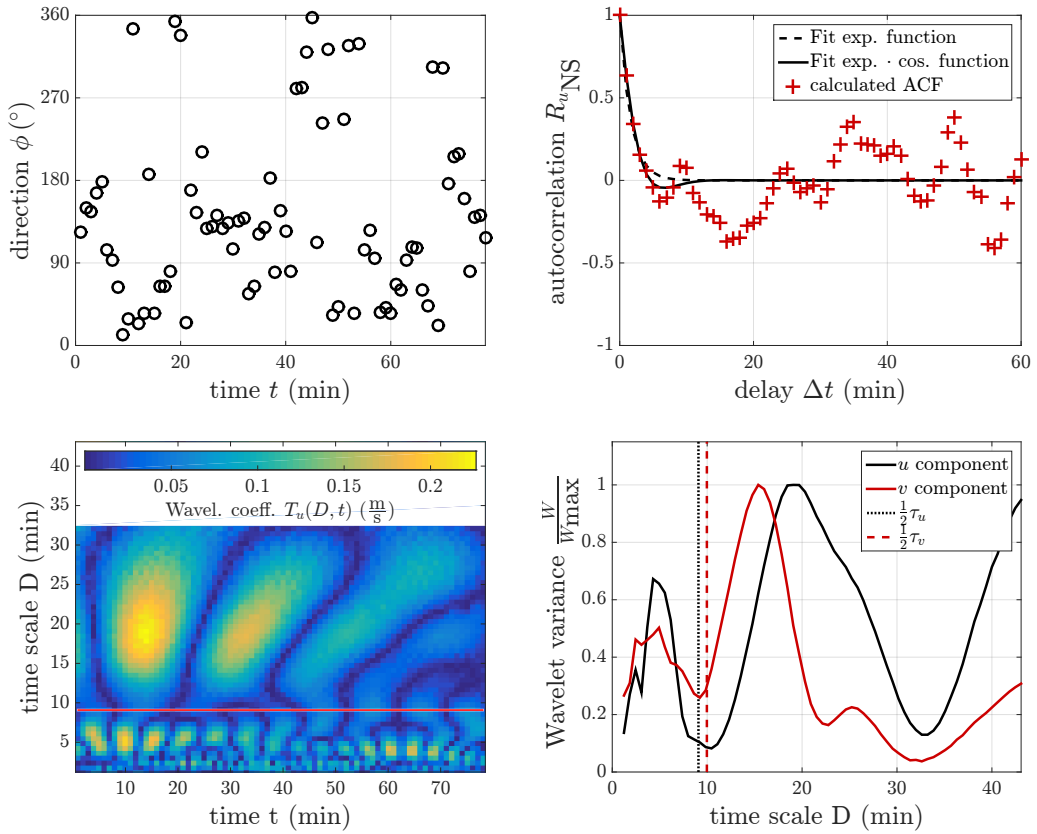
Figure 5.9: *Top left:* Time series of the wind direction during a meandering interval detected by the constancy method. *Top right:* Autocorrelation of the u_{NS} component during this interval and fit of the expected autocorrelation function during a meandering interval (continuous line) and a during a turbulent interval (dashed line). *Bottom left:* Wavelet spectrum of u_{NS}. *Bottom right:* Wavelet variance spectrum of u_{NS}.

to the constancy method. Regarding the autocorrelation of the u_{NS} component one can clearly see that it does go down far below zero, as it is expected for a meandering interval. However, the oscillation of the autocorrelation function is very irregular. As a result, the fit of eq. (5.3) does not succeed in capturing the oscillation and looks similar to a simple exponential decay instead. The loop parameter from this fit is $m_u = 0.86 < 1$ which hints at a non-meandering interval. Also for the second horizontal wind component, v_{NS} (not shown), the loop parameter $m_u = 0.54 < 1$ does indicate meandering. Only the loop parameter from the temperature θ_s is greater than unity and thus makes the interval 'almost meandering' according to Mortarini *et al.* (2016*b*). The time scale of the oscillation given by the fit of the temperature autocorrelation however is $\tau_\theta = 65.7$ min, which is a very dubious result from a time series that is only about 80 minutes long.

At the bottom of figure 5.9, the wavelet spectrum and the wavelet variance spectrum
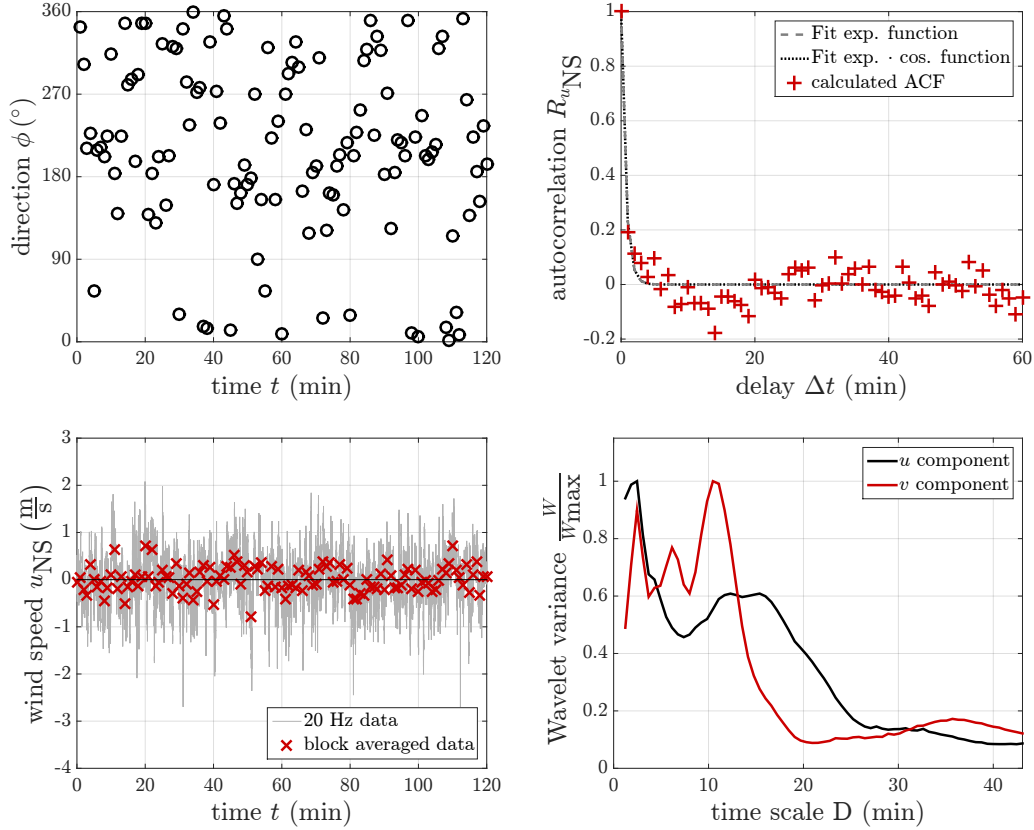
Figure 5.10: *Top left:* Time series of the wind direction during an interval where turbulence was possibly misjudged as meandering; *Top right:* Autocorrelation of the u_{NS} component during this interval and fit of the expected autocorrelation function during a meandering interval (dotted line) and during a turbulent interval (dashed line); *Bottom left:* Time series of the 20 Hz data and the block averaged data; *Bottom right:* Wavelet variance spectrum of u_{NS}.

of the u_{NS} component (and v_{NS} for the wavelet variance spectrum) are shown. It is clearly visible that there is a superposition of events with a time scale of around 20 minutes and ones with around five minutes. Also the time scales $D_{u,v} = \frac{1}{2}\tau_{u,v} = \frac{\pi}{q_{u,v}}$ that result from the fit of the autocorrelation function are shown. They clearly do not fit to the time scales shown by the wavelet spectrum. All in all, figure 5.9 shows an example of a meandering situation that is only judged as almost meandering according to the autocorrelation method. Furthermore, the time scales that the autocorrelation method gives back are completely wrong as the fit cannot properly describe the superposition of two different time scales.

From visual inspection of the autocorrelation functions in the cases with discrepancies between the autocorrelation and the constancy method, it appears that the super-

position of different time scales is the most frequent reason for the autocorrelation function not or only partially detecting the meandering.

Another example, of an interval where the two methods don't agree on whether or not it is meandering is shown in figure 5.10. Again, the wind covers all possible directions during the depicted interval. However the situation is different this time as apart from a lot of scatter, the autocorrelation of the u_{NS} component hardly dips below zero. Also the time series of one horizontal velocity component during the interval (bottom left of fig. 5.10) looks different than the clear meandering time series shown in figure 5.3. The difference is that now, the rapid fluctuations of the original 20 Hz time series shown in gray are large compared to the fluctuations of the block-averaged data with a temporal resolution of 1 minute. Furthermore, the wavelet variance spectrum (bottom right) shows a peak at the smallest time scales that it can resolve. Intervals with behaviour like described above occur almost only during the day. Particularly often they can be found at the MP site. MP is the only site, where this kind of 'meandering interval' can be found during the night, too.

The preferred time of occurrence as well as the very small dominant time scale found from the wavelet spectrum and the form of the autocorrelation function all hint that during these intervals, the constancy indicator is actually not detecting meandering, but turbulent fluctuations of the wind direction. This is probably caused by the turbulence during the day not being confined to the same small scales as during
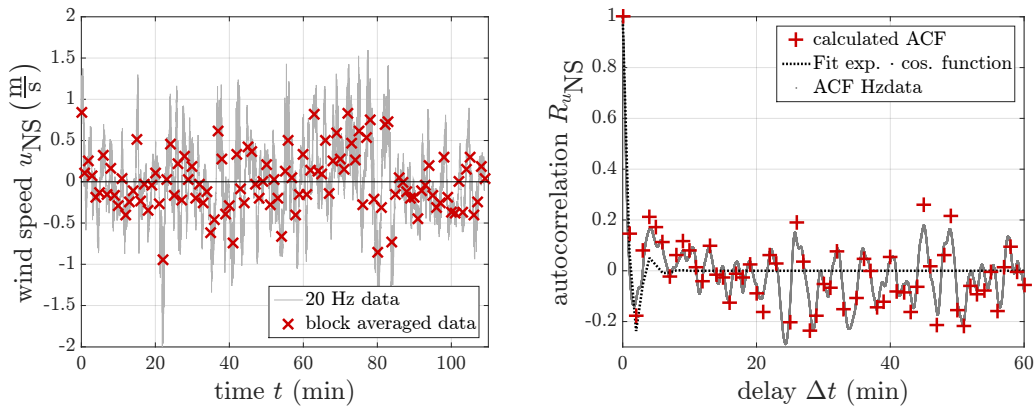
Figure 5.11: *left*: time series of the u_{NS} component during a 'meandering interval' detected by the constancy; *right* Autocorrelation of the block averaged data (red crosses) and the 20 Hz data (grey dots forming a line) and the fit of the expected function for a meandering situation (black dotted line)

the night. Because of that, in the block averaged data, some turbulent fluctuations are still included. In order to avoid the accidental detection of turbulent phases as meandering it would probably help to adapt the perturbation time scale T_p. For this purpose, the method of Vickers & Mahrt (2003) could be used in order to detect the best perturbation time scale during the night and during the day respectively. It is however unlikely that a distinct cospectral gap can be found during the day, as then

the scales of submeso motions and of turbulence might overlap. All in all, the chosen time scale $T_\mathrm{p} = 1$ min is probably too short during the day, but finding a proper one is a challenge.

As the intervals of possibly misjudged turbulence happen exceptionally often at the MP site, this probably is the reason for the bad coincidence between the constancy and the autocorrelation method at this site (see tab. 5.3). This raises the suspicion that the perturbation time scale $T_\mathrm{p} = 1$ min is actually not a good choice for the MP site. The choice of a proper perturbation time scale is thus of vital importance for identifying meandering via the constancy.

Also the autocorrelation function sometimes judges intervals as meandering or almost meandering where it is doubtful if the oscillations that can be seen are actually meandering or turbulence. One example of such a situation can be seen in figure 5.11. The left plot shows the time series of an interval that is judged as meandering. The 1 minute block averaged time series is represented by the red crosses and the 20 Hz time series is shown as as continuous grey line. Again, the interval takes place during the day (8.40 AM to 10:30 AM) and again also the block averaged time series seems to fluctuate rapidly. This time however two out of three loop parameters (m_u and m_θ) are greater than unity and thus classify the interval as almost meandering. For the u_NS component, the autocorrelation function from the block averaged data and also the one from the 20 Hz data are shown in the right plot of figure 5.11. One can see that this time, the fitted autocorrelation function recognizes the first dip below zero of the autocorrelation. As a result, the loop parameter for the shown autocorrelation is $m_u = 2.0$. The time scale that the fitted autocorrelation gives back is $D_u = \frac{1}{2}\tau_u = 2.2$ min. This is similar to the dominant time scale from the wavelet variance spectrum $D = 2$ min, which is again at the very limit of time scales that can be resolved. All in all, the interval has all of the properties that were identified as a indication for turbulent fluctuations being misjudged as meandering. Thus, both methods, the autocorrelation as well as the constancy, might sometimes mistake turbulent fluctuations as meandering. However, at least at the BPP, HJA and MF sites, this problem vanishes when excluding daytime data.

It is now clear that the constancy performs better than the autocorrelation method at recognizing meandering if there is a superposition of motions with different scales. On the other hand, if the perturbation time scale was chosen too short the constancy cannot differentiate between the directional changes due to turbulence and those due to mesoscale phenomena. The problem is less pronounced when using the autocorrelation function as an indicator, but also then some intervals remain dubious. When using the constancy, the problem of misinterpreted turbulence might be resolved by choosing a site-dependent and day/night dependent perturbation time scale according to the cospectral gap method (Vickers & Mahrt, 2003). This was however not done in the scope of this master thesis.

Next, it is interesting how many meandering intervals the autocorrelation method finds during periods that are non-meandering according to the constancy. For this purpose, too long intervals are again split into pieces of 70 minutes like described above. This serves again the purpose of the diurnal course not impeding the detection
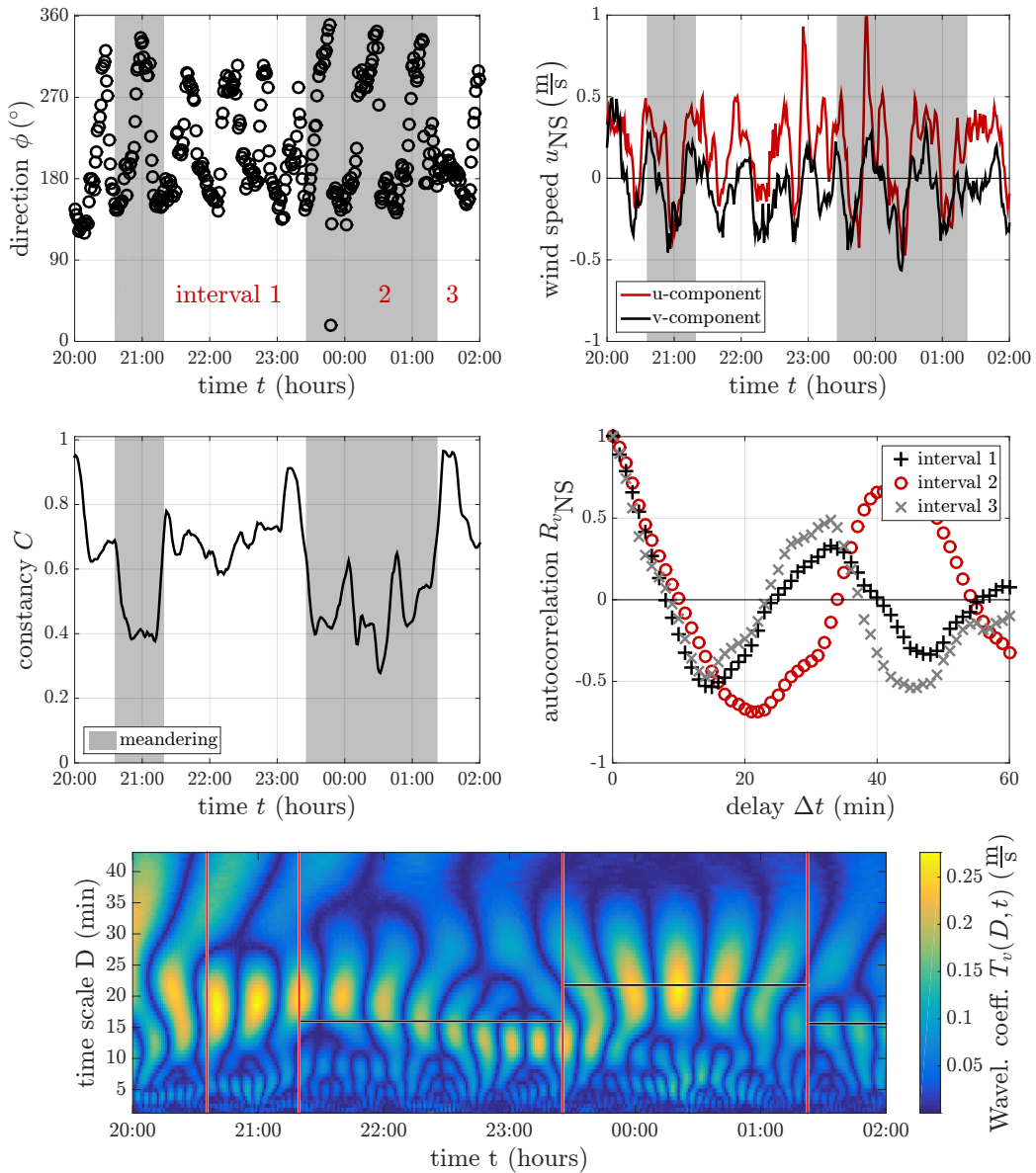
Figure 5.12: Interval where sometimes directional changes are too small to be discovered by the constancy *Top left*: Time series of the wind direction ϕ. Intervals that are detected as meandering by the constancy are marked in grey. ; *Top right*: Time series of the two horizontal wind components u and v ; *Middle left*: Time series of the constancy C ; *Middle right*: Autocorrelation of the three intervals marked with 1, 2 and 3 in the top left plot (interval 1: 9:20 pm - 11:26 pm, interval 2: 11:26 pm - 1:23 am, interval 3: 1:23 am - 2:35 am). The earlier intervals are shorter than 70 minutes and thus no autocorrelation is calculated ; *Bottom:* Wavelet spectrum; Intervals detected by the constancy are marked with vertical red lines. For the intervals that are at least 70 minutes, the meandering time scale given by the autocorrelation function is marked with a horizontal black line.

(%)	BPP	BPP (Moritz)	MP	HJA (val.)	HJA (sl.)	MF
meandering	0.5	4.2	3.6	7.3	14.0	8.8
almost meandering	18.3	17.2	52.2	65.3	53.7	74.1
not meandering	81.1	78.6	44.4	36.4	32.3	17.1

Table 5.6: Percentage of non-meandering intervals according to constancy that are classified as meandering, almost meandering and not meandering by the loop parameters.

of meandering.

Table 5.6 shows the percentage of intervals that the autocorrelation function judges as meandering, almost meandering or not meandering when the constancy doesn't detect meandering. While the result looks promising for the BPP site (less than 5% meandering according to the autocorrelation when constancy says non-meandering), all the other sites show a disappointing result. Especially at the MF site, only 17.1% of the intervals that are non-meandering according to the constancy are also classified as non-meandering by the autocorrelation function. It is thus important to investigate the reason for the autocorrelation function discovering so much more meandering than the constancy.

Visual inspection of the intervals in question suggests three main reasons for the discrepancies.

1. Sometimes, wind directions don't cover the whole range of 360° but only a smaller angle. This is shown in figure 5.12 for a 6-hour interval, which is characterized by quite regular directional changes occurring during the complete period (top left plot). The wind directions however only span roughly 180°. The exact range that they cover varies slightly over time, with a slightly smaller range from 9:20 PM to 11:26 PM and after 1:23 AM. As a result, the constancy during those intervals with a slightly smaller range of wind directions doesn't fall below 0.5 and the intervals stay undetected by the constancy method. The autocorrelation function however correctly detects the oscillating behaviour during the intervals 1, 2 and 3 and classifies all of them as meandering (see second row, right plot; loop parameters : $m_1 = 9.0$, $m_2 = 14.2$ and $m_3 = 6.9$). The time scales that the autocorrelation gives for them is marked with a horizontal black line in the wavelet spectrum (bottom plot, fig. 5.12). The good agreement between the dominant time scale in the wavelet spectrum and the time scale from the autocorrelation is obvious.

   The two intervals that are not marked with a number in figure 5.12 are shorter than 70 minutes. This means that they are shorter than the lower limit set for a meandering interval for being analysed with the autocorrelation. This limit was set because for too short intervals the autocorrelation cannot reliably detect the slowly fluctuating behaviour of the wind components. The directional time series as well as the wavelet spectrum however suggests that also during the two earlier intervals, regular fluctuations of the horizontal wind velocity already

exist and thus meandering is already present.

The interval in figure 5.12 shows, that situations with regular wind directional changes exist, during which not the whole range of 360° is covered. Due to the limit of $C < 0.5$ that determines meandering situations with the constancy method, the intervals with a too small range of directions are missed. The range that has to be covered during an interval of 35 minutes (i.e. the filter length) is 120° for the ideal case an abrupt change of direction of 180°. For a very gradual change of direction with equidistant steps, the change within 35 minutes needs to be at least 217°, in case the absolute value of the wind speed stays constant. The numbers that are necessary for the directional change being recognized vary when the wind speed doesn't stay constant and when the change of direction neither goes abruptly nor in equidistant steps. This dependence of the detection scheme on how the directional change happens certainly is a disadvantage in
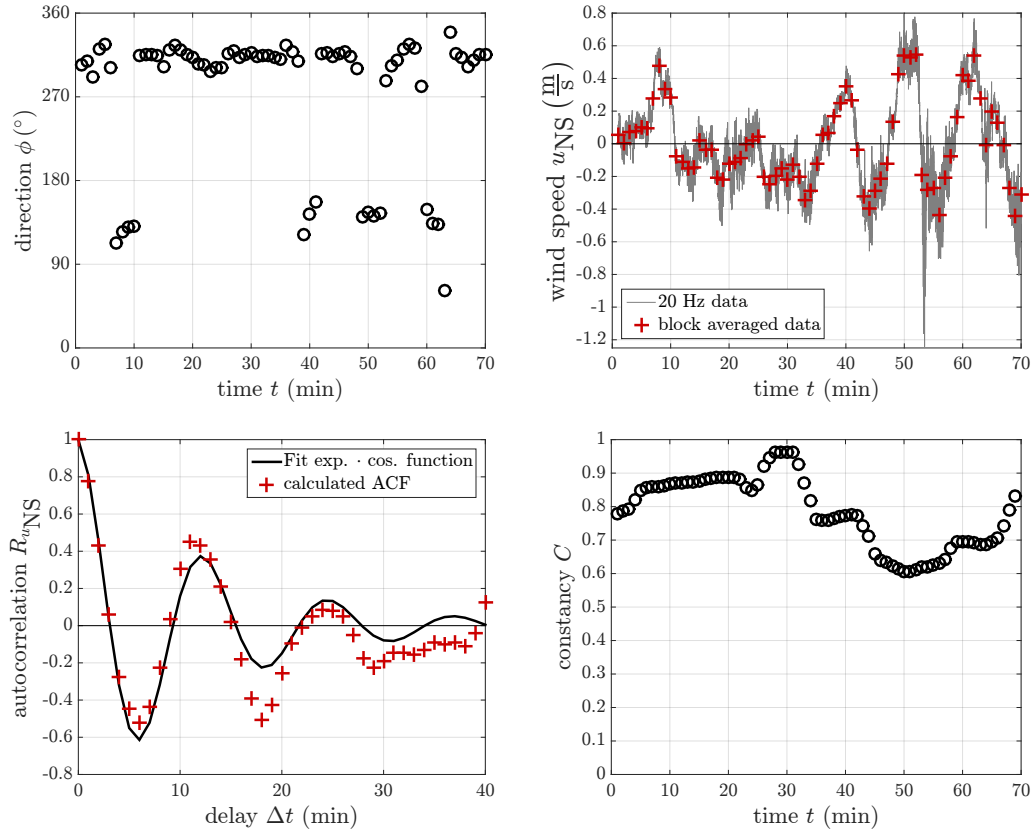

Figure 5.13: Interval with a dominant wind direction with some strong but short changes of direction. *Top left:* Time series of the wind direction ϕ.; *Top right:* Time series of one of the horizontal wind components (u_{NS}); *Bottom left:* Autocorrelation of u_{NS}; *Bottom right:* Time series of the constancy C.

the constancy method. It would be possible to adapt the limit of the constancy, from which on a interval is classified as meandering. However, the optimal limit of the constancy seems to be site dependent (not shown). No further analysis was done for determining the site-dependent optimal limit for detecting the constancy.
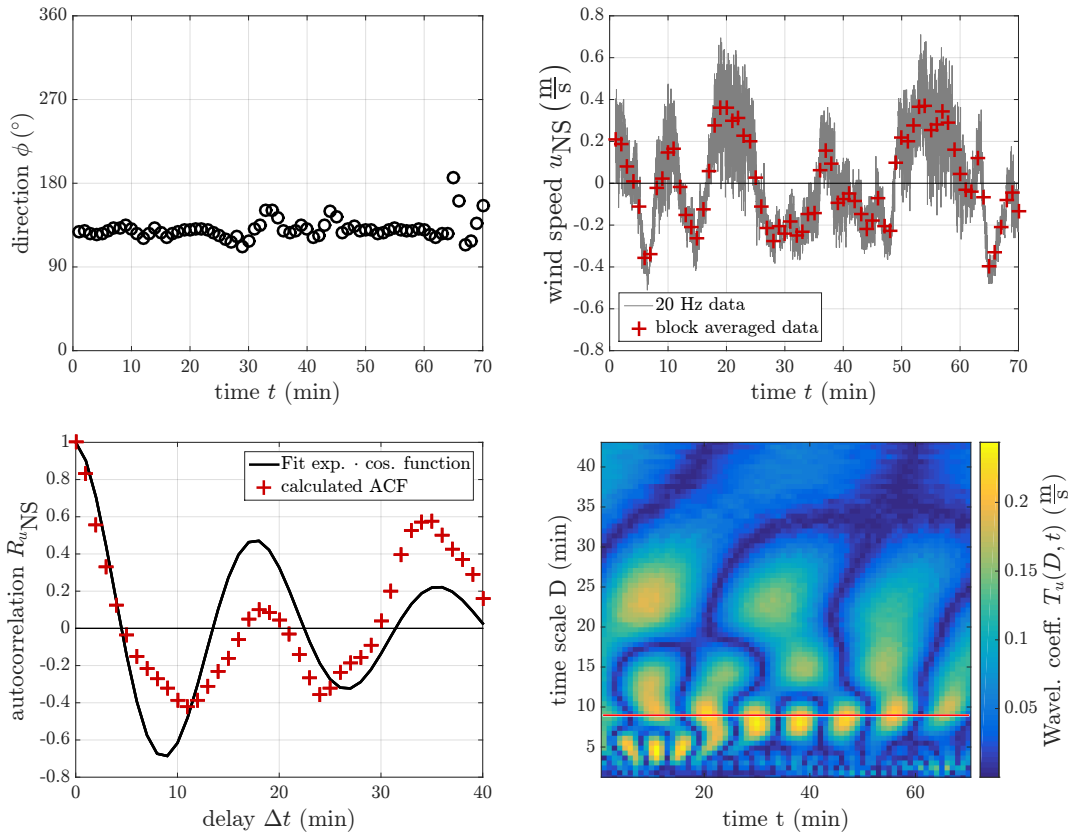
Figure 5.14: Interval without directional changes but other wavelike structures in the horizontal wind components *Top left:* Time series of the wind direction ϕ; *Top right:* Time series of one of the horizontal wind components (u_{NS}); *Bottom left:* Autocorrelation of u_{NS}; *Bottom right:* Wavelet spectrum with the time scale extracted by the autocorrelation function marked with a horizontal red line.

2. Sometimes, a clearly dominant wind direction exists, which is from time to time interrupted by a sudden and strong wind directional change (fig. 5.13, after 10 minutes, 40 minutes, 50 minutes and 60 minutes) The new wind direction stays stable for a couple of minutes (one symbol in figure 5.13 corresponds to one minute) and then the old dominant wind direction takes over again. This behaviour is especially typical for the HJA site, where due to the narrow valley basically only two wind directions exist (down the valley and up the valley). It

can however also be found at the other sites, albeit to a lesser extent.

In the plot of the horizontal wind component u_NS, each of the shifts of wind direction is connected to a peak in u_NS. Those quite regular peaks are easily detected by the autocorrelation function, which gives the loop parameters $m_u = 6.3$, $m_v = 4.3$, $m_\theta = 3.2$. For the u_NS component, the autocorrelation function as well as the fit is shown in the bottom left plot of figure 5.13. The oscillating behaviour can clearly be seen. The constancy however stays higher than 0.5 for the complete interval because of the strong predominance of one direction. The secondary direction needs to be present for at least 9 minutes (not necessarily coherent) during a 35 minutes interval so that the constancy drops below 0.5. As a result, the constancy method fails at identifying the directional changes in the interval shown in figure 5.13.

3. The autocorrelation sometimes detects intervals as meandering, where actually the wind direction stays constant during the complete interval. During the interval shown in figure 5.14, no major directional changes take place (see top left plot). Only after 30-40 minutes, some fluctuations of the wind direction occur, but they are less than 30°.

   In case of the wind speed however, slow fluctuations are quite obvious and results in loop parameters of $m_u = 8.4$, $m_v = 4.4$ and $m_\theta = 9.9$. This can be seen in the top right plot (time series of u_NS) and in the bottom left plot (autocorrelation of u_NS and fit) of figure 5.14. The autocorrelation function thus clearly characterizes the interval as meandering.

   Also the wavelet spectrum shows that structures on the order of 10 minutes occur during the interval, which corresponds to the time scale that the autocorrelation gives back as the dominant one. This means that during the observed interval, some structures do occur in the atmospheric boundary layer leading to an oscillation of the horizontal wind components. However, with meandering being defined as slow but strong changes of wind direction, what is observed certainly is not meandering. Thus, the autocorrelation method can accidentally identify the wrong kind of motions.

All in all, the constancy method misses some intervals if the changes of wind direction cover a too small range or if there is a strongly dominating wind direction. However, many of the intervals identified as meandering by the autocorrelation but not by the constancy actually correspond to a different kind of motions. This means that both methods might misinterpret some motions as meandering that are actually something different. Besides, both methods might not be able to identify some actually meandering situations. Which situations are accidentally detected and which ones are missed depends on the method used for identification of meandering. The difference in which situations are missed and which ones might accidentally be detected could be used as a criterion for deciding which method to use for the detection of meandering.

Apart from the ability to deal with a superposition of differently sized motions, another big advantage of the constancy method is that the identification can be done

very quickly compared to the autocorrelation method, where three functions have to be fitted for every interval in order to decide whether is is meandering, almost meandering or not meandering. This is especially useful, if block averaged wind speeds have already been calculated with a proper perturbation time scale, as it was the case in this work.

Furthermore, using the autocorrelation method, it is necessary to decide beforehand, how long the intervals to be analysed for meandering should be. The original time series then has to be cut into pieces of this length and every one of those pieces has to be analysed. With the constancy method on the other hand, the complete time series can be analysed at once. Besides, the starting and the ending time of a meandering period can be found much more exactly using the constancy, as with the autocorrelation method one is bound to the intervals into which the time series was cut.

On the other hand, the autocorrelation immediately gives a typical time scale of the meandering motion, while with the constancy method one has to apply some additional work in order to get that. The time scale given by the autocorrelation is however not very reliable in case there is a superposition of different motions.

5.5 Some statistics on weak wind and meandering

Finally, we will make use of the weak-wind threshold and the new meandering indicator to get some statistics on weak-wind and meandering situations and the connection between both. Furthermore, we look at the site dependence of those statistics.

(%)	BPP	BPP (Moritz)	MP	HJA (valley)	HJA (slopes)	MF
overall	23	21	40	17	22	26
day	11	11	56	14	19	27
night	36	31	13	21	28	24
during sw	13	13	46	4	12	8
during ww	66	42	25	26	26	27

Table 5.7: Average percentage of meandering situations for each site. *First line*: during the complete period, *second line*: during the day, *third line*: during the night, *fourth line*: during strong wind situations, *fifth line*: during weak-wind situations;

Table 5.7 shows, how often meandering happens at the four sites. For computing those numbers, first all meandering situations are determined for each sensor respectively. The percentage is calculated by taking the ratio of the number of minutes classified as meandering to the number of minutes during the measurement period. The overall ratio for a given site is then calculated by averaging over the ratios of all ground network stations of the respective site. Apart from the overall percentage, the table also shows the percentage of meandering during the day and during the night and also

(%)	BPP	BPP (Moritz)	MP	HJA (valley)	HJA (slopes)	MF
overall	19	27	31	62	81	95
by day	5	10	22	47	70	93
by night	35	46	45	82	96	96

Table 5.8: Percentage of weak-wind situations overall, during the day and during the night at the different sites.

during weak-wind and during strong-wind situations. For deriving the percentages of meandering within the different categories, only the minutes associated to the respective category are used. Then the ratio of the meandering minutes to the overall number of minutes within the category is taken. For defining the weak-wind and strong-wind category, the scalar averaged wind speed and the threshold wind speed derived in chap. 4.1 are used. For differentiating between day and night, we use a day-night indicator which is given back by the Bmmflux program for every minute. For calculating that, the day of the year and the geographic position are taken into account for calculating the time when the sun sets behind the horizon. The transition time during sunset and sunrise is excluded from table 5.8.

At the HJA site and the BPP site, the ground network stations are additionally split into two different subgroups. At the BPP site those subgroups are the main site on the one hand and the Moritz site on the other hand. At the HJA site, the one subgroup consists of all the sensors on the valley bottom, while the sensors of the other group are all located on the slopes. Thus, at the BPP site, the two subgroups are separated spatially by approximately one kilometre, but the terrain is very similar between them. At the HJA site on the other hand, the two subgroups are not separated by a big spatial distance compared to the distance between the sensors within one subgroup. Instead, the subgroups are fundamentally different regarding the terrain. As an addition to the table on meandering, table 5.8 shows the percentage of weak-wind situations at the different (sub-)sites. Due to the different weak-wind thresholds at the different sites, a higher percentage of weak-wind does not necessarily show that the wind speed at this site is lower. The table shows that, as expected, much more weak-wind situations can be found during night. Only at the densely forested MF site, the difference between day and night is very low, as there are always predominately weak-wind situations. For the HJA site, the same weak-wind threshold is for both subgroups. Thus, table 5.8 indicates that the wind speed is generally higher at the valley bottom than at the slopes, resulting in less weak-wind situations at the bottom. It is evident from table 5.7 that for most sites, there are much more meandering situations during the night and during weak-wind situations than there are during strong-wind situations and during the day. This is exactly what we would expect, as submeso motions are more prominent during weak-wind situations and weak-wind situations occur most often during the night. Also Mortarini *et al.* (2016*b*), using the autocorrelation method noted that meandering is much more frequent during the night. Furthermore, we can confirm that also during strong wind situations,

sometimes meandering can be observed, but less frequently than during weak winds. This was also noted by Anfossi *et al.* (2005) but with a much higher wind speed as a weak-wind threshold.

At the MF site, there are a bit more meandering intervals during the day than during the night. This is probably due to the fact that at this site winds are generally very weak and thus also during the day, weak-wind situations prevail. If one differentiates by weak wind and strong wind instead of by night and day, the MF site again shows the expected behaviour, with very little meandering during strong wind situations. This suggests that at least at the MF site, actually the wind speed is more important for the existence of meandering than the time of the day.

The next thing that catches the eye is that by far the most meandering situations are identified at the MP site, while for the other sites, the percentages are very similar. This peculiarity is particularly strong during the day and during strong-wind situations. During weak-wind situations and during the night, the percentage of meandering situations on the other hand is much lower at the MP site than at al the others. Furthermore, the rule that there is more meandering during weak wind or during the night respectively than during strong wind or during the day seems not to apply to the MP site.

Unfortunately, this anomaly is probably caused by the erroneously identified meandering intervals that were already mentioned in chapter 5.4. The combination of unexpectedly many meandering cases during strong wind with very little meandering during weak wind supports the suspicion that at the MP site, we might misjudge turbulent fluctuations for meandering. Another possibility is that some of the motions identified as meandering are actually a rotor caused by the airflow being forced above the nearby ridge of the Cascade mountains. During the night, the turbulent fluctuations are confined to much smaller scales. As a result, the 'meandering situations' identified during the night are more likely to actually be caused by submesoscale motions and thus the ones that we originally wanted to detect. Still, the data on meandering from the MP site should not be over-interpreted.

At the HJA site, a systematic difference can be seen between the valley stations and the slope stations. For every single category, the percentage of meandering cases is lower at the valley bottom than at the slopes. Especially during strong-wind situations, hardly any meandering occurs at the valley bottom. Only for the weak-wind cases, meandering shows a similar frequency of occurrence for both subgroups.

Probably, there are three reasons for this difference between the valley bottom and the slopes. On the one hand, as already mentioned, winds are generally weaker at the slopes than at the valley bottom. This can explain, why overall as well as in the categories 'day' and 'night' meandering is more frequent at the slopes, as lower wind speeds favour meandering. This is supported by the fact that for weak-wind situations, the probability of meandering is nearly as high in the valley as at the slopes. However, during strong-wind situations, meandering is nearly three times as likely at the slopes than at the valley floor. This indicates that there is an additional cause for the different frequencies of occurrence. The most likely causes can be seen from the very special distribution of wind directions at the bottom of the deeply
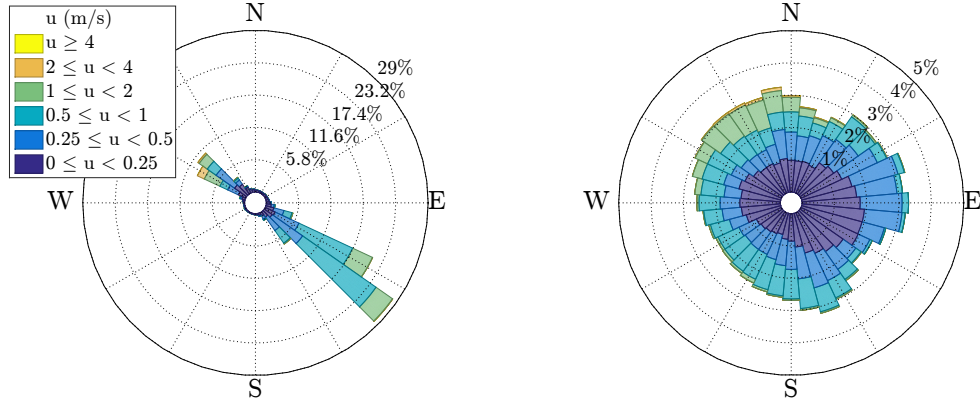
Figure 5.15: *Left*: Distribution of wind directions at the A3 sensor at HJA (valley bottom); *Right*: Distribution of wind directions at the A4 sensor at HJA (slope)

incised valley. As you can see in the wind rose plot figure 5.15, the flow at the valley bottom of HJA is strongly channelled. It can only move either downstream or upstream, but hardly ever perpendicular to the valley axis. Thus, the trigger for meandering probably needs to be much stronger at the bottom of the valley compared to a place where every wind direction is possible. At the slopes, the upstream and downstream directions are much less dominant. This is first and foremost true for the A4 station, which is the one placed farthest away from the valley bottom (right plot, fig. 5.15). At this station, more than 40 % of the time, meandering can be detected. Also at the the WS1_Top station, which is located above the canopy in a height of 38 m, more meandering situations than the average of HJA can be found. Also at this station the flow is less channelled (see wind direction distribution in figure 2.9). Last but not least, cold air drainage can only happen at the deepest locations within the valley and only close to the ground. Presumably, also cold air drainage and its fixed downward wind direction can reduce meandering. It is thus very likely that the strong topography impedes meandering at the valley bottom.

Apart from the difference between the two HJA subgroups, no big systematic differences can be found between the sites. Actually the differences in the probability of meandering between weak wind and strong wind are much stronger than the differences between the single sites. Thus, again, the most important criterion for whether meandering happens is the wind speed, except with extremely strong topography.

Apart from when meandering occurs, also the time scales of the meandering motions and their dependence on the wind speed and the time of the day can be analysed. Unfortunately, at the shortest time scales that can be detected with the perturbation time scale $T_p = 1$ min, we cannot be sure if the observed phenomenon actually is a submeso motion or if the directional changes are caused by turbulence. On the other hand, the length of the filter for calculating the constancy can lead to very slow
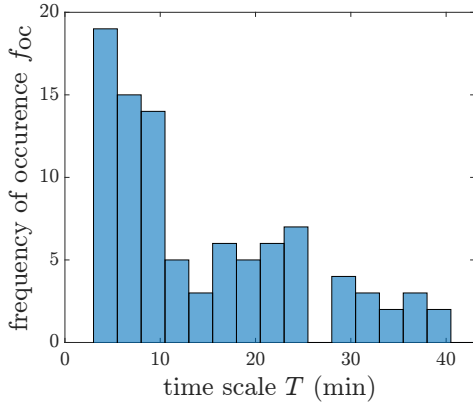
Figure 5.16: Distribution of the meandering time scales of the A1 sensor at HJA.

(min)	BPP	BPP (Moritz)	MP	HJA (valley)	HJA (slopes)	MF
overall	14.4	14.5	11.9	13.9	13.2	14.3
by day	13.2	13.8	11.6	12.7	11.8	13.0
by night	14.8	14.8	13.5	15.0	14.5	15.5
during sw	14.0	13.8	11.6	11.7	10.7	-
during ww	14.7	15.3	14.0	14.0	13.5	14.3

Table 5.9: Average time scales of the meandering motion at the different sites overall, during the day/night and during weak-wind/strong-wind situations.

directional chances not being recognized. If a change of direction needs longer than the filter length $\tau_{1\%} = 35$ min for a angular change of at least $120°$, it can not be recognized. We thus probably register too many events with a very short time scale and possibly too few events with a very long time scale. Unfortunately the same problem concerning the influence of the detection mechanism on the detected time scales exists when using the autocorrelation method (Mortarini *et al.*, 2013).

The distribution of the time scales, which is exemplary shown for station A1 in HJA in figure 5.16 may thus result from a systematic error in our detection scheme. The time scales shown in this figure are the ones extracted by a wavelet analysis for every single meandering interval, as explained in chapter 5.3. A similar distribution can be found for all sensors of the ground networks. Even if the exact form of the distribution is doubtful, we can conclude from fig.5.16 that a broad variety of meandering time scales exists. This is true for each of the analysed sites.

Table 5.9 shows the mean time scale of the meandering motions for all (sub-)sites. It is clear that due to the uncertainty concerning the influence of our filter on the detected time scales, no quantitative conclusions should be drawn from this table. Nevertheless, it should be possible to draw some qualitative conclusions on whether or not the time scale is site dependent.

Apart from the mean time scale of all the meandering intervals ('overall', tab. 5.9), the intervals are again sorted depending on whether they happen during weak wind

or during strong wind and whether during the day or during the night. During each meandering interval, there can be a mix of minutes classified as weak wind and minutes classified as strong wind due to fluctuations in the wind speed. As for each interval, the wavelet variance spectrum gives only one set of dominant time scales however, we want to assign the whole interval either to weak wind or to strong wind. There are two possibilities for doing the allocation.

The first option is deciding for every single minute, if it belongs to weak wind or to strong wind. If the majority of the minutes within one meandering interval belongs to weak wind, the whole interval could be attributed to the weak-wind category. The second possibility is calculating the average scalar wind speed during the complete interval. If this average wind speed is less then the threshold velocity, the complete interval is taken into account in the category 'during weak-wind'. For table 5.9, the second method was used. However, no big differences arise when using the other method.

For differentiating between 'by day' and 'by night', we use again the day-night indicator from Bmmflux. Again, the interval has to be allocated wholly to one group or the other. Thus, when more than three quarters of an interval happen during the day, the complete interval is attributed to the 'by day' group and vice versa. The exact limit for when an interval can be attributed to either group is of minor importance as only qualitative conclusions will be drawn.

It is evident from table 5.9 that regarding the time scales, there are only small differences between the different sites. On average, the time scales are shortest at the MP site (11.9 min). This can however also be due to the large number of possibly turbulent intervals that were misjudged as meandering at this site. Also the two subgroups of the HJA, the valley stations and the slop stations show very similar average time scales, although they are quite different concerning the frequency of occurrence of meandering.

Slightly bigger differences than between the different sites can be found between the categories day and night and between weak wind and strong wind. The time scales during the nightly intervals are generally larger than the ones during the day. Similarly, time scales during strong wind are smaller than during weak wind. Unfortunately this difference can again be caused by turbulence misinterpreted as meandering, as this is much more likely during the day than during the night.

In order to get good quantitative results on the typical distribution of time scales for a given site, it would be necessary to further evaluate the effect of the filter length on the one hand and the optimal perturbation time scale for not misjudging turbulence as meandering on the other hand. This however was not done for this thesis. We can however conclude that no big difference exists between the meandering time scales of the different sites.

6 Conclusion

We used data from a network of 12 sonic anemometers and 12 thermohygrometers for detecting and analysing weak-wind situations. This network of sensors was deployed at four sites with strongly different vegetation and topography for one to two months at each site. With this data, the following analysis was conducted

- We used the dependence of the friction velocity u_* on the mean wind speed for determining a threshold for weak-wind situations. At all sites, a wind speed could be found, starting from which the friction velocity and thus the turbulence are stronger influenced by the wind speed. This is true independent from whether the scalar or the vector average is used for computing the mean speed.

  The threshold velocity of the weak-wind regime turned out to be strongly dependent on the location of the sensor. Strong differences could be found between sensors at different sites but also between sensors at the same site when the surrounding is very different (e.g. subcanopy vs. within the canopy). Sensors in very similar surroundings showed a very similar weak-wind threshold. For the subcanopy sensors, there seems to exist a connection between the tree density and the threshold velocity. This connection could however not be confirmed beyond doubts due to considerable scatter. Especially the large variability at the HJA site complicated the derivation of a correlation between the threshold and the surroundings.

- We tried to verify the hypothesis that a weak-wind situation in the subcanopy indicates a decoupling of the bole space from the flow above the canopy. Coupling or decoupling should be indicated by the different relationships between the vertical wind's standard deviation σ_w above and below the canopy.

  At the BPP site, the air flow at the highest sensor seems to be decoupled from the one at the lowest sensor during weak-wind situations. For the other sites however, a decoupling could not be verified, as the slope in the dependence of subcanopy turbulence from above canopy turbulence is the same for weak-wind and for strong-wind cases. Nevertheless, the amount of turbulence in the subcanopy at a given amount of turbulence above the canopy is very much smaller during weak-wind situations than during strong-wind situations.

  Some doubts arose about this method of identifying decoupled situations when we compared the different ratios of subcanopy to above canopy turbulence with weak-wind and strong-wind situations separated to the ratio when no separation was done. The higher slope that has so far been used as a sign for coupling of subcanopy to above the canopy might actually be caused by strong-wind

situations becoming more frequent than weak-wind situations at a higher above canopy turbulence.

- We developed a new indicator for meandering motions. This methods makes use of the difference between the vector average and the scalar average for finding intervals with lots of directional changes. By using the block averaged data with a perturbation time scale of $T_\mathrm{p} = 1$ min we can make sure that (mostly) only non-turbulent directional changes are detected. It also became clear that great care has to be taken about the proper perturbation time scale for making that work reliably. For determining the dominant time scale(s) of the detected meandering motion, we used a wavelet transform. The Morlet wavelet is used as a mother wavelet due to its good performance in the frequency space.

- The new method for detection of meandering was compared to a well established one, namely the autocorrelation method. The new methods has advantages when a superposition of different motions is present. Furthermore, it can make sure that the detected motions are really connected to directional changes and not a different kind of submesoscale motions, as may happen with the autocorrelation method. Last but not least, the beginning and the end of a meandering period can be found more exactly. On the other hand, intervals with a too small range of directions or intervals with one direction that is too dominant compared to the directional changes are missed.

- The new detection method was used for getting some statistics on meandering. As expected, meandering is more prevalent during the night and during weak-wind situations. Similarly, weak-wind situations are more frequent during the night. The average time scales of meandering motions hardly vary between the different sites. At all of the sites, a broad range of time scales can be found with shorter time scales occurring more often than longer time scales. The average time scale seems to be a bit longer during weak-wind situations (or nights respectively) than during strong-wind situations (or days), but that might be caused by misinterpretation of turbulent fluctuations as meandering.

A The procedure of Reynolds averaging

The procedure of Reynolds averaging and the subsequent calculation of turbulent perturbations can be divided into four steps. First of all, a running average is applied. This can be written as

$$u_j = \frac{1}{N+1} \sum_{n=k-\frac{N}{2}}^{k+\frac{N}{2}} u_n \tag{A.1}$$

where u_n is the original time series of 20 Hz and N is the number of data within one perturbation time scale. In case of the perturbation time scale $T_\mathrm{p} = 1$ min this corresponds to 1200 data points.

The next step after the application of the moving average is downsampling, so that only one data point per perturbation time scale is retained.

$$u_k = u_j \cdot \delta \left(j - Nk + \frac{N}{2} \right) \tag{A.2}$$

The resulting time series is the time series of the mean Reynolds averaged quantity. For computing the perturbations, this quantity first has to be re-expanded by a Zero Order Hold. As we want the interval to be centred around the one data point that is retained, the Zero Order Hold additionally has to be shifted backwards by half an interval

$$u_l = u_k \cdot \mathrm{rect}_D \left(l - k \right) \tag{A.3}$$

with the discrete rectangular function

$$\mathrm{rect}_D \left(l - k \right) = \begin{cases} 0, & \text{if } |l - k| > \frac{N}{2} \\ 1, & \text{if } |l - k| \leq \frac{N}{2} \end{cases}$$

The new time series u_l has again the same number of data points as the original one u_n. For retaining the turbulent perturbation u'_n, the time series u_l simply has to be subtracted from u_n:

$$u'_n = u_n - u_l \tag{A.4}$$

B Fit ranges for the hockeystick curves

The following table contains the ranges that where used for fitting the hockeystick curves in order to identify the weak-wind threshold.

Site	SUSAN unit	range ($\frac{m}{s}$)	comment
BPP, main	all except A1 and C1	0.1 - 0.6	all ground network sensors at BPP main
BPP, main	A1 and C1	0.1 - 1.5	the higher sensors at BPP main
BPP, Moritz	all B sensors	0.1 - 1.0	
MP	all A and C sensors, B3 sensor	0.1 - 1.0	all subcanopy sensor
MP	B1 and B2 sensor	0.1 - 4.0	the above canopy sensors at MP
HJA	all A sensors, C1 and C2 sensor	0.2 - 1.0	
HJA	all B sensors, C3 and C4 sensor	0.2 - 1.5	
MF	all C sensors, B1 - B3	0.1 - no upper limit	all except the sensor right at the upper edge of the canopy
MF	B4	0.1 - 1	edge of canopy sensor

Table B.1: Ranges for fitting the hockeystick curves for finding the weak-wind threshold

Acknowledgement

Bibliography

Acevedo, Otávio C, Moraes, Osvaldo LL, Degrazia, Gervásio A, Fitz-jarrald, David R, Manzi, Antônio O & Campos, José G 2009 Is friction velocity the most appropriate scale for correcting nocturnal carbon dioxide fluxes? *Agricultural and forest meteorology* **149** (1), 1–10.

Anfossi, D, Oettl, D, Degrazia, G & Goulart, lA 2005 An analysis of sonic anemometer observations in low wind speed conditions. *Boundary-Layer Meteorology* **114** (1), 179–203.

Aubinet, Marc, Vesala, Timo & Papale, Dario 2012 *Eddy covariance: a practical guide to measurement and data analysis*, 1st edition. Dordrecht; Heidelberg; London; New York: Springer Science & Business Media.

Belušić, Danijel & Mahrt, Larry 2008 Estimation of length scales from mesoscale networks. *Tellus A* **60** (4), 706–715.

Bendat, Julius S & Piersol, Allan G 2011 *Random data: analysis and measurement procedures*, , vol. 729. John Wiley & Sons.

Cava, D, Mortarini, L, Giostra, U, Richiardone, R & Anfossi, D 2017 A wavelet analysis of low-wind-speed submeso motions in a nocturnal boundary layer. *Quarterly Journal of the Royal Meteorological Society* **143** (703), 661–669.

Collineau, Serge & Brunet, Yves 1993 Detection of turbulent coherent motions in a forest canopy part i: Wavelet analysis. *Boundary-Layer Meteorology* **65** (4), 357–379.

Daly, Christopher, Conklin, David R & Unsworth, Michael H 2010 Local atmospheric decoupling in complex topography alters climate change impacts. *International Journal of Climatology* **30** (12), 1857–1864.

Deaves, DM & Lines, IG 1998 The nature and frequency of low wind speed conditions. *Journal of Wind Engineering and Industrial Aerodynamics* **73** (1), 1–29.

Drake, Stephen, Kingzett, Laura, McGinity, John & Thomas, Christoph K. 2012*a* ARCFLO 2012 field report.

Drake, Stephen, Mahrt, Larry, Orozco, Javier, Smoot, Alex, Thomas, Christoph K. & Zeeman, Matthias J. 2012*b* ARCFLO-DONUTSS 2011 field report.

Bibliography

DUYNKERKE, PETER G 1999 Turbulence, radiation and fog in dutch stable boundary layers. *Boundary-Layer Meteorology* **90** (3), 447–477.

FINNIGAN, JJ, CLEMENT, R, MALHI, Y, LEUNING, R & CLEUGH, HA 2003 A re-evaluation of long-term flux measurement techniques part i: averaging and coordinate rotation. *Boundary-Layer Meteorology* **107** (1), 1–48.

FINNIGAN, JOHN J. & SHAW, ROGER H. 2008 Double-averaging methodology and its application to turbulent flow in and above vegetation canopies. *Acta Geophysica* **56** (3), 534–561.

FOKEN, T 1991 Die universelle Funktion nach Skeib - Grundlage für Massstabsbetrachtungen in der atmosphärischen Bodenschicht. *Zeitschrift für Meteorologie* **41** (1), 1–7.

FOKEN, THOMAS & NAPO, CARMEN J 2008 *Micrometeorology*, , vol. 2. Springer.

DE FÉRIET, J. KAMPÉ 1951 Averaging processes and reynolds equations in atmospheric turbulence. *Journal of Meteorology* **8**, 358–361.

GAMAGE, NIMAL & HAGELBERG, CARL 1993 Detection and analysis of microfronts and associated coherent events using localized transforms. *Journal of the atmospheric sciences* **50** (5), 750–756.

GERMANO, M. 1987 On the non-reynolds averages in turbulence. *AIAA 19-th Fluid Dynamics and Lasers Conference* .

GERMANO, M. 1992 Turbulence: the filtering approach. *J. Fluid Mech.* **238**, 325–336.

GOULART, ANTÔNIO GO, DEGRAZIA, GERVÁSIO A, ACEVEDO, OTÁVIO C & ANFOSSI, DOMENICO 2007 Theoretical considerations of meandering winds in simplified conditions. *Boundary-layer meteorology* **125** (2), 279–287.

HOLTSLAG, AAM, SVENSSON, GUNILLA, BAAS, P, BASU, S, BEARE, B, BELJAARS, ACM, BOSVELD, FC, CUXART, J, LINDVALL, JENNY, STEENEVELD, GJ *et al.* 2013 Stable atmospheric boundary layers and diurnal cycles: challenges for weather and climate models. *Bulletin of the American Meteorological Society* **94** (11), 1691–1706.

HOLTSLAG, BERT 2006 Preface: Gewex atmospheric boundary-layer study (gabls) on stable boundary layers. *Boundary-Layer Meteorology* **118** (2), 243–246.

IRVINE, J, LAW, BE, MARTIN, JG & VICKERS, D 2008 Interannual variation in soil co2 efflux and the response of root respiration to climate and canopy gas exchange in mature ponderosa pine. *Global Change Biology* **14** (12), 2848–2859.

KAIMAL, JC & BUSINGER, JA 1963 A continuous wave sonic anemometer-thermometer. *Journal of Applied Meteorology* **2** (1), 156–164.

Kaimal, J.C. & Finnigan, J.J. 1994 *Atmospheric Boundary Layer Flows: Their Structure and Measurement*, 1st edition, chap. 7, pp. 255–275. New York; Oxford [u.a.]: Oxford University Press.

Kristensen, Leif, Jensen, Niels Otto & Petersen, Erik Lundtang 1981 Lateral dispersion of pollutants in a very stable atmosphere?the effect of meandering. *Atmospheric Environment (1967)* **15** (5), 837–844.

Lee, X., Massman, W. & Law, B. 2000 *Handbook of Micrometeorology: A Guide for Surface Flux Measurement and Analysis*, 1st edition. New York; Boston; Dordrecht; London; Moscow: Kluwer Academic Publishers.

Liang, Jiening, Zhang, Lei, Wang, Ying, Cao, Xianjie, Zhang, Qiang, Wang, Hongbin & Zhang, Beidou 2014 Turbulence regimes and the validity of similarity theory in the stable boundary layer over complex terrain of the loess plateau, china. *Journal of Geophysical Research: Atmospheres* **119** (10), 6009–6021.

Lowe, Paul R 1977 An approximating polynomial for the computation of saturation vapor pressure. *Journal of Applied Meteorology* **16** (1), 100–103.

Mahrt, Larry 2007 Weak-wind mesoscale meandering in the nocturnal boundary layer. *Environmental Fluid Mechanics* **7** (4), 331–347.

Mahrt, L 2014 Stably stratified atmospheric boundary layers. *Annual Review of Fluid Mechanics* **46**, 23–45.

Mahrt, L, Sun, Jielun & Stauffer, David 2015 Dependence of turbulent velocities on wind speed and stratification. *Boundary-Layer Meteorology* **155** (1), 55–71.

Mahrt, Larry, Thomas, CK & Prueger, JH 2009 Space–time structure of mesoscale motions in the stable boundary layer. *Quarterly Journal of the Royal Meteorological Society* **135** (638), 67–75.

Mahrt, L & Thomas, Christoph K 2016 Surface stress with non-stationary weak winds and stable stratification. *Boundary Layer Meteorology* **159** (1), 3.

Manual, R.M. YOUNG COMPANY 2017 ultrasonic anemometer model 81000VRE - Instructions. URL http://www.youngusa.com/products/6/46.html – Zugriffsdatum: 29.06.2017.

Monin, AS & Obukhov, AMF 1954 Basic laws of turbulent mixing in the surface layer of the atmosphere. *Contrib. Geophys. Inst. Acad. Sci. USSR* **151** (163), e187.

Monin, A. S. & Yaglom, A. M. 1971 *Statistical Fluid Mechanics: Mechanics of Turbulence*, 1st edition, chap. 2, pp. 205–256. Cambridge; Massachusetts; London: The MIT Press.

Bibliography

Mortarini, L & Anfossi, D 2015 Proposal of an empirical velocity spectrum formula in low-wind speed conditions. *Quarterly Journal of the Royal Meteorological Society* **141** (686), 85–97.

Mortarini, L, Ferrero, E, Falabino, S, Trini Castelli, S, Richiardone, R & Anfossi, D 2013 Low-frequency processes and turbulence structure in a perturbed boundary layer. *Quarterly Journal of the Royal Meteorological Society* **139** (673), 1059–1072.

Mortarini, L, Maldaner, S, Moor, LP, Stefanello, MB, Acevedo, O, Degrazia, G & Anfossi, D 2016*a* Temperature auto-correlation and spectra functions in low-wind meandering conditions. *Quarterly Journal of the Royal Meteorological Society* **142** (698), 1881–1889.

Mortarini, Luca, Stefanello, Michel, Degrazia, Gervasio, Roberti, Debora, Castelli, Silvia Trini & Anfossi, Domenico 2016*b* Characterization of wind meandering in low-wind-speed conditions. *Boundary-Layer Meteorology* **161** (1), 165–182.

Oettl, Dietmar, Almbauer, Raimund Alfons & Sturm, Peter Johann 2001 A new method to estimate diffusion in stable, low-wind conditions. *Journal of Applied Meteorology* **40** (2), 259–268.

Oettl, D, Goulart, A, Degrazia, G & Anfossi, D 2005 A new hypothesis on meandering atmospheric flows in low wind speed conditions. *Atmospheric Environment* **39** (9), 1739–1748.

Oliveira, Pablo ES, Acevedo, Otávio C, Moraes, Osvaldo LL, Zimermann, Hans R & Teichrieb, Claudio 2013 Nocturnal intermittent coupling between the interior of a pine forest and the air above it. *Boundary-layer meteorology* pp. 1–20.

Rannik, Ullar & Vesala, Timo 1999 Autoregressive filtering versus linear detrending in estimation of fluxes by the eddy covariance method. *Boundary-Layer Meteorology* **91** (2), 259–280.

Russell, Eric S, Liu, Heping, Gao, Zhongming, Lamb, Brian & Wagenbrenner, Natalie 2016 Turbulence dependence on winds and stability in a weak-wind canopy sublayer over complex terrain. *Journal of Geophysical Research: Atmospheres* **121** (19).

Singer, Irving A 1967 Steadiness of the wind. *Journal of Applied Meteorology* **6** (6), 1033–1038.

Skeib, G 1980 Zur Definition universeller Funktionen für die Gradienten von Windgeschwindigkeit und Temperatur in der bodennahen Luftschicht. *Z. Meteorol.* **30**.

SUN, JIELUN, MAHRT, LARRY, BANTA, ROBERT M & PICHUGINA, YELENA L 2012 Turbulence regimes and turbulence intermittency in the stable boundary layer during cases-99. *Journal of the Atmospheric Sciences* **69** (1), 338–351.

THOMAS, CHR & FOKEN, TH 2005 Detection of long-term coherent exchange over spruce forest using wavelet analysis. *Theoretical and Applied Climatology* **80** (2), 91–104.

THOMAS, CHRISTOPH K 2011 Variability of sub-canopy flow, temperature, and horizontal advection in moderately complex terrain. *Boundary-layer meteorology* **139** (1), 61–81.

THOMAS, CHRISTOPH K., CARRIG, SEAN & PETERSON, FOX 2015 Tower method yields ecologically meaningful forest net carbon exchange and evapotranspiration in a steep mountainous watershed in the central oregon cascades. Manuscript prepared for Biogeosciences Discussion.

THOMAS, CHRISTOPH K, MARTIN, JONATHAN G, LAW, BEVERLY E & DAVIS, KENT 2013 Toward biologically meaningful net carbon exchange estimates for tall, dense canopies: multi-level eddy covariance observations and canopy coupling regimes in a mature douglas-fir forest in oregon. *Agricultural and forest meteorology* **173**, 14–27.

VAISALA 2012 Vaisala HUMICAP humidity and temperature prope HMP155 - user's guide.

VICKERS, DEAN, IRVINE, JAMES, MARTIN, JONATHAN G & LAW, BEVERLY E 2012 Nocturnal subcanopy flow regimes and missing carbon dioxide. *Agricultural and forest meteorology* **152**, 101–108.

VICKERS, DEAN & MAHRT, L 1997 Quality control and flux sampling problems for tower and aircraft data. *Journal of Atmospheric and Oceanic Technology* **14** (3), 512–526.

VICKERS, DEAN & MAHRT, L 2003 The cospectral gap and turbulent flux calculations. *Journal of Atmospheric and Oceanic technology* **20** (5), 660–672.

VICKERS, D & THOMAS, CK 2014 Observations of the scale-dependent turbulence and evaluation of the flux–gradient relationship for sensible heat for a closed douglas-fir canopy in very weak wind conditions. *Atmospheric Chemistry and Physics* **14** (18), 9665–9676.

VICKERS, DEAN, THOMAS, CHRISTOPH & LAW, BEVERLY E. 2009 Random and systematic co2 flux sampling errors for tower measurements over forests in the convective boundary layer. *Agric. Forest Meteor.* **149**, 73–83.

WILCZAK, JAMES M, ONCLEY, STEVEN P & STAGE, STEVEN A 2001 Sonic anemometer tilt correction algorithms. *Boundary-Layer Meteorology* **99** (1), 127–150.

Bibliography

Wyngaard, John C. 2010 *Turbulence in the Atmosphere*, 1st edn. Cambridge: Cambridge University press.

Zeeman, Matthias J, Selker, John S & Thomas, Christoph K 2015 Near-surface motion in the nocturnal, stable boundary layer observed with fibre-optic distributed temperature sensing. *Boundary Layer Meteorology* **154** (2), 189.

Declaration of authorship

Hereby, I, **Anita Freundorfer**, declare that I have created this thesis independently, that I have not used other resources and implemental than the ones stated and that I have not submitted this thesis for the attainment of any other academic degree.

Hiermit erkläre ich, **Anita Freundorfer**, dass ich diese Arbeit selbständig verfasst, keine anderen als die von mir angegebenen Quellen und Hilfsmittel benutzt und diese Arbeit nicht bereits zur Erlangung eines akademischen Grades eingereicht habe.

Bayreuth, October 23, 2017   ....